Doctoral Dissertation (Shinshu University)

Development of CNT-based functional nanocomposites and their applications

March 2015

Melvin Gan Jet Hong

ABSTRACT

****

The advancement of nanotechnology is progressing rapidly and the exploitation of them has been geared toward usage in various fields and applications such as nanocomposites, electronic devices, smart materials, and so on. Manipulation of size, morphology, structure, and purity of the nanomaterials has allowed the innovation of advanced materials and improvement to the traditional materials. Furthermore, nanomaterials also have generated a great attention from the researchers and commercial product developers as they can show novel and interesting properties than those of the corresponding bulk materials. In this dissertation, the focus has been forwarded to the fabrication of nanomaterials and the characterization of nanocomposites as electromagnetic (EM) wave absorbers and electroactive actuators. Carbon nanotubes (CNTs) have been utilized mainly in the research to fabricate CNT-based nanocomposites. Moreover, nanoparticles such as barium titanate (BTO) and silver (Ag) nanoparticles also have been synthesized and evaluated. The significant results obtained from this research are as follows:

(1) Barium titanate/carbon nanotube (BTO/CNT) hybrid nanocomposites were fabricated by sol-gel method. The BTO/CNT hybrid nanomaterials were characterized using X-ray diffraction (XRD), transmission electron microscopy (TEM), field emission scanning electron microscopy (FE-SEM), Raman and X-ray photoelectron spectroscopy (XPS). The BTO/CNT hybrid nanomaterials were then loaded in paraffin wax with different weight percentage, and pressed into toroidal shape with thickness of 1.0 mm to evaluate their complex permittivity and complex permeability using vector network analyzer. The reflection loss (*R.L.*) of the samples was calculated according to their measured complex permittivity and permeability. Samples with various weight fractions were prepared and evaluated. Improved *R.L.* can be obtained with higher weight fraction and this greatly affected the absorption ability. The BTO/CNT 60 wt.% hybrid nanocomposites with thickness of 1.1 mm showed a minimum *R.L.* of ~-56.5 dB (over 99.999% absorption) at 13.2 GHz and was the best absorber when compared with the other samples of different thickness. The reflection loss peak shifted to lower frequency and wider response bandwidth can be obtained as the thickness of the samples increased.

The EM wave absorption properties of double-layer BTO/CNT nanocomposites where BTO/CNT nanopowders were incorporated into polyurethane (PU) matrix were also evaluated. The minimum *R.L.* of single-layer BTO/CNT 30 wt.% nanocomposites sample with a thickness of 1.1 mm reached ~-30.3 dB (over 99.9% absorption) at 13.8 GHz, and the bandwidth of the *R.L.* less than -10 dB (over 90% absorption) was 1.5 GHz. The double-layer composites consist of BTO/CNT 30 wt.% (Layer 1) with thickness of 1.0 mm and BTO 30 wt.% (Layer 2) with thickness of 0.3 mm showed a minimum *R.L.* of ~-63.7 dB (over 99.9999% absorption) at 13.7 GHz, and the bandwidth of the *R.L.* less than -10 dB was 1.7 GHz. The *R.L.* improved and wider response bandwidth can be obtained with the double-layer composites. This proves that the thickness of samples can be manipulated to produce absorption bands at different frequencies to design highly effective EM wave absorbers. Furthermore, the high interfacial area of the nanomaterials results in high interfacial polarization and multiple scattering, which improves EM wave absorption. Influence of weight fraction, behavior of permittivity and permeability, nanoeffects, and so on are discussed to understand the EM wave absorption mechanism.

(2) Ag nanoparticles fabricated by chemical reduction process were grafted onto the surface of CNTs to prepare hybrid nanocomposites. The Ag/CNT hybrid nanomaterials were characterized using TEM, XPS, and Raman spectroscopy. The Ag/CNT hybrid nanomaterials were then loaded in paraffin wax, and pressed into toroidal shape with thickness of 1.0 mm to evaluate their complex permittivity and complex permeability. The *R.L.* of the samples was calculated using their measured complex permittivity and permeability. The minimum *R.L.* of the Ag/CNT hybrid nanocomposite sample with a thickness of 1.0 mm reached ~-21.9 dB (over 99 % absorption) at 12.9 GHz, and also exhibited a wide response bandwidth where the frequency bandwidth of the reflection loss of less than -10 dB (over 90 % absorption) was from 11.7 to 14.0 GHz. The Ag/CNT hybrid nanocomposite with thickness of 6.0 mm showed a minimum reflection loss of ~-32.1 dB (over 99.9 % absorption) at 3.0 GHz and was the best absorber when compared with the other samples of different thickness. The reflection loss shifted to lower frequency as the thickness of the samples increased. Interestingly, the Ag/CNT hybrid nanomaterials also exhibited two *R.L.* peaks, at low and high frequency region, as the thickness of the sample increased, and they also showed wide minimum *R.L.* of over -10 dB. The capability to modulate the absorption band of these samples to suit

various applications in different frequency bands simply by manipulating their thickness indicates that these hybrid nanocomposites could be a promising EM wave absorber. Optimization of the EM wave absorber that is able to perform at certain frequency and broad frequency range can be realized by controlling the absorber's design.

(3) The electroactive nanocomposite films were fabricated using PU with modified CNTs as the filler. The CNTs were modified using microwave-induced polymerization and mild hydrothermal route and they were found to be highly dispersed in polar solvents such as dimethylformamide. The modified CNTs contained more carboxyl and hydroxyl groups and showed less aggregation than that of the pristine CNTs. The modified CNTs were characterized using TEM, FE-SEM, thermogravimetric analysis (TGA), and XPS. To evaluate these films we mainly focused on electrical properties such as actuation behavior, volume resistivity, dielectric spectroscopy, impedance analysis, and space charge measurements. We found that the PU/CNT films bent toward the cathode when an electric field was applied and they reverted to its original position when the electric field was removed. Upon the incorporation of CNTs as the filler for the polymer, the electrical properties of the films improved significantly. The highly polarized films had a high relative permittivity, and this produced a higher Maxwell pressure, which assisted the actuation. Asymmetric charge accumulation was observed from space charge measurements in some of the films and this explains the bending deformation and the actuation behavior. This helped us to understand the actuation mechanism and bending deformation direction of this kind of electroactive nanocomposite materials. Furthermore, by considering the factors that affect the actuation, highly effective actuator material that shows high performance and can be applied for advanced materials in the future could be designed.

CONTENTS

****

Chapter 1

****

General introduction

****

1 General introduction

1.1 Nanotechnology

The National Nanotechnology Initiative Strategic Plan, developed by the Nanoscale Science, Engineering, and Technology Subcommitee, defines nanotechnology as shown below [1]:

Nanotechnology is the understanding and control of matter at the dimensions of roughly 1 to 100 nanometers, where unique phenomena enable novel applications. A nanometer is one-billionth of a meter, a sheet of paper is about 100000 nanometers thick. Encompassing nanoscale science; engineering, and technology, nanotechnology involves imaging, measuring, modeling, and manipulating matter at this length scale.

At this level, the physical, chemical, and biological properties of materials differ in fundamental and valuable ways from the properties of individual atoms and molecules or bulk matter. Nanotechnology R&D is directed towards the understanding and creating improved materials, devices, and systems that exploit these new properties.

The development and application of nanotechnology has enhanced job opportunity, economic growth, and improved the quality life of human beings. R&D in this field is expected to result in cleaner and less wasteful methods of manufacture, stronger and lighter building materials, smaller yet faster computers, and more powerful ways to detect and treat disease [2, 3]. With the fabrication of nanometer-scale structures, it is possible to control fundamental properties of materials, such as their melting temperature, magnetic properties, charge capacity, and even their color, without changing the materials' chemical compositions [2]. The usage of this potential will lead to new, high performance products and technologies that were not possible before.

Although nanotechnology is a relatively recent development in scientific research, the development of its central concepts happened over a longer period of time. The concepts and ideas behind nanoscience and nanotechnology started with a talk entitled "There's Plenty of Room at the Bottom" by physicist Richard Feynman at an American Physical Society meeting at the California Institute of Technology (CalTech) on December 29, 1959, long before the term nanotechnology was used [3]. In his talk,

Feynman described a process in which scientists would be able to manipulate and control individual atoms and molecules. Over a decade later, Professor Norio Taniguchi used the term nanotechnology in 1974 to describe machining with tolerances of less than 1μm, in his explorations of ultraprecision machining [3-5]. His definition still stands as the basic statement today:

"*Nano-technology' mainly consists of the processing of separation, consolidation, and deformation of materials by one atom or one molecule.*"

Individual atoms and molecules were conceptually explored in depth by K. Eric Drexler in 1981, who promoted the technological significance of nanoscale phenomena and devices [4]. It involves designing and building machines in which every atom and chemical bond is precisely specified.

Recent advances in fabricating nanostructured materials with novel material properties have stimulated research to create multifunctional engineering materials by designing structures at nanometer scale. Motivated by the recent enthusiasm in nanotechnology, development of nanocomposites is one of the rapidly evolving areas of composite research.

1.2 Nanocomposites

For decades the studies of macrocomposites such as filled polymers have been conducted intensively, where the length scale of polymer fillers is in micrometers. The reinforcement length scale is in micrometers, and the interface of fillers is close to the bulk polymer matrix [2]. On the other hand, nanocomposites are structured with reinforcement (nanoparticles) where the length scale is in nanometer scale [2, 7]. Nanocomposites are composite materials in which the matrix material is reinforced by one or more separate nanomaterials in order to improve performance properties [6]. Generally, the materials used as matrix in nanocomposites are polymers such as polyurethane, epoxy, rubber, polyvinyl alcohol, polyvinyl chloride, and so on. The nanocomposites have ultra large interfacial area per volume, and the distances between the polymer and filler components are extremely short. As a result, molecular interaction between the polymer and the nanoparticles will give polymer nanocomposites unusual material properties that conventional polymers do not possess

[2].

The excitement surrounding nanoscale science and technology allows the unique opportunities to develop revolutionary materials. Nanoscale science and technology is a young field that encompasses nearly every discipline of science and technology. Nanophase and nanostructured materials, a new branch of materials research, is attracting a great deal of attention because of its potential applications in areas such as electronics, optics, catalysis, ceramics, magnetic materials, and polymer nanocomposites. The unique properties and improved performance of nanomaterials are determined by their sizes, surface structures, and interparticle interactions.

Nanomaterials can be categorized into nanostructured materials and nanophase/nanoparticles materials [2]. Nanostructured materials commonly refer to condensed bulk materials that are made of grains (agglomerates), with grain sizes in the nanometer size range. Conversely, nanophase/nanoparticles materials usually describe the dispersive nanoaprticles. The nanometer size covers a wide range, from 1 nm to as large as 100 or 200 nm. To distinguish nanomaterials from bulk materials, it is essential to reveal the unique properties of nanomaterials and their potential impacts in science and technology.

1.3 Polymer nanocomposites

Polymers alone exhibit an excellent range of mechanical, optical, electrical, and surface properties [8]. Fig. 1.1 depicts the brief motivation of research related to polymers [8]. Polymers over the last century have arguably transformed technology more than any other material. Their combination of light weight, low cost, molecular specificity, corrosion resistance, and the properties associated with their large molecular size have made them attractive replacements for metals and ceramics in their role as structural and functional materials [8]. In recent years, the discovery of the electrical, electronic, and optical properties of polymers over the last decade has opened up a vast variety of new applications in developing and challenging technologies. In the last 20 years, from the ability to process and fabricate polymers into a variety of complex and nanoscopic phase, they have been developed significantly.

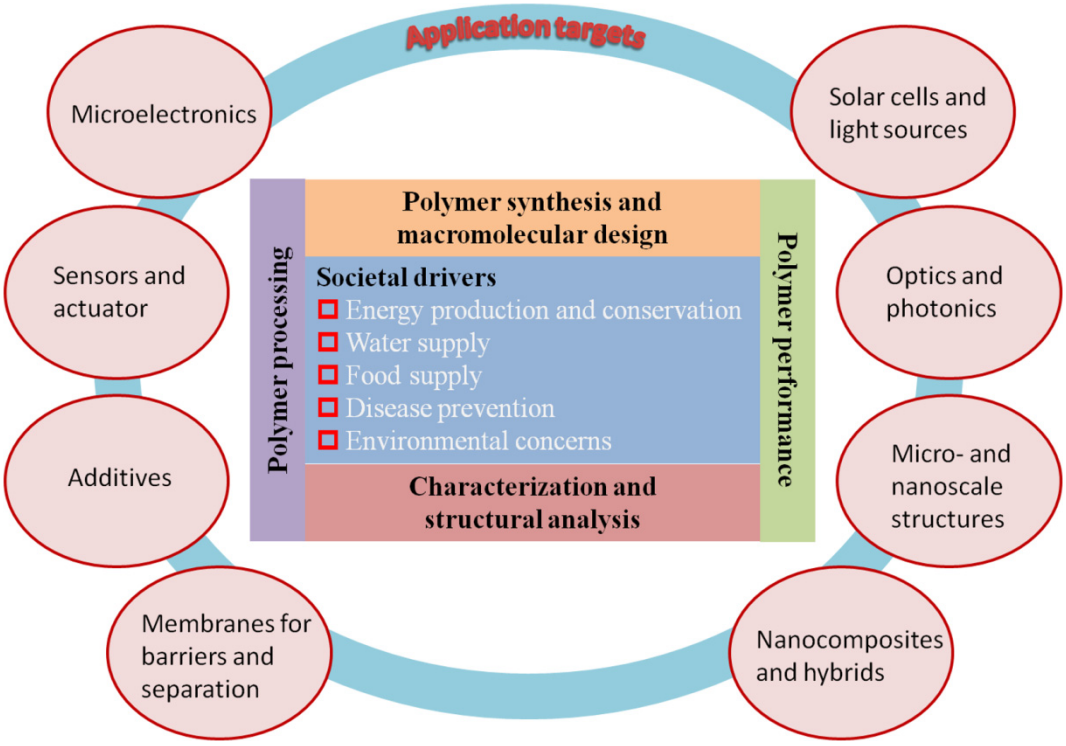

Fig. 1.1 Social drivers motivate research in polymer synthesis, characterization, and processing for improved performance resulting in new applications for polymers.

Nevertheless, there are often circumstances where even more specific or better performance is demanded from the polymers. Since the development of polymers, composite have been used to enhance properties or improve them. The formation of the composite involves incorporating filler, commonly an inorganic filler, to modify polymer performance. In recent years, very small scale fillers, some having dimensions of just a few nanometers, have been modulated to fabricate nanocomposites.

The development of composites has been driven by the need for materials with specific combinations of properties beyond those obtainable from a single material [7]. Polymer nanocomposites consist of polymeric materials such as thermoplastics, thermosets, elastomers, etc., and a reinforcing nanoscale material (nanoparticle) [2]. There are many factors that affect the polymer nanocomposites properties:

- Synthesis method such as melt compounding, solvent blending, in-situ polymerization, high shear mixing, and emulsion polymerization
- Polymer nanocomposites morphology
- Types of nanoparticles and their surface treatments
- Polymer matrix such as crystallinity, molecular weight, polymer chemistry, etc.

The introduction of inorganic nanoparticles as the fillers into polymer systems has resulted in polymer nanocomposites showing multifunctional, high performance polymer characteristics beyond those traditional filled polymeric materials possess [2, 6, 9, 10]. Through control or alteration of the fillers at the nanoscale level, we are able to maximize property enhancement of selected polymer systems to meet or exceed the requirements of current military, aerospace, commercial applications, and so on [2]. The technical approach involves the incorporation of nanoparticles into selected polymer systems whereby nanoparticles may be surface-treated to provide hydrophobic characteristics and enhanced inclusion into hydrophobic polymer matrix.

1.3.1 Thermoplastic-based nanocomposites

Table 1.1 Characteristics of thermoplastic and thermoset resin systems.

Thermoplastic	Thermoset
● High MW# solid	● Low MW liquid or solid
● Stable material	● Low to medium viscosity, requires cure
● Reprocessable, recyclable	● Cross-linked, nonreprocessable
● Amorphous or crystalline	● Liquid or solid
● Linear or branched polymer	● Low MW oligomers
● Some are liquid solvent resistance	● Excellent environmental and solvent resistance
● Short process cycle	● Long process cycle
● Neat up to 30% filler	● Long or short fiber reinforced
● Injection/compression/extrusion	● Resin transfer molding/filament winding/ sheet molding compound/prepreg/pultrusion
● Limited structural components	● Many structural components
● Neat resin + nanoparticles	● Neat or fiber reinforced + nanoparticles
● Commodity: high performance areas for automotive, appliance housings, toys, etc.	● Commodity: advanced materials for construction, marine, aircraft, aerospace, etc.

#MW: Molecular weight

Thermoplastics materials are used in a vast array of products. In the automotive area, they are used for interior parts and in under-the-hood applications. The packaging applications area is a large area for thermoplastics, from carbonated beverage bottles to plastic wrap. Applications requirements vary widely; fortuitously, plastic materials can be formulated to meet these different business opportunities. It remains for designers to select from the array of thermoplastics materials that are available to meet the particular needs of their applications. Many thermoplastics have been nanomodified into polymer nanocomposites by incorporating nanoparticles into the polymers. Table 1.1 lists several characteristics of thermoplastic and thermoset resin systems [2].

1.3.2 Polyurethane

Polyurethane (PU) can be classified into thermoplastics, thermosets, or elastomers, and they are widely used for various kinds of applications. In this study, we mainly used thermoplastic PU as the polymer matrix and in the development of polymer-based nanocomposites. Generally, PU are insulator and they are light, soft, flexible, and easy to fabricate [13-15].

Otto Bayer and his coworkers at I.G. Farben in Leverkusen, Germany, first made PU in 1937 [11, 12]. In the following years, the urethane polymer-forming system has received intensive attention resulting in syntheses of many specialized forms, surface coatings, adhesives, and fibers. PU polymers are traditionally and most commonly formed by reacting a di- or polyisocyanate with a polyol [12]. Both the isocyanates and polyols used to make PU contain on average two or more functional groups per molecule.

1.4 Nanomaterials

There are various kinds or commercially available nanoparticles or laboratory fabricated nanoparticles that can be incorporated into the polymer matrix to form polymer nanocomposites. Depending on the application, the nanoparticles can be manipulated to satisfy the desired effect. Table 1.2 exhibits several benefits and disadvantages when nanoparticles are incorporated into the polymer matrix [2]. A wide variety of different types of materials for reinforcement have been employed in polymer nanocomposites, such as nanoparticles, nanotubes, nanowires, nanorods, and so on. In this study, we focused on barium titanate nanoparticles, silver nanoparticles, and carbon

nanotubes. Their brief introduction is shown in the next section.

Table 1.2 Characteristics of nanoparticles in polymer matrix.

Improved properties	Disadvantages
■ Mechanical properties (tensile strength, stiffness, toughness) ■ Electrical properties ■ Gas barrier ■ Synergistic flame retardant additive ■ Dimensional stability ■ Thermal expansion ■ Thermal conductivity ■ Ablation resistance ■ Chemical resistance ■ Reinforcement	■ Viscosity increase (limits processability) ■ Dispersion difficulties ■ Optical issues ■ Sedimentation ■ Black color when different carbon containing nanoparticles are used

1.4.1 Barium titanate nanoparticles

Origin

Barium titanate (BTO) is the first ferroelectric ceramics, and the most widely used ferroelectric material even after 60 years of its discovery [16-18]. BTO is one of the widely used perovskite materials for electric ceramics and a good candidate for a vast variety of applications due to its outstanding dielectric, ferroelectric, and piezoelectric properties; and has been applied for various applications, such as electromagnetic wave absorber, actuators, capacitors, energy storage devices, and so on [16-30]. BTO was discovered during World War II in 1941 and 1944 in the United States, Russia, and Japan [16]. The initial reports were based on doping studies of titanium dioxide and barium oxide, which produced ceramic materials with enhanced dielectric properties [16]. The mixed oxides were made by Thurnaurer and Deaderick at the American Lava Co. as early as 1941 [31]. In the following years, more precise studies were reported by Wainer and Solomon in the United States, Ogawa and Waku in Japan, and Wul and Goldman in Russia [32-34].

Perovskite structure

The perovskite structure is adopted by many oxides that have the chemical formula of

ABO_3, including BTO. Generally, the crystal structure is a primitive cube, with the A-larger cation in the corner, the B-smaller anion in the middle of the cube, and the anion which commonly is oxygen in the centre of the face edges; where A is a monovalent, divalent, or trivalent metal and B a pentavalent, tetravalent, or trivalent element, respectively [17]. Geometrical packing of ions in the lattice is an essential factor determining the structure type. The solid also can exist in five phases, listing from high temperature to low temperature: hexagonal, cubic, tetragonal, orthorhombic, and rhombohedral crystal structure.

Synthesis methods

There are various synthesis methods to produce BTO. As miniaturization and light weight requirement of electronic devices continues to demand smaller particle size powders with controlled morphology, the desired characteristics of the starting powder become an essential issue [17, 35]. The successful synthesis of BTO powder with their unique dielectric properties largely depends on the purity and crystal structure that greatly influences final properties [17, 36, 37].

(a) Conventional solid-state reaction (top-down manufacture)

Conventionally, BTO is fabricated by a solid-state reaction that involves ball milling of barium carbonate or barium oxide with titanium dioxide. The mixture has to be calcined at high temperature in the range of 800°C to 1200°C [38-40]. Generally, the BTO powders prepared by a solid-state reaction are highly agglomerated, large particle size (2-5 μm), irregular morphologies, and high impurity contents due to their inherent problems such as high reaction temperature, heterogeneous solid phase reaction, which result in poor electrical properties of the BTO [41]. One of the solutions to these problems, wet chemical synthesis routes can be considered effective to generate high purity, homogenous, nanoscale powders.

(b) Wet chemical synthesis route (bottom-up manufacture)

Chemical method has been established through techniques such as sol-gel [22, 23, 25, 27], hydro/solvothermal [28, 29, 38], coprecipitation [39, 40], polymeric precursor method [37], and so on. These methods give advantages such as quasi-atomic dispersion of constituent components in a liquid precursor, which facilitates synthesis of the crystallized powder with micro/nanoscale particles and high purity at low temperature

[17]. In our study, BTO nanoparticles were fabricated using the sol-gel method, and will be discussed below.

Sol-gel method is a technique to fabricate metal oxide glasses and ceramics by hydrolyzing a chemical precursor to form a sol and then a gel, which finally on drying (evaporation) and pyrolysis results in an amorphous oxide [17]. Upon further heat treatment, crystallization can be achieved. Generally, the basic steps involved are as shown below [17]:

① Partial hydrolysis of metal oxide to form reactive monomers
② Polycondensation of these monomers to form colloid like oligomers (sol)
③ Additional hydrolysis to promote polymerization and cross-linking leading to a 3-dimensional matrix (gel)

As polymerization and cross-linking progress, the viscosity abruptly increases and gel occurs. In this process, the sol evolves gradually towards the formation of a gel-like network containing both a liquid phase and a solid phase.

Applications

BTO nanoparticles have been vastly used for various applications. BTO which is used extensively in multilayer capacitors, thermistors, and electrooptic devices, shows a ferroelectric to nonferroelectric phase transition when its size is reduced below 100 nm [19]. Furthermore, the BTO nanoparticles also have been incorporated into polymer matrix to produce polymer nanocomposites, and they are desired because the breakdown voltage of ceramic phase is increased by the introduction of a polymer matrix such that the dielectric constant is not compromised [19].

Moreover, the BTO nanocomposites and hybrid nanocomposites also have been exploited as a promising electromagnetic wave absorber material [22-30]. The high interfacial area of the nanomaterials results in high interfacial polarization and multiple scattering, which improves electromagnetic wave absorption. The weight compositions of nanomaterials, thickness, and design/structure of the nanocomposites, which greatly affect the absorption properties of the materials also have been manipulated to realize an optimum absorber material.

1.4.2 Silver Nanoparticles

Origin

Over the past few decades, noble metal nanoparticles such as silver (Ag) nanoparticles which exhibited significantly distinct physical, chemical, electrical, thermal, and biological properties in contrast to the bulk parent materials have been greatly explored [42-46]. Ag nanoparticles can be applied for wide range of applications in various fields such as nanocomposites, medical, and electronic devices [42-46]. Over 116 years ago in 1899, M. C. Lea reported the synthesis of a citrate-stabilized Ag colloid where the average diameter of particles obtained is between 7-9 nm [47]. Furthermore, the stabilization of Ag nanoparticles using proteins has been described as early as 1902 [48] under the name "Collargol" (mean particle size of 10 nm) and has been manufactured commercially since 1897 for medical applications [49-51]. Other Ag nanoparticles fabrications were also developed in the next decades; the gelatin stabilized Ag nanoaparticles (2-20 nm) patented by Moudry in 1953 [52] and Ag nanoparticle (below 25 nm) impregnated carbon [53]. The long history of rational fabrication and use of colloidal Ag nanoparticles has resulted in a lot of research and knowledge about these nanomaterials over the last 100 years, even some of the researches are not reported using the term "nano" [42].

Synthesis methods

Generally, metal nanoparticles can be fabricated by two routes. The first one is a physical approach (top-down) that utilizes several methods such as evaporation/condensation and laser ablation [43, 45]. The second one is a chemical approach (bottom-up) in which the metal ions in solution are reduced in conditions favoring the subsequent formation of small metal clusters or aggregates [54-56].

(a) Physical approach (top-down manufacture)

The Ag nanoparticles can be typically fabricated by evaporation/condensation, which can be conducted by using a tube furnace at atmospheric pressure. However, this method has several drawbacks such as a large space of tube furnace, large consumption of energy, and a time consuming process [43, 44]. Furthermore, Ag nanoparticles also have been produced with laser ablation of metallic bulk materials in solution [57-60]. The characteristics of the metal particles formed and the ablation efficiency greatly depend upon various parameters such as the wavelength of the laser impinging the

metallic target, the duration of the laser pulse (femto-, pico-, nanosecond), the laser fluence, the ablation time duration, the effective liquid medium, the presence of surfactants, etc. [43]. The physical approaches typically utilize energies (thermal, electrical) to fabricate Ag nanoparticles. Even though these methods allow for large quantity production in a single process, the high cost and investment of equipments should be concerned.

(b) Chemical approach (bottom-up manufacture)

Generally, the chemical approach synthesis route of the Ag nanoparticles in solution typically employs the following components: (i) metal precursors, (ii) reducing agents, and (iii) stabilizing/capping agents [44]. Chemical reduction is the most regularly applied method for the preparation of Ag nanoparticles. The process only requires simple equipment and is convenient, inexpensive, and gives a high yield [61-64]. Commonly, the process involves the reduction of a silver salt such as silver nitrate with the reductants like sodium borohydride, citrate, ascorbate, and elemental hydrogen [43, 65]. Moreover, the typical colloidal stabilizers used are polyvinyl alcohol, poly(vinylpyrrolidone), bovine serum albumin, citrate, and cellulose [65]. The reduction of Ag ions (Ag^{+}) in aqueous solution commonly yields colloidal silver where the particle diameter is in several nanometers order. Primarily, the reduction of various complexes with Ag^{+} leads to the formation of Ag atom (Ag^{0}), which is followed by agglomeration into oligomeric clusters. Then, these clusters eventually lead to the formation of colloidal Ag particles.

Applications

Recently, Ag nanoparticles have attracted the attentions and have been applied extensively as anti-bacterial agents [66] in the health industry, food storage, textile coatings and a number of environmental applications. It is important to note that despite of decades of use, the evidence of toxicity of silver is still not clear. As anti-bacterial agents, Ag nanoparticles were applied in a wide range of applications from disinfecting medical devices and home appliances to water treatment.

Furthermore, by utilizing the excellent electrical conductivity and nanoscale size of the Ag nanoparticles, research related to inkjet inks to produce electronic devices (printed electronic circuits) [62, 63], conductive thin films [64], and many more, have been conducted. Moreover, Ag nanoparticles and Ag hybrid nanocomposites also have

been applied for electromagnetic wave absorber materials [61, 67-69]. They showed good absorption ability and can be considered as a promising absorber material.

1.4.3 Carbon nanotubes

Origin

There are great numbers of reviews and publications related to the history, synthesis, excellent properties, and development as polymer nanocomposites of carbon nanotubes (CNTs) [70-86]. Since the discovery of fullerene (C_{60}, buckyball) by Kroto et al. [87] in 1985, and both multi- and single-walled CNTs soon afterwards by Iijima in 1991 [88] and 1993 [89], respectively, the interest in CNTs has rapidly developed. Furthermore, CNTs are famous for their outstanding mechanical, electrical, chemical, thermal, etc. properties that allow them to be manipulated for various applications and research studies [70-86]. Moreover, CNTs also play an essential role as the fillers for composite materials, including polymer nanocomposites. The first ever polymer nanocomposites using CNTs as fillers were reported in 1994 by Ajayan et al. [90].

Structure and morphology

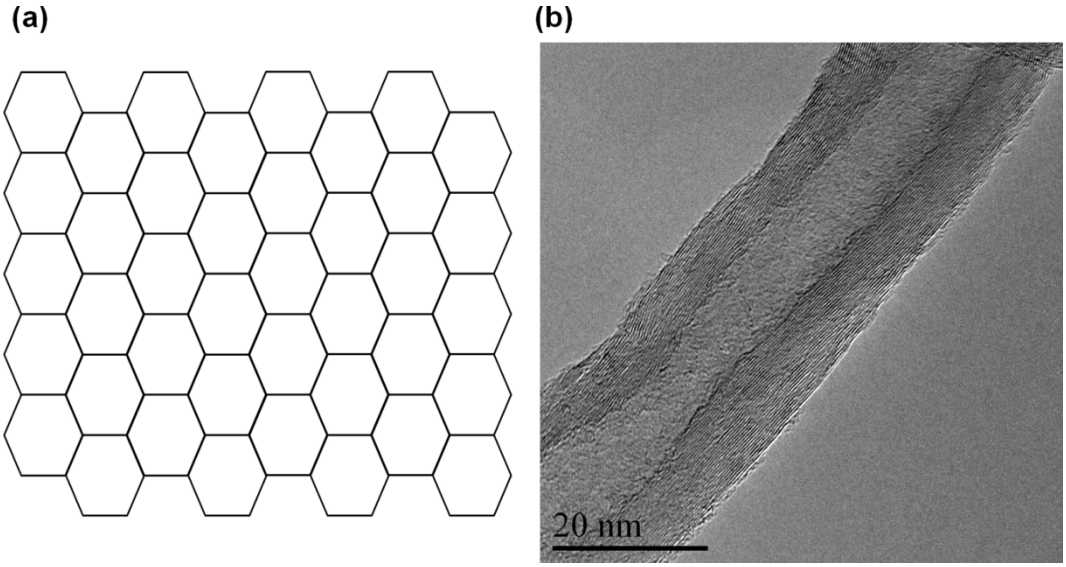

Fig. 1.2 (a) Schematic image of graphene sheet and (b) TEM image of MWCNT.

Generally, CNTs can be grouped into single-walled CNT (SWCNT) and multi-walled CNT (MWCNT). A SWCNT can be thought of as a rolled-up sheet of a structure called graphene, which is a single layer of an allotrope of carbon called graphite, and the edges

of the sheet are joined together to form a seamless tube [7, 71, 72]. Several tubes of different diameter can be fitted into each other to make a MWCNT. Fig. 1.2 shows schematic image of graphene sheet and transmission electron microscopy (TEM) image of MWCNT.

Synthesis methods

There are three methods to produce CNTs: arc discharge, laser ablation, and chemical vapor deposition (CVD). Each of these techniques has its advantages and disadvantages and briefly discussed below.

Arc discharge and laser ablation depend on the evaporation of a graphite target to create gas phase carbon fragments that recombine to form CNTs. The temperature reached in these processes is in the range 2000-3000°C, sufficient enough for the carbon atoms to rearrange into the tube structure. In order to promote the yield of CNTs, several different metals in concentrations about 1% are incorporated into the target materials that is evaporated [72]. For application of CNTs for composite materials where large quantities of CNTs are required, these methods would make the cost of CNTs prohibitive [82]. However, a large amount of non-tubular graphitic and amorphous carbon is also produced during the process [72, 82]. Thus, purification steps are essential before the usage of them.

CVD is the most widely used method for the production of CNTs. Generally, the CVD process includes catalyst-assisted decomposition of hydrocarbons, usually ethylene or acetylene, in a tube reactor at 400-1100°C and growth of CNTs over the catalyst upon cooling the system [72, 83, 84]. The growth temperature depends on the type of CNTs to be grown and the catalyst composition [72]. The advantages of this method are the ability to fabricate aligned arrays of CNTs with controlled diameter and length, and under the right condition only nanotubes are produced and no unwanted graphitic material [72, 82].

Dispersion of CNTs

CNTs disperse poorly in organic and aqueous solvents and tend to agglomerate because of a strong intrinsic van der Waals attraction between the CNTs. These problems also affected their performance as a nanocomposite material, including when incorporated into polymer matrix. To encounter these drawbacks, modifications toward the CNTs are an effective solution.

(a) Ultrasonication

Ultrasonication is a type of mechanical dispersion of CNTs. This process is the act of applying ultrasound energy to agitate particles (CNTs) in a low viscosity solution such as water or ethanol [79]. Commonly, this method is achieved by using an ultrasonic bath or ultrasonic probe/horn. When ultrasound propagates via a series of compression, attenuated waves are induced in the molecules of the medium through which it passes. As a result, bundles or agglomerates can be separated.

(b) Covalent functionalization

Direct covalent sidewall functionalization is associated with a change of hybridization from sp^2 to sp^3 and a simultaneous loss of π-conjugation system on graphene layer [77, 79]. This method can be established by reaction with some molecules of a high chemical reactivity. Commonly, functional groups such as carboxyl (–COOH) groups and hydroxyl (–OH) groups are attached onto the surface of CNTs during the oxidation using concentrated sulfuric acid, nitric acid, acids mixture, aqueous hydrogen peroxide, or strong oxidants [61, 64, 68, 69]. The number of –COOH and –OH groups on the surface of CNTs depends on acid treatment temperature and time, increasing as the temperature increased. Furthermore, the extent of the induced –COOH and –OH functionality also depend on the oxidation procedures and oxidizing agents. Moreover, nanotube ends also can be opened during the oxidation process. The CNTs functionalized using this method are able to disperse in many organic solvents because the hydrophobic nature of CNTs is changed to hydrophilic due to the introduction of polar/functional groups [79]. In the same time, the functionalized CNTs will also provide strong interfacial bonds when incorporated into polymer matrix, allowing CNT-based polymer nanocomposites to possess excellent and multifunctional properties.

(c) Non-covalent functionalization

Non-covalent functionalization is an alternative way for tuning the dispersion or interfacial properties of CNTs. This method does not compromise the physical properties of CNTs, but improves solubility and processability [77]. This kind of functionalization majorly involves wrapping the CNTs with polymer or using surfactants. The polymer wrapping process is achieved through the van der Waals interaction and π–π stacking between CNTs and polymer chains containing aromatic

rings [79]. Conversely, anionic, cationic, and surfactants can be used to perform non-covalent functionalization of CNTs. The physical attachment of surfactants on the surface lowered the surface tension of CNTs, effectively preventing the aggregation of CNTs [79]. Moreover, the surfactant-treated CNTs overcome the van der Waals attraction by electrostatic/steric repulsive forces. The efficiency of this method depends greatly on the properties of surfactants and medium chemistry.

1.5 Electromagnetic wave absorber

In our study, we utilized BTO nanoparticles, Ag nanoparticles, CNTs, and the hybrid nanocomposites of them, for the application of electromagnetic (EM) wave absorber, or also known as microwave absorber. This section will present the introduction of EM wave absorber.

Research related to EM wave absorbers started in the 1930's [91], and first patent was in 1936 in Netherlands [92]. The absorber was a quarter-wave resonant type using carbon black as a lossy resistive material and titanium dioxide for its high permittivity in order to reduce the thickness. During World War II, Germany navy has developed several EM wave absorbers (Jaumann absorber, etc.) for the technology of radar camouflage for submarines [91]. The material had a layered structure and was based on graphite particles and other semiconductive materials embedded in a rubber matrix. In the United States, Salisbury screen that was invented by W. W. Salisbury in 1952 [93], was one of the first concepts in radar absorbent material, later known as "stealth technology", used to prevent enemy radar detection of military vehicles. Later, led by Halpern at MIT Radiation Laboratory, materials known as Halpern Anti Radiation Paint (HARP) was developed [94, 95]. In the following years and after few decades (on to today), the development of EM wave absorbers are still developing and some of them are already used for practical applications and commercial products [91, 96-98].

The increase of EM pollution due to the advancement of gigahertz electronic systems, development of electronic devices and communication instruments in commercial, industrial, scientific, and military fields, such as mobile phones, computers, radar technology, and wireless network systems has resulted rapidly growing and intense interest in EM wave absorber technology [99-103]. EM radiation can cause device malfunction, generate false images, reduce devices performance, and also harm the health of human beings, especially expectant mothers and children [97, 100, 101, 104].

These are some of the factors why the usage of self-generated EM radiation devices such as cellular telephones, wireless computer, and the devices in the same category are strictly prohibited in certain areas, which include hospitals, banks, petrol stations and inside airplanes. Therefore, it is essential to protect electronic devices and human beings from excessive exposure to EM radiation. EM wave absorber materials have received much attention to effectively solve the problem of exposure to EM radiation. An ideal EM wave absorber should be lightweight, strongly absorb EM waves, and possess tunable absorption frequency, and multifunctionality [99, 100].

Generally, EM absorber consist a filler material inside a matrix material. The filler which can be one or more constituents play an important role to do most the absorbing. Nanomaterials such as nanoparticles and hybrid nanocomposites are among excellent candidates as the filler. The matrix material is chosen for its physical properties such as temperature resistance, weatherability, etc. Commonly, polymer matrix is chosen because they are light weight, cost efficient, and flexible.

1.5.1 Absorption theory

EM wave absorption is a process where the energy of EM wave is depleted and then transformed into other energy, such as heat, and in result the wave cannot be reflected or permeated through the absorber materials [99, 100]. The incident wave through the absorber materials undergoes the following phenomenon: penetration, reflection, and absorption, as shown in Fig. 1.3.

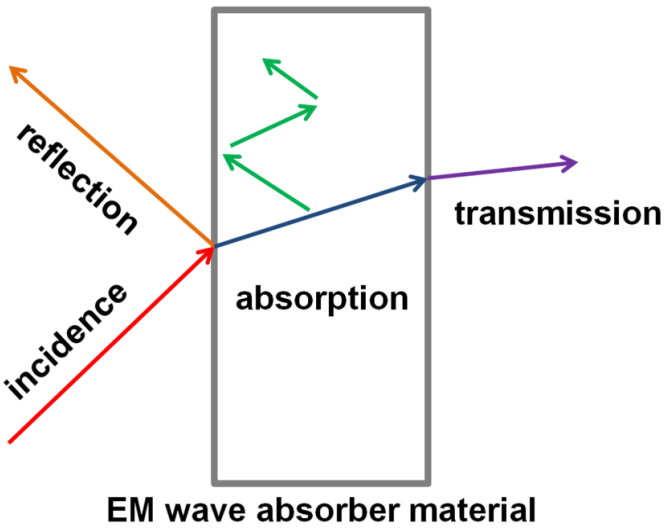

Fig. 1.3 General processes of an incident EM wave through an EM wave absorber material.

Furthermore, an excellent EM wave absorber material must fulfill two basic requirements [26, 100, 105, 106]:

① Concept of matched impedance: the characteristic impedance of an absorber should be almost equal to that of the free space to achieve zero reflection on the front surface of the material, which requires the complex permittivity close to complex permeability.

② The absorber materials can absorb incident waves as much as possible inside the absorbers, which requires the materials to exhibit strong magnetic or/and dielectric loss.

Two main material parameters that highly associated with the EM wave absorption are complex permittivity ε (real part ε' and imaginary part ε'', $\varepsilon = \varepsilon' - j\varepsilon''$) and complex permeability μ (real part μ' and imaginary part μ'', $\mu = \mu' - j\mu''$). The real part of permittivity and permeability represent the energy storage, while the imaginary part of permittivity and permeability are related to dielectric loss or energy dissipation within a material resulting from conduction, resonance, and relaxation mechanisms. The EM absorption properties of a material backed by a perfect electric conductor (metal plate), as shown in Fig. 1.4, typically investigated using the reflection loss (*R.L.*, dB) that is calculated according to the transmission line theory as follows [99-101]:

$$R.L. = 20\log\left|\frac{Z_{in}-1}{Z_{in}+1}\right| \tag{1.1}$$

where the normalized input impedance (Z_{in}) is given by the formula,

$$Z_{in} = \sqrt{\frac{\mu_r}{\varepsilon_r}}\tanh\left[j\left(\frac{2\pi fd}{c}\right)\sqrt{\mu_r\varepsilon_r}\right] \tag{1.2}$$

where $\varepsilon_r = \varepsilon' - j\varepsilon''$, $\mu_r = \mu' - j\mu''$, f (Hz) is the EM wave frequency, d (m) is the thickness of the absorber, and c (m/s) is the velocity of light in free space. Typically, the value of -10 dB and -20 dB for *R.L.* represent that 90% and 99%, respectively, EM waves are absorbed by the materials. The energy depletion mechanism associated majorly with the dielectric loss and magnetic loss.

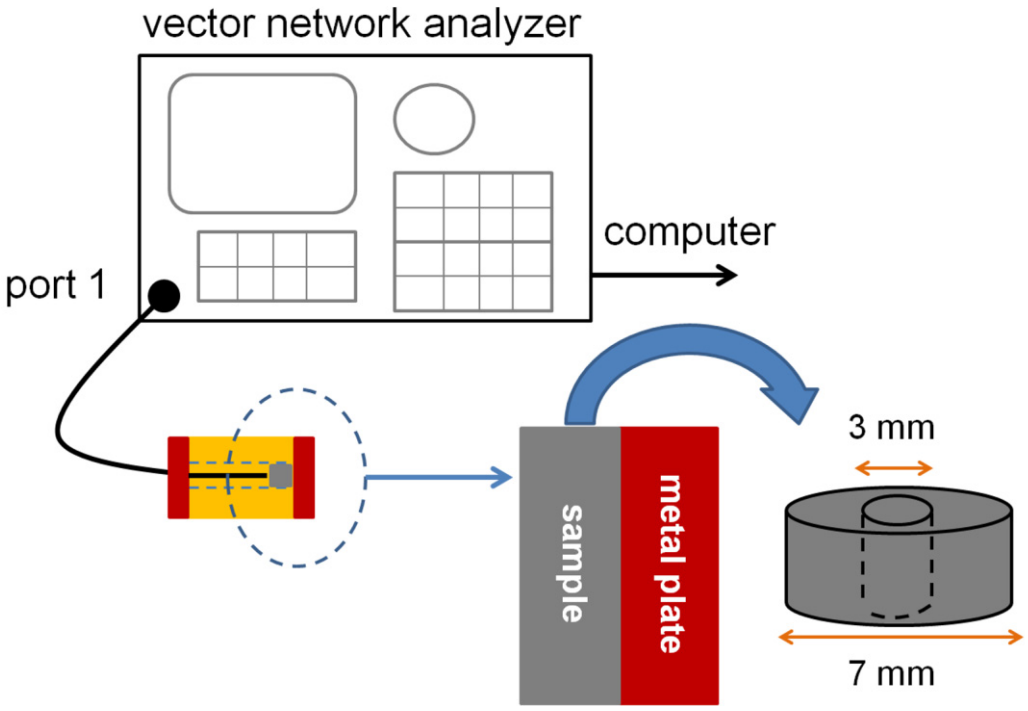

Fig. 1.4 Experimental setup to evaluate EM wave absorption properties.

1.5.2 Influence factors for EM wave absorption

The electrical and magnetic properties, design, size, morphology, and structure of materials influence greatly their EM wave absorption ability. In order to gain excellent EM wave absorption property, the materials must be well designed to achieve the concept of matched impedance.

(a) Basic EM parameters

Magnetic loss

When penetrated with EM waves, magnetic materials will produce mainly three energy loss: eddy current loss, magnetic hysteresis loss, and residual loss. If a conducting material was put in an alternating magnetic field, a close induced current will be produced inside the material, which would dissipate the energy and referred as

eddy current loss [100]. The eddy current loss is also influenced by other factors, such as orientation, grain size, surface roughness, morphology of material, and so on. Meanwhile, magnetic hysteresis loss is induced by the irreversible domain movement and magnetic moment rotation of magnetic material [100]. Furthermore, magnetic loss except the two types of losses mentioned before is called as residual loss. At low frequency, the residual loss was caused mainly by magnetic after-effect loss, which includes thermal fluctuation or the hysteresis of some electrons and ions moving to equilibrium position relative to the diffusion of applied magnetic field. This kind of loss is determined by the amplitude of alternating magnetic field and relaxation time of materials. Conversely, at high frequencies, the residual loss is affected by size resonance, ferromagnetic resonance, natural resonance and/or domain wall resonance [100, 107].

Examples of magnetic nanoparticles are such as materials that commonly consist of magnetic elements such as iron, nickel, cobalt, and their chemical compounds. Cui et al. synthesized nanocomposites consisting of magnetite (Fe_3O_4)/polyaniline, and the maximum *R.L.* was -31.3 dB at 9 GHz, when the thickness is 3 mm [106]. Guo et al. fabricated PU nanocomposites filled with iron core/iron oxide shell nanoparticles which exhibited maximum *R.L.* of -27.5 dB at 10 GHz [108]. There are many other papers and reports presented, where magnetic materials were applied for EM wave absorber.

Dielectric loss

Interacting with EM waves, dielectric material dissipate electric energy which then transformed into other energy such as thermal energy, and the energy is refereed as dielectric loss. Basically, the mechanisms of dielectric loss include conductance loss, dielectric relaxation loss, and resonance loss [100].

EM wave absorber material with certain electric conductivity produces conductance current. When an alternating electric field acted on it, the current dissipates the energy into heat. The conductance loss is majorly determined by the electric conductivity of materials. However, a proper electric conductivity of material must be designed to obtain great wave absorption effect. Fig. 1.5 demonstrates the relationship between conductivity and EM wave transmission through absorber material. The impedance of material with high conductivity is relatively small in contrast to air, thus the skin depth is small and nearly most of EM wave will be reflected by the absorbers. Carbon-based material such as carbon black (conductor) has been incorporated into the matrix and

used as an EM wave absorber since it was first patented in Netherlands in 1936 [92]. Carbon black remained as the favorable filler for absorber materials for a few decades. Afterwards, with the discovery of CNTs, which are excellent electric conductor in the 1990's, besides their application for various fields, they also have been noticed as an exceptional candidate for EM wave absorber material. High electrical conductivity of CNTs makes them capable of dissipating electrostatic charges or shielding EM radiation. Ting et al. fabricated nanocomposites using CNTs and conducting polymer, polyaniline [108]. By utilizing conducting materials, their materials showed enhanced EM wave absorption. Furthermore, metallic particle such as Ag nanoparticles is also a good conductor, abundant, easy to prepare, and inexpensive [109-111]. Ag nanoparticles decoration would have a beneficial effect on the electrical conductivity of CNTs because the inherent electrical conductivity of Ag is superior to the CNTs without Ag [109]. Ramesh et al. [67] investigated the EM absorption properties of Ag nanoparticles embedded in thin polymer films. The films exhibited appreciable EM wave absorption in the 8-12 GHz range. Meanwhile, Zhao et al. [68, 69] examined the EM absorption properties of CNTs filled with Ag nanowires. The maximum *R.L.* of -19.2 dB at 7.8 GHz was obtained.

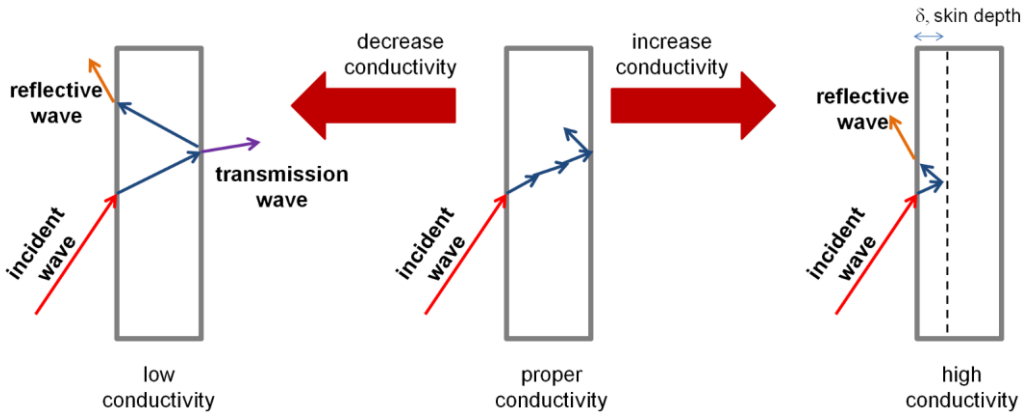

Fig. 1.5 EM wave transmission model for materials with different conductivity.

Under the application of electric field, the materials would be polarized, and if the change of polarization is slower than that of electric field, the dielectric relaxation loss will be produced. The most common polarizations from low frequency are: thermal ion polarization, dipole rotation polarization, ion (atomic) polarization, and electronic displacement polarization [100, 112]. Fig. 1.6 exhibits various polarizations over a broad frequency. The time constant for thermal ion and dipole rotation polarization is

about 10^{-8}-10^{-2} s; meanwhile, for electronic displacement and ion polarization, the time constant is very short (energy loss at high frequency, ~10^{15} Hz), about 10^{-15}-10^{-14} s. As a result, at high frequencies, the electronic displacement and ion polarization play an essential role in relaxation loss. BTO is a typical dielectric material and have been studied widely for the use as EM wave absorber materials. In the earlier studies conducted by our research group, BTO nanotubes had been synthesized and their EM wave absorption properties had been evaluated [24, 30]. Their absorption properties indicated that BTO can be manipulated as an efficient and promising EM wave absorber material. Bi et al. [28] and Huang et al. [29] fabricated BTO/CNT composites by a solvothermal method and investigated their EM wave absorption properties. Their results showed that enhanced EM wave absorption can be achieved by using the combination of BTO and CNT. Using other fabrication method, Wang et al. fabricated BTO and carbon black compound via sol-gel method and also investigated the EM wave absorption properties [25]. Significant EM wave absorption properties were also obtained from their study.

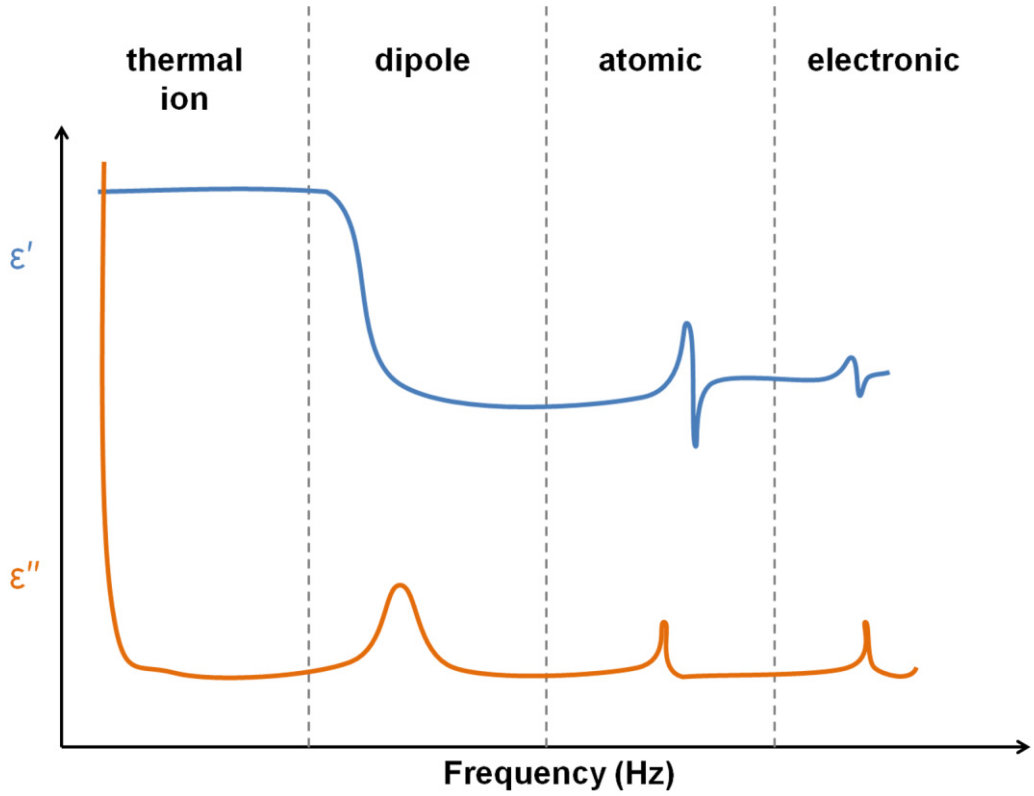

Fig. 1.6 Various polarizations over a broad range of frequency.

The resonance loss originated from resonance effect induced by the vibration of

atoms, ions, or electron inside of the particular materials. Moreover, it is produced at the scope of infrared to ultraviolet frequency.

Complex permittivity and complex permeability

Complex permittivity and complex permeability are basic parameters associated with the EM wave absorption properties of a material. Furthermore, dielectric loss factor (tan $\delta_\varepsilon = \varepsilon''/\varepsilon'$) and magnetic loss factor (tan $\delta_\mu = \mu''/\mu'$) also play a great role to reveal the intrinsic reasons for the EM wave absorption.

From tan δ_ε , the bigger the ε'', better absorption effect can be expected. Thus, materials with high permittivity are often chosen as the candidate for absorber materials. However, the reflection part of wave is relatively large for a material with too high permittivity [113], which indicates that material with proper permittivity must be selected according to practical needs. In the case where the matrix is polymer, polymer with low dielectric loss is better for the absorption property, which can allow more waves to transmit into the absorber material [101].

From tan δ_μ and magnetic loss mechanisms, we also can interpret that the bigger the μ'' and the smaller the μ', the larger the magnetic loss of materials can be obtained. However, according to the concept of matched impedance, when the permeability is equal to the permittivity, there is no reflection and the EM wave absorption effect is the best.

(b) Nanoeffect

Nanoscale materials were endowed with outstanding electric and magnetic properties owing to their particular size, surface and quantum tunnel effect. Nanomaterials such as nanoparticles and hybrid nanocomposites are among essential candidates as EM wave absorbing materials. For instance, the relative density of nanomaterials is lower, and their specific surface area is larger than those of the corresponding bulk materials. As a result, there are a large number of active atoms at the nanomaterial surface, which has a large interfacial dielectric loss induced by interface polarization and will allows multi reflection to progress [100]. Furthermore, hybrid nanocomposites such as CNTs decorated with nanoparticles on their surface, will absorb energy through electron hopping and shows enhanced EM absorption bandwidth [99]. The combination of nanoparticles with CNTs can integrate the properties of these two components to form hybrid nanocomposites for use as EM wave absorber materials. Moreover, if the particle

size is below the skin depth, the eddy current loss can be induced which can enhance the stability of wave absorption property. Generally, the skin depth of a particular material is about 1 μm at frequency of 10 GHz, which prove that nanomaterials will posses great EM wave absorption properties at broad frequency [100].

(c) Design of materials

Generally, the EM wave absorption ability can be manipulated by controlling the weight fraction composition, thickness, and layer structure of the absorber materials. Basically, higher weight fraction of filler in the matrix of a particular absorber material will produce higher absorption ability. Although higher absorption ability can be achieved by this method, some problems are inevitable: cost performance, dispersion and homogeneity problems, electric conductivity percolation threshold (reflected wave), and so on. By adjusting the thickness of absorber materials, higher absorption ability can be obtained and the absorption peak will shift to lower frequencies. The *R.L.* will increase as the thickness increase, until a certain frequency, and then it will decrease gradually. However, it is difficult to prepare light weight and flexible absorber materials by this way, and to fulfill the demands for thin absorber material.

In order to gain higher absorption ability and broad absorption frequency, a multilayer structure of absorber material is an effective method. Fig. 1.7 shows the multilayer structure of EM wave absorber.

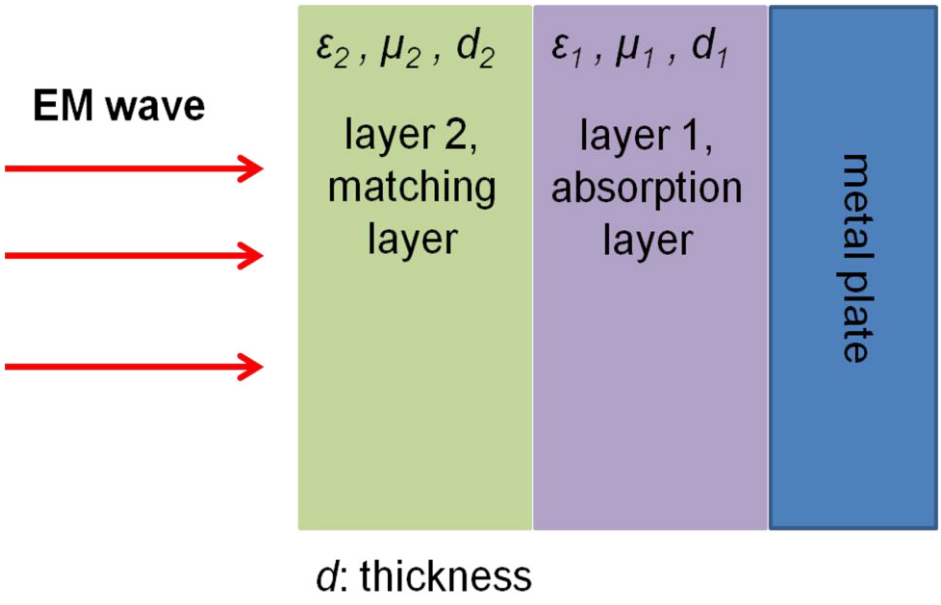

Fig. 1.7 Multilayer EM wave absorber.

Basically multilayer includes layers of: impedance matching layer (matching layer), EM wave loss layer (absorption layer), and reflective layer (metal plate), in which the matching layer can transmit the EM wave without reflection by adjusting the complex permittivity and permeability of material; the EM wave is depleted in the absorption layer composing of high dielectric or magnetic loss materials; the role of the reflective layer is to make a small quantity of transmission wave back to the wave loss layer [99, 100, 114]. Through this specific structure design, the material shows enhanced EM wave absorption ability and broad absorption frequency. Furthermore, by manipulating the thickness of matching and absorption layer, absorption at various frequencies can be achieved. Yuchang et al. used a matching layer filled with 50 wt.% BTO, and an absorption layer filled with 60 wt.% BTO and 20 wt.% carbonyl iron particles with total thickness of 1.4 mm. The maximum *R.L.* of -59 dB was obtained at 12.5 GHz. Wu et al. used ordered mesoporous carbon as filler and their study also showed enhanced EM wave absorption properties when double-layer structure was adopted [114].

1.6 Electroactive polymer

In our study, we fabricated nanocomposite film based on PU and modified CNTs, for the application of electroactive actuator. This section will present the introduction of electroactive nanocomposite actuator.

For few decades, shape memory materials have received significant attention as they can be considered as promising smart materials. Shape memory materials are stimuli-responsive materials that change their shapes upon the application of external stimuli [115]. In contrast to other shape memory materials such as shape memory alloys or shape memory ceramics, shape memory polymers (SMPs) are light, have low density, have low cost, and are easy to fabricate [115-126]. External stimulation such as heat, electric fields, magnetic fields, pH, light, or vapor can trigger the shape memory effect [116-126]. Generally, heat-stimulated SMPs have been evaluated widely. In the earlier research by our research group, shape memory effect of PU-based SMP composites using heat stimulation (thermo-mechanical) was reported [121, 122]. The PU-based SMP composites showed remarkable shape memory effects. However, not only heat, stimulation such as electric fields will enable the manipulation of shape memory behavior at ambient temperature and eliminate the temperature constraints arising from external heating [117, 118]. An electric field-stimulated polymer-based actuators are

referred to as electroactive polymers (EAPs) and can be considered as a type of SMP [126-128]. They are soft and flexible materials that can convert electrical energy to mechanical energy and thus impart a force and produce large strain [126-133].

1.6.1 Background of EAPs

The beginning of EAPs can be traced back to a research that was conducted by Roentgen in 1880; he tested the effect of an electrical current on the mechanical properties of a rubber band [134]. The rubber band was charged and discharged with a fixed end and a mass attached to the free end. It is worth to note that Roentgen attributed the observed volume change to thermal effects of the electric field and the interaction with the rubber strip that was made of a dielectric material. Later in 1899, Sacerdote followed up Roentgen's research and formulated the strain response to electric field activation [135]. These milestones were followed in 1925 when the first piezoelectric polymer called electret was discovered [136]. Electret was formed when carnauba wax, rosin, and beeswax were solidified by cooling while they were subjected to a DC bias field. Following in 1969, Kawai observed a substantial piezoelectric activity in polyvinylidene fluoride (PVDF) [137], and then researchers started to investigate other polymer systems (eventually including the EAPs), and a series of effective materials have emerged. The largest progress in EAP materials development is when effective materials that can induce strains that exceed 100% have emerged [138]. In 1999, one of the pioneers of the EAPs field, Yoseph Bar-Cohen, proposed the Armwrestling Match of EAP Robotic Arm Against Human Challenge [139-142]. This was a challenge in which research groups around the world competed to design a robotic arm consisting of EAP muscles that could defeat a human in an arm wrestling match. Another major milestone of the field is that the first commercially developed device including EAP materials that was produced in 2002 by Eamex in Japan [139]. This device was a fish that is able to swim on its own, moving its tail using an EAP muscle.

1.6.2 Type of EAPs

Table 1.3 summarizes the advantages and disadvantages of electronic EAPs and ionic EAPs. Generally, EAPs can be categorized into two types based on their actuation mechanism, which is electronic EAPs (dry) and ionic EAPs (wet) [126, 127, 131-133, 139-142]. Electronic EAPs actuate due to forces from the shift or motion of electrical

charge (driven by electric field); or Maxwell forces. Meanwhile, ionic EAPs function in an electrochemical system and require liquid electrolytes for ion transport or diffusion of ion. Ionic EAPs are inconvenient for practical application as most of them require a liquid medium to maintain their wetness, and a high-standard safety encapsulation is required for the liquid electrolyte.

Table 1.3 Characteristics of electronic and ionic EAPs.

Type	Advantages	Disadvantages
Electronic EAPs	◆ Operation in room conditions is available for a long time ◆ Exhibit rapid response (ms) ◆ Can withstand strain upon DC application ◆ Generates relatively large actuation forces ◆ Exhibits high mechanical energy density	◆ Requires high voltages ◆ Requires compromise between strain and stress ◆ Glass transition temperature is inadequate for low temperature actuation tasks ◆ Independent of the voltage polarity, it produces majorly monopolar actuation due to associated electrostriction effect
Ionic EAPs	◆ Requires low voltages ◆ Provides mostly bending actuation ◆ Generates large bending deformations ◆ Bi-directional actuation depends on the voltage polarity ◆ Some ionic EAPs such as conducting polymers (CPs) have a unique capability of bi-stability	◆ Most of ionic EAPs cannot withstand strain upon DC application, except for CPs ◆ Slow response (fraction of a second) ◆ Generates relatively low actuation forces ◆ Requires using an electrolyte medium ◆ Requires encapsulation or protective layer for open air operation

In this study, we focused on electronic EAPs as they can function in a dry environment and are appropriate for practical applications. Dielectric elastomers and electrostrictive elastomers are some of the examples of electronic EAPs. They can be

applied for actuator materials, sensors, artificial muscles, smart devices, and microswitches [126, 133, 143, 144]. Materials that can directly convert different types of energy into mechanical energy are normally known as actuator materials [133].

1.6.3 EAP actuator

Generally, soft, flexible, and multifunctional polymers are selected as the matrix material for EAPs. Furthermore, conducting fillers such as CNTs, carbon black, or conducting polymers such as polypyrrole are incorporated into the polymer matrix, not only to improve their mechanical properties but mainly their electrical properties. Commonly, EAP actuators are evaluated by measuring their bending displacement upon the application of voltage. Fig. 1.8 shows the experimental setup we used in order to measure bending displacement in this study.

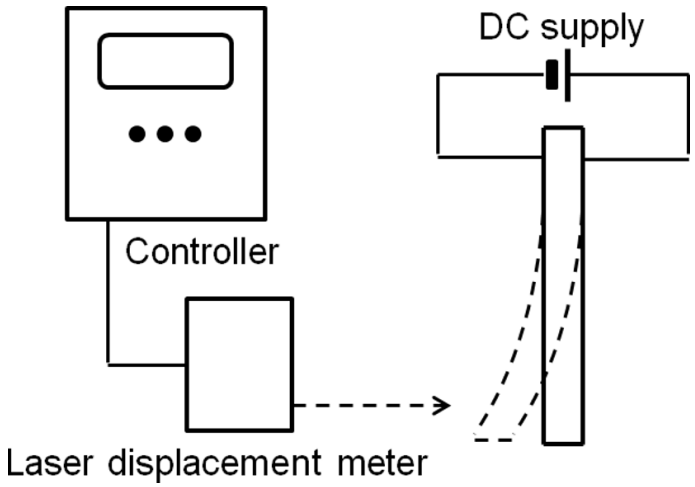

Fig. 1.8 Measurement of bending displacement.

PU has been used widely in the development of EAPs actuator. For instance, Petit et al. prepared carbon black filled PU films, and the strains induced by their composites films were believed triggered due to the Maxwell effect [145]. Jo et al. [127] and Nakama et al. [148] studied PU-based actuators with various polyols and fullerenol doped PU elastomer, respectively. The bending displacement under the application of an electric field was measured. Kofod et al. studied the actuation response of polyacrylate dielectric elastomers, and also discussed the Maxwell pressure [146]. In another study, Sahoo et al. investigated the influence of CNTs on electroactive shape memory properties of PU nanocomposites [125]. Chen et al. reported the electrothermal actuation of dielectric elastomers based on CNTs dispersed in silicone elastomer [129].

CNTs are well accepted as great fillers to be incorporated in polymer matrix for the development of EAPs.

Maxwell pressure is an essential parameter in the actuation of polymeric materials (dielectric materials). Maxwell pressure can be assumed as the compressive stress in the thickness direction that, which changes the width and length of the samples when voltage is applied [138,145-147]. The equation for the generated Maxwell pressure is:

$$p = \varepsilon_0 \varepsilon_r E^2, \tag{1.3}$$

where ε_0 is the vacuum permittivity, ε_r is the relative permittivity, and E is the applied electric field. From this equation, a higher relative permittivity will produce a higher Maxwell pressure if the vacuum permittivity and the applied electric field are constant. Therefore, highly polarized dielectric materials are considered to be vital in the actuation of EAP actuators.

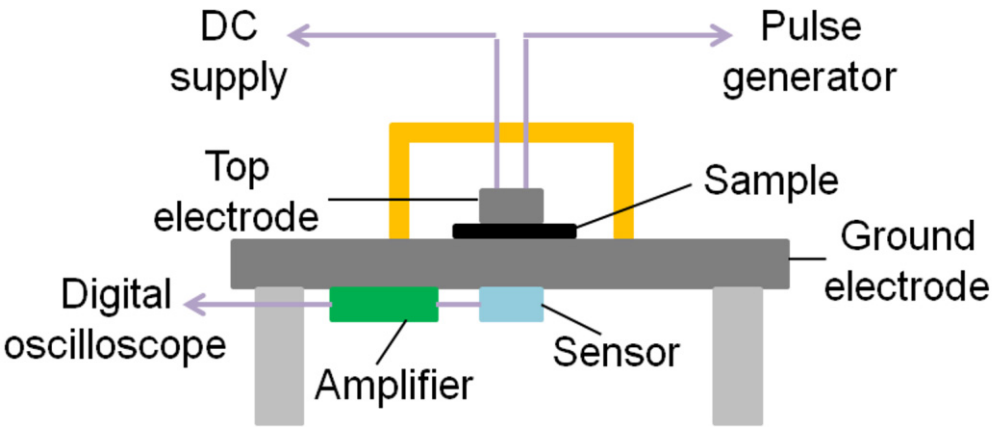

Fig. 1.9 Experimental setup for space charge measurement.

Watanabe et al. reported that bending direction of the PU films they prepared depends highly on the chemical structure of PU [128]. Bending deformation was measured, and charge transfer (space charge measurement) and accumulation within the samples when voltage is applied are discussed. In their another report, PU films doped with electron acceptors showed enhanced actuation and charge distribution and accumulation that was evaluated using space charge measurement were discussed once again [149]. Ali et al. also reported the charge accumulation within their polyvinyl chloride gel actuator and

discussed the relationship with actuation when voltage is applied [143]. Investigation by Yoshino et al. related to electrical conduction in polymers explained the phenomenon of charge accumulation in polymers [150]. Generally, space charge measurement is conducted using a pulsed electroacoustic non-destructive test system. Fig. 1.9 shows the experimental setup for space charge measurement. When a pulsed voltage is applied to the films, they deform instantaneously and produce an elastic wave within the materials. If charge exists within the films, the Coulomb force of the charge will produce an elastic wave. This elastic wave will be detected by a sensor and will be observed as amplitude that depends on the amount of charge.

1.7 Purposes and significances of research

The purposes of this study are to fabricate and characterize the nanocomposites we prepared. The main materials we used in this study are CNTs, BTO nanoparticles, and Ag nanoparticles, and their hybrid nanocomposites (BTO/CNT, Ag/CNT). First, we undertake the challenges to overcome the problem of CNTs dispersion in organic solvents. Then, we synthesized BTO and Ag nanoparticles and grafted them onto the surface of CNTs. The main characterization in this study is divided into two; EM wave absorber materials and EAPs actuator. These two characterizations are highly associated with the electrical properties of the nanocomposites.

In the development of EM wave absorber material, we investigated the factors that affect the absorption ability of the materials, such as the weight fraction of fillers, thickness, and multilayer design. The purpose of this investigation is to design absorber materials which possess high absorption ability and broad absorption frequency. In the same time, we also discussed the EM wave absorption mechanism. We applied hybrid nanocompsoites, BTO/CNT and Ag/CNT for the usage of EM wave absorber materials. The significance of fabricating and evaluating the EM wave absorber is to protect electronic devices and human beings from excessive EM radiation.

Meanwhile, in the development of EAPs actuator, we incorporated highly dispersed (after modification) CNTs into PU matrix and fabricated them into soft and flexible films. Their actuation behaviors upon the application of voltage were observed and we tried to clear and understand their actuation mechanism. The purpose of this study is to fabricate EAPs actuator with high performance that can be applied for practical application in the future. The significance of this investigation can lead to realization of

advanced materials for application in artificial muscles technology. Furthermore, they also can be applied for actuator materials, smart devices, sensors, microswitches, and so on.

1.8 Outline of dissertation

This dissertation is structured to provide a summary of "Development of CNT-based functional nanocomposites and their applications".

In Chapter 1, an overview of nanotechnology, nanocomposites, nanomaterials, EM wave absorber, and EAP actuator has been presented.

In Chapter 2, BTO nanoparticles were fabricated using sol-gel method and then grafted onto the surface of CNTs to prepare BTO/CNT hybrid nanomaterials. The evaluation of EM wave absorption properties was conducted.

In Chapter 3, BTO/CNT was incorporated into PU matrix to fabricate double-layer BTO/CNT nanocomposites. Significant results of EM wave absorption ability were obtained from double-layer structure than that of single-layer nanocomposite absorbers.

In Chapter 4, Ag nanoparticles were synthesized using chemical reduction process and then grafted onto the surface of CNTs to prepare Ag/CNT hybrid nanomaterials. EM wave absorption properties were investigated and discussed.

In Chapter 5, polymer-based electroactive nanocomposite actuators were fabricated by incorporating microwave-induced polymerization treated CNTs into PU matrix. The modification of CNTs was successful and significant bending actuation was obtained. The actuation behavior was discussed and actuation mechanism was proposed.

In Chapter 6, nanocomposite actuator films were fabricated using PU as the matrix and mild hydrothermally treated CNTs as the filler. The mild hydrothermally treated CNTs were highly dispersed in a polar solvent and PU matrix. The films bent toward the cathode side when voltage was applied and reverted back to almost their original position when voltage was removed. Reasonable explanation of the actuation behavior and mechanism were reviewed.

In Chapter 7, summary and conclusions of this dissertation were presented.

References

[1] The National Nanotechnology Initiative Strategic Plan, Nanoscale Science, Engineering, and Technology Subcommitee, Committee on Technology, National Science and Technology Council, Arlington, VA, December 2004.

[2] J. H. Koo, McGraw-Hill, New York, 2006.

[3] National Nanotechnology Initiative, http://www.nano.gov.

[4] M. J. Madou, Vol. 3, CRC Press, Boca Raton, 2012.

[5] N. Taniguchi, Proc. Intl. Conf. Prod. Eng. Tokyo, Part II, Japan Society of Precision Engineering, 1974.

[6] H. Hu, L. Onyebueke, A. Abatan, J. Miner. Mater. Charact. Eng. 9(4) (2010) 275-319.

[7] R. J. Young, P. A. Lovell, CRC Press, Boca Raton, 2011.

[8] K. Matyjaszewski, M. Moller, K. Mullen, C. K. Ober, Vol. 8, Elsevier, Amsterdam, 2012.

[9] D. W. Schaefer, R. S. Justice, Macromolecules 40(24) (2007) 8501-8517.

[10] E. T. Thostenson, C. Li, T. W. Chou, Compos. Sci. Technol. 65 (2005) 491-516.

[11] O. Bayer, Angew. Chem. 59 (1947) 257-272.

[12] C. Hepburn, Elsevier Applied Science, London, 1992.

[13] G. J. H Melvin, Q. Q. Ni, T. Natsuki, Microelectron. Eng. 126 (2014) 9-12.

[14] G. J. H Melvin, Q. Q. Ni, T. Natsuki, Appl. Phys. A 117 (2014) 2043-2050.

[15] G. J. H Melvin, Q. Q. Ni, T. Natsuki, Polym. Compos. DOI: 10.1002/pc.23177.

[16] C.A. Randall, R.E. Newnham, L.E. Cross, “History of the first ferroelectric oxide, $BaTiO_3$” (2004) unpublished.

[17] M.M. Vijatovic, J.D. Bobic, B.D. Stojanovic, Sci. Sinter. 40 (2008) 155-165.

[18] M.M. Vijatovic, J.D. Bobic, B.D. Stojanovic, Sci. Sinter. 40 (2008) 235-244.

[19] T. Lee, N. Yao, H. Imai, I. A. Aksay, Langmuir 17 (2001) 7656-7663.

[20] Y. Mao, S. Banerjee, S. S. Wong, J. Am. Chem. Soc. 125 (2003) 15718-15719.

[21] B. Ertug, American Journal of Engineering Research (AJER) 2 (2013) 1-7.

[22] L. Jing, G. Wang, Y. Duan, Y. Jiang, J. Alloys Comp. 475 (2009) 862-868.

[23] X. Chen, G. Wang, Y. Duan, S. Liu, J. Alloys Comp. 453 (2008) 433-436.

[24] Y. F. Zhu, Y. Q. Fu, T. Natsuki, Q. Q. Ni, Polym. Compos. 34 (2013) 265-273.

[25] G. Wang, X. Chen, Y. Duan, S. Liu, J. Alloys Comp. 454 (2008) 340-346.

[26] Q. Yuchang, Z. Wancheng, L. Fa, Z. Dongmei, J. Magn. Magn. Mater. 323 (2011)

600-606.

[27] G. J. H. Melvin, Q. Q. Ni, T. Natsuki, J. Alloys Comp. 615 (2014) 84-90.

[28] C. Bi, M. Zhu, Q. Zhang, Y. Li, H. Wang, J. Nanosci. Nanotechnol. 11 (2011) 1030-1036.

[29] X. Huang, Z. Chen, L. Tong, M. Feng, Z. Pu, X. Liu, Mater. Lett. 111 (2013) 24-27.

[30] Y. F. Zhu, L. Zhang, T. Natsuki, Y. Q. Fu, Q. Q. Ni, ACS Appl. Mater. Interfaces 4 (2012) 2101-2106.

[31] H. Thurnaurer, J. Deaderick, U.S. Patent No. 2,429,588 (1947); filed: 1941.

[32] E. Wainer, A.N. Solomon, Titanium Alloy Manufacturing Co. report No. 8 (September 1942) and No. 9 (January 1943).

[33] T. Ogawa, S. Waku (discovered 1944); T. Ogawa, Busseiron Kenkyu No. 6 (1947).

[34] B. WUl, J. M. Goldman, C. R. Acad. Sci. URSS 46, 139 (1945).

[35] B. I. Lee, M. Wang, D. Yoon, M. Hu, J. Ceram. Proc. Res. 4 (2003) 17-24.

[36] G. H. Haertling, J. Am. Ceram. Soc. 82 (1999) 797-818.

[37] V. Vinothini, P. Singh, M. Balasubramanian, Ceram. Int. 32 (2006) 99-103.

[38] M. Boulos, S. Guillemet-Fritsch, F. Mathieu, B. Durand, T. Lebey, V. Bley, Solid State Ionics 176 (2005) 1301-1309.

[39] H.S. Potdar, S.B. Deshpande, S.K. Date, Mater. Chem. Phys. 58 (1999) 121-127.

[40] L. Simon-Seveyrat, A. Hajjaji, Y. Emziane, B. Guiffard, D. Guyomar, Ceram. Int. 33 (2007) 35-40.

[41] L. Wang, L. Liu, D. Xue, H. Kang, C. Liu, J. Alloys Comp. 440 (2007) 78-83.

[42] B. Nowack, H. F. Krug, M. Height, Environ. Sci. Technol. 45 (2011) 1177-1183.

[43] K. M. M. A. El-Nour, A. Eftaiha, A. Al-Warthan, R. A. A. Ammar, Arabian J. Chem. 3 (2010) 135-140.

[44] Q. H. Tran, V. Q. Nguyen, A. T. Le, Adv. Nat. Sci.: Nanosci. Nanotechnol. 4 (2013) 033001.

[45] T. M. Tolaymat, A. M. E. Badawy, A. Genaidy, K. G. Scheckel, T. P. Luxton, M. Suidan, Sci. Total Environ. 408 (2010) 999-1006.

[46] C. M. Welch, R. G. Compton, Anal. Bioanal. Chem. 384 (2006) 601-619.

[47] M. C. Lea, Am. J. Sci. 37 (1889) 476-491.

[48] C. Paal, Ber. Dtsch. Chem. Ges. 35(2) (1902) 2224-2236.

[49] K. Boose, Dtsch. Z. Chir. 163 (1921) 62-84.

[50] N. E. Bogdanchikova, A. V. Kurbatov, V. V. Tret'yakov, P. P. Rodionov, Pharm.

Chem. J. 26 (1992) 778-779.

[51] H. Bechhold, Z. Chem. Ind. Kolloide 2 (1907) 3-9-33-41.

[52] Z. V. Moudry, U.S. Patent No. 2,927,052 (1953).

[53] M. Manes, U.S. Patent No. 3,374,608 (1968).

[54] G. Khomutov, S. Gubin, Mater. Sci. Eng. C 22 (2002) 141-146.

[55] M. Oliveira, D. Ugarte, D. Zanchet, A. Zarbin, J. Colloid Interface Sci. 292 (2005) 429-435.

[56] E. Egorova, A. Revina, Colloids Surf. A: Physicochem. Eng. Aspects 168 (2000) 87-96.

[57] F. Mafune, J. Kohno, Y. Takeda, T. Kondow, H. Sawabe, J. Phys. Chem. B 104 (2000) 9111-9117.

[58] T. Tsuji, K. Iryo, N. Watanabe, M. Tsuji, Appl. Surf. Sci. 202 (2002) 80-85.

[59] T. Tsuji, T. Kakita, M. Tsuji, Appl. Surf. Sci. 206 (2003) 314-320.

[60] Y. H. Chen, C. S. Yeh, Colloids Surf. A: Physicochem. Eng. Aspects 197 (2002) 133-139.

[61] G. J. H. Melvin, Q. Q. Ni, Y. Suzuki, T. Natsuki, J. Mater. Sci. 49 (2014) 5199-5207.

[62] J. Natsuki, T. Natsuki, T. Abe, J. Nanopart. Res. 15 (2013) 1483.

[63] J. Natsuki, T. Abe, J. Colloid Interface Sci. 359 (2011) 19-23.

[64] S. H. Lee, C. C Teng, C. C. M. Ma, I. Wang, J. Colloid Interface Sci. 364 (2011) 1-9.

[65] V. V. Mody, R. Siwale, A. Singh, H. R. Mody, J. Pharm. Bioallied Sci. 2 (2010) 282-289.

[66] M. Bosetti, A. Masse, E. Tobin, M. Cannas, Biomaterials 23 (2002) 887-892.

[67] G. V. Ramesh, K. Sudheendran, K. C. J. Raju, B. Shreedhar, T. P. Radhakrishnan, J. Nanosci. Nanotechnol. 9 (2009) 261-266.

[68] D. L. Zhao, X. Li, Z. M. Shen, Mater. Sci. Eng. B 150 (2008)105-110.

[69] D. L. Zhao, X. Li, Z. M. Shen, Compos. Sci. Technol. 68 (2008) 2902-2908.

[70] M. J. O'Connell, CRC Press, Boca raton, 2012.

[71] D. Hecht, VDM Verlag Dr. Muller, Saarbrucken, 2008.

[72] C. Hierold, Vol. 8, Wiley-VCH, Weinheim, 2008.

[73] R. Saito, G. Dresselhaus, M. S. Dresselhaus, Imperial college Press, London, 1998.

[74] D. Tasis, N. Tagmatarchis, A. Bianco, M. Prato, Chem. Rev. 106 (2006) 1105-1136.

[75] Z. Spitalsky, D. Tasis, K. Papagelis, C. Galiotis, Prog. Polym. Sci. 35 (2010)

357-401.

[76] M. Moniruzzaman, K. I. Winey, Macromolecules 39 (2006) 5194-5205.

[77] N. G. Sahoo, S. Rana, J. W. Cho, L. Li, S. H. Chan, Prog. Polym. Sci. 35 (2010) 837-867.

[78] J. N. Coleman, U. Khan, W. J. Blau, Y. K. Gun'ko, Carbon 44 (2006) 1624-1652.

[79] P. C. Ma, N. A. Siddiqui, G. Marom, J. K. Kim, Composites: Part A 41 (2010) 1345-1367.

[80] M. Rahmat, P. Hubert, Compos. Sci. Technol. 72 (2011) 72-84.

[81] R. Andrews, M. C. Weisenberger, Curr. Opin. Solid State Mater. Sci. 8 (2004) 31-37.

[82] E. T. Thostenson, Z. Ren, T. W. Chou, Compos. Sci. Technol. 61 (2001) 1899-1912.

[83] L. Hu, D. S. Hecht, G. Gruner, Chem. Rev. 110 (2010) 5790-5844.

[84] V. N. Popov, Mater. Sci. Eng., R 43 (2004) 61-102.

[85] X. L. Xie, Y. W. Mai, X. P. Zhou, Mater. Sci. Eng., R 49 (2005) 89-112.

[86] K. Matyjaszewski, M. Moller, E. Kumacheva, T. P. Russell, Vol. 7, Elsevier, Amsterdam, 2012.

[87] H. W. Kroto, J. R. Heath, S. C. O'Brien, R.F. Curl, R. E. Smalley, Nature 318 (1985) 162-163.

[88] S. Iijima, Nature 354 (1991) 56-58.

[89] S. Iijima, T. Ichihashi, Nature, 363 (1993) 603-605.

[90] P. M. Ajayan, O. Stephan, C. Colliex, D. Trauth, Science 265 (1994) 1212-1214.

[91] P. Seville, Review of radar absorbing materials, Defense Research and Development Atlantic Dartmouth, Canada (2005).

[92] N. V. Machinerieen, FR Patent 802728 (1936).

[93] W. W. Salisbury, U.S. Patent 2599944 (1952).

[94] O. Halpern, U.S. Patent 2923934 (1960)

[95] O. Halpern, M. H. J. Johnson, R. W. Wright, U.S. Patent 2951247 (1960).

[96] P. Dixon, Emerson & Cuming Microwave Products, white papers (2012).

[97] RF Products, Microwave absorbing materials, Laird Technologies.

[98] Microwave absorbing materials solution, Laird Technologies.

[99] F. Qin, C. Brosseau, J. Appl. Phys. 111 (2012) 061301.

[100] J. Huo, L. Wang, H. Yu, J. Mater. Sci. 44 (2009) 3917-3927.

[101] A. N. Yusoff, M. H. Abdullah, S. H. Ahmad, S. F. Jusoh, A. A. Mansor, S. A. A. Hamid, J. Appl. Phys. 92 (2002) 876-882.

[102] V. M. Petrov, V. V. Gagulin, Inorg. Mater. 37 (2001) 93-98.

[103] H. L. Zhu, Y. J. Bai, R. Liu, N. Lun, Y. X. Qi, F. D. Han, X. L. Meng, J. Q. Bi, R. H. Fan, AIP Adv. 1 (2011) 032140.

[104] S. M. Wentworth, John Wiley & Sons, Hoboken, 2005.

[105] J. H. Kim, S. S. Kim, J. Alloys Comp. 509 (2011) 4399-4403.

[106] C. Cui, Y. Du, T. Li, X. Zheng, X. Wang, X. Han, P. Xu, J. Phys. Chem. B 116 (2012) 9523-9531.

[107] S. Yamada, E. Otsuki, J. Appl. Phys. 81 (1997) 4791-4793.

[108] T. H Ting, Y. N Jau, R. P. Yu, Appl. Surf. Sci. 257 (2012) 3184-3190.

[109] W. Zhang, W. Li, J. Wang, C. Qin, L. Dai, Fibers Polym. 11 (2010) 1132-1136.

[110] G. W. Yang, G. Y. Gao, C. Wang, C. L. Xu, H. L. Li, Carbon 46 (2008) 747-752.

[111] R. X. Dong, C. T. Liu, K. C. Huang, W. Y. Chiu, K. C. Ho, J. J. Lin, ACS Appl. Mater. Interfaces 4 (2012) 1449-1455.

[112] K. Matyjaszewski, M. Moller, T. Hashimoto, H. W. Spiess, M. Takenaka, Vol. 2, Elsevier, Amsterdam, 2012.

[113] X. F. Zhang, X. L. Dong, H. Huang, B. Lv, J. P. Lei, C. J. Choi, J. Phys. D: Appl. Phys. 40 (2007) 5383-5387.

[114] H. Wu, L. Wang, S. Guo, Z. Shen, Appl. Phys. A 108 (2012) 439-446.

[115] K. J. Kim, S. Tadokoro, Springer, 2007.

[116] M. Haghayegh, G.M.M. Sadeghi, Polym. Compos. 33 (2012) 843-849.

[117] D. Ratna, J. Karger-Kocsis, J. Mater. Sci. 43 (2008) 254-269.

[118] Y. Liu, H. Lv, X. Lan, J. Leng, S. Du, Compos. Sci. Technol. 69 (2009) 2064-2068.

[119] C. Liu, H. Qin, P.T. Mather, J. Mater. Chem. 17 (2007) 1543-1558.

[120] J. Ding, Y. Zhu, Y. Fu, Polym. Compos. 35 (2014) 412-417.

[121] T. Ohki, Q.Q. Ni, N. Ohsako, M. Iwamoto, Composites Part A 35 (2004) 1065-1073.

[122] C.S. Zhang, Q.Q. Ni, Compos. Struct. 78 (2007) 153-161.

[123] B. Xu, Y.Q. Fu, M. Ahmad, J.K. Luo, W.M. Huang, A. Kraft, R. Reuben, Y.T. Pei, Z.G. Chen, J.Th.M. De Hosson, J. Mater. Chem. 20 (2010) 3442-3448.

[124] N.G. Sahoo, Y.C. Jung, N.S. Goo, J.W. Cho, Macromol. Mater. Eng. 290 (2005) 1049-1055.

[125] N.G. Sahoo, Y.C. Jung, H.J. Yoo, J.W. Cho, Compos. Sci. Technol. 67 (2007) 1920-1929.

[126] R. Shankar, T.K. Ghosh, R.J. Spontak, Soft Matter 3 (2007) 1116-1129.

[127] N.J. Jo, D.H. Lim, G.M. Bark, H.H. Chun, I.W. Lee, H. Park, J. Mater. Sci. Technol. 26 (2010) 763-768.

[128] M. Watanabe, N. Wakimoto, H. Shirai, T. Hirai, J. Appl. Phys. 94 (2003) 2494-2497.

[129] L.Z. Chen, C.H. Liu, C.H. Hu, S.S. Fan, Appl. Phys. Lett. 92 (2008) 263104.

[130] K.Y. Cho, H.G. Lim, S.R. Yun, J. Kim, K.S. Kang, J. Phys. Chem. C 112 (2008) 7001-7004.

[131] X. Zhang, C. Lowe, M. Wissler, B. Jahne, and G. Kovacs, Adv. Eng. Mater. 7 (2005) 361-367.

[132] Z. Cai, J. Kim, J. Appl. Polym. Sci. 115 (2010) 2044-2049.

[133] L. Chen, C. Liu, K. Liu, C. Meng, C. Hu, J. Wang, S. Fan, ACS Nano 5 (2011) 1588-1593.

[134] W. C. Roentgen, Section III in G. Wiedemann (Ed.), Annual Physics and Chemistry Series 11 (1880) 771-786.

[135] M. P. Sacerdote, J. Phys. 3, 31 (1899) 282-285.

[136] M. Eguchi, Philos. Mag. 49 (1925) 178.

[137] H. Kawai, Jpn. J. Appl. Phys. 8 (1969) 975-976.

[138] R.E. Pelrine, R.D. Kornbluh, J.P. Joseph, Sens. Actuators, A 64 (1998), 77-85.

[139] Y. Bar-Cohen, 2nd edition, SPIE Press, Washington, 2004.

[140] Y. Bar-Cohen, K. J. Kim, H. R. Choi, J. D. W. Madden, Smart Mater. Struc. 16 (2007) DOI: 10.1088/0964-1726/16/2/E01.

[141] Y. Bar-Cohen, Proceeding of Structure, Structural, Dynamics and Materials Conference, Seattle, Washington, Paper #2001-1492, 2001.

[142] Y. Bar-Cohen, Proceedings of Robotics 2000, New Mexico, 188-196, 2000.

[143] M. Ali, T. Hirai, J. Mater. Sci. 46 (2011) 7681-7688.

[144] M. Ali, T. Hirai, J. Mater. Sci. 47 (2012) 3777-3783.

[145] L. Petit, B. Guiffard, L. Seveyrat, D. Guyomar, Sens. Actuators, A 148 (2008), 105-110.

[146] G. Kofod, R. Kornbluh, R. Pelrine, P. Sommer-Larsen, J. Intell. Mater. Syst. Struct. 14 (2003) 787-793.

[147] B.M. O'Brien, E.P. Calius, T. Inamura, S.Q. Xie, I.A. Anderson, Appl. Phys. A 100 (2010) 385-389.

[148] Y. Nakama, J. Kyokane, K. Tokugi, T. Ueda, K. Yoshino, Synth. Met. 135-136

(2003) 749–750.

[149] M. Watanabe, Polym. Int. 56 (2007) 1265-1271.

[150] K. Yoshino, Y. Inuishi, Oyo Buturi 49 (1980) 212-227.

Chapter 2

****

BTO/CNT hybrid nanocomposites EM wave absorber

****

2 BTO/CNT hybrid nanocomposites EM wave absorber

2.1 Introduction

In recent years, the development of communication appliances and electronic tools in scientific, commercial, industrial, and military fields, such as navigation systems, computers, mobile phones, radar technology and wireless network systems is progressing fast [1-8]. Although these technologies are convenient, electromagnetic (EM) radiation has restricted their advancement and is becoming a serious crisis. EM radiation can harm the health of human beings, especially expectant mothers and children and pollute the environment [2, 4, 5, 7-10]. Thus, it is essential to defend human beings and electronic devices from excessive exposure to EM radiation. Therefore, the demand for EM wave absorber materials have increased and received much attention to effectively solve the problem of exposure to EM radiation. An ideal EM wave absorber material should be lightweight, strongly absorb EM waves, possess tunable absorption frequency, and multifunctionality [1, 5, 10].

Nanomaterials are among important candidates for EM wave absorber materials [5, 9, 11]. The relative density of nanomaterials is lower and their specific surface area is larger than those of the corresponding bulk materials. As a result, there are a large number of active atoms at the nanomaterials surface, which has a large interfacial dielectric loss induced by interface polarization [10]. Carbon nanotubes (CNTs) are light, possess a high aspect ratio and unique magnetic properties, and exhibit favorable mechanical, chemical and electric properties that have attracted considerable attention [1, 5-8, 12]. Their high electrical conductivity makes CNTs capable of dissipating electrostatic charges or shielding EM radiation [5-8, 12]. The ability to absorb EM wave can be optimized by synthesizing nanocomposites which includes the CNTs. Barium titanate (BTO) is one of the widely used materials for electric ceramics and has been applied for various of applications [2, 3, 13-15]. BTO perovskite possess high dielectric constant, good ferroelectric properties, and shows occurrence of relaxation at gigahertz frequencies [2, 3, 7, 8, 11, 13-19], thus a good candidate for the development of nanocomposites EM wave absorber. The combination of BTO with CNTs can integrate

the properties of these two components to form hybrid nanocomposites for use as EM wave absorber materials.

Reports on BTO/CNT hybrid materials as the EM wave absorbers are very limited. Bi et al. [6, 7] and Huang et al. [8] synthesized BTO/CNT compound by a solvothermal method and investigated their EM wave absorption properties. In their reports, the CNTs were oxidized with modification using strong acids treatment, which used harsh solvents and a time consuming process. In contrast, a mild hydrothermal treatment that is environment friendly, fast, efficient, and allows for easy modification has been performed [20]. No harsh organic or aqueous solvents were used in this process and it is thus a less destructive modification route. This treatment leads to the introduction of carboxyl and hydroxyl groups to the surface of the CNTs, which allows them to be highly dispersed in polar solvents and prevent agglomeration caused by strong intrinsic van der Waals attraction between the CNTs. Meanwhile, Wang et al. [14] fabricated BTO and carbon black compound via sol-gel method and also investigated the EM wave absorption properties. Sol-gel method is a widely used and classical fabrication approach, which offer a lot of inherent merits such as high purity, better homogeneity, lower temperature of preparation, and low manufacturing cost [17-19]. To the best of our knowledge, the evaluation of EM wave absorption properties of BTO/CNT hybrid nanocomposites, where the CNTs were mild hydrothermally treated, prepared using sol-gel method has not been examined.

In this chapter, we prepare BTO nanoparticles and graft them onto the surface of CNTs by using sol-gel method. We then evaluate the ability of these materials to absorb EM waves by measuring their dielectric and magnetic losses when penetrated by an EM wave. The complex permittivity and complex permeability of these hybrid nanocomposites are measured and their reflection loss is also calculated.

2.2 Materials and methods

2.2.1 Modification of CNTs

Multi-walled CNTs (Wako Pure Chemical Industries Ltd., Japan, d = 20-30 nm) were functionalized by mild hydrothermal treatment, as reported by our research group in Ref. [20], with some modifications. Pure water, potassium hydroxide (KOH), and potassium persulfate (KPS) were used in the treatment and they were also obtained from Wako Pure Chemical Industries Ltd., Japan.

CNTs were added to the aqueous solution of KOH and ultrasonically mixed in a stainless steel reaction autoclave with a polytetrafluoroethylene liner. KPS was added to the aqueous solution and ultrasonically mixed as a next step. The autoclave was then sealed and heated at 160°C for 2.0 h. Finally, the solutions were filtered and rinsed with pure water and ethanol for several times. The products were dried overnight in vacuum at 50°C. The mild hydrothermally treated CNTs were denoted as modified CNTs hereafter.

2.2.2 Preparation of BTO/CNT hybrid nanocomposites

BTO nanoparticles were prepared by sol-gel method and modified CNTs were mixed to prepare BTO/CNT hybrid nanocomposites. Barium acetate $Ba(CH_3COO)_2$, titanium tetraisopropoxide $Ti[(CH_3)_2CHO]_4$, acetic acid, ethanol, and pure water were obtained from Wako Pure Chemical Industries Ltd., Japan.

Barium acetate was dissolved in mixed solution of 20 ml ethanol and 3 ml acetic acid (solution A), stirred in water bath at 60°C for 0.5 h. In the same time, titanium tetraisopropoxide was mixed in 10 ml ethanol (solution B). Solution A and B were combined and 1 ml pure water was added to perform hydrolysis. Then these two solutions were stirred at 60°C for 2.0 h to form a sol, which contained Ba/Ti molar ratio 1:1. Next 0.15 g modified CNTs were added to the final solution, sonicated for 1.0 h, and stirred furthermore for 1.0 h. The mixture was then aged for 2 days and a black color gel was obtained. The gel was dried at at 100°C for 1.0 h to make a xerogel. Finally, the product was calcined at 800°C for 2.0 h. Samples for BTO were prepared using same process excluding the addition of modified CNTs.

2.2.3 Evaluation method

The crystal structure of prepared powders was analyzed by using X-ray diffraction (XRD; Rigaku Rotaflex, Japan) with Cu Kα radiation (λ = 0.15406 nm). The morphology was characterized using transmission electron microscopy (TEM; JEM-2100, JOEL, Japan) and field emission scanning electron microscopy (FE-SEM; Hitachi S-5000, Japan) with an accelerating voltage of 200 kV and 20 kV, respectively. Raman spectroscopy measurements were performed on a Raman spectrometer (HoloLab series 5000, Kaiser Optical Systems) with 532 nm laser excitation. Lorentzian fitting was conducted for the low Raman shift range. X-ray photoelectron spectroscopy (XPS; Kratos Axis Ultra DLD) was performed with a standard Mg Kα (1256.6 eV)

X-ray source operating at 10 mA and 15 kV to characterize the elemental composition and chemical states of the samples.

The real and imaginary parts of complex permittivity ε ($\varepsilon = \varepsilon' - j\varepsilon''$) and permeability μ ($\mu = \mu' - j\mu''$) were measured by scattering parameters measurement method in reflection mode using a vector network analyzer (37247D, Anritsu Co. Ltd.) within the frequency range of 0.5-13.8 GHz. Samples for these measurements were prepared by loading the BTO/CNT hybrid nanocomposites in paraffin wax with a weight fraction of BTO/CNT hybrid nanocomposites of 40, 50, and 60 wt.%. The powder-wax composites were pressed into a toroidal shape using a mold designed with an outer diameter of 7.0 mm, inner diameter of 3.0 mm, and thickness of 1.0 mm. The reflection loss was calculated from the measured complex permittivity and permeability of the samples. For comparison, the samples of BTO 60 wt.% and modified CNTs 20 wt.% were also fabricated with the same process.

2.3 Results and discussion

2.3.1 Structure and morphology of BTO/CNT hybrid nanocomposites

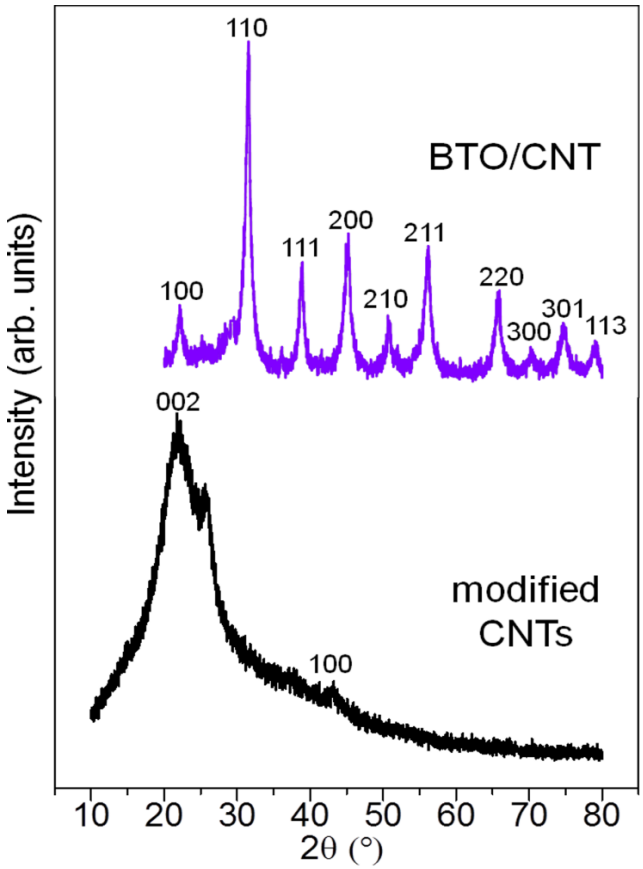

Fig. 2.1 XRD patterns of the modified CNTs and the BTO/CNT hybrid nanocomposites.

XRD patterns of the modified CNTs and BTO/CNT hybrid nanocomposites are shown in Fig. 2.1. All peaks of the BTO/CNT can be assigned to the cubic perovskite structure (JCPDS No. 31-0174) [8, 11, 13], and no split peak was observed around 2θ = 45° [3, 14]. Strong intensity of (110) peak can be observed from BTO/CNT hybrid nanocomposites at 2θ = 31.6°. The modified CNTs showed typical multi-walled CNTs (002) peak at 22° [21, 22] which overlapped with the (100) peak of BTO/CNT. Similar pattern of the modified CNTs also can be observed from the pristine CNTs sample (not shown in the figure). Even though the peak for CNTs in the BTO/CNT is not clear (overlapped), their existence was confirmed from the Raman and XPS spectra presented below. Using the Scherrer's equation as shown below [14]:

$$D = \frac{0.9\lambda}{\beta \cos\theta} \tag{2.1}$$

where D is the particle size, λ is the wavelength of the Cu Kα radiation (0.15406 nm), θ is the diffraction angle, and β is the full width at half maximum (FWHM) of the peak, average crystalline size of BTO nanoparticles were calculated to be 10.3 nm from the broadening of BTO/CNT (110) peak.

TEM and FE-SEM images of the BTO nanoparticles, modified CNTs, and BTO/CNT hybrid nanocomposites are depicted in Fig. 2.2. Fig. 2.2(a) shows the TEM image of BTO nanoparticles with spherical shape which exist in a bundle. Fig. 2.2(b) shows the TEM image of modified CNTs and no agglomeration was observed. The inset in Fig. 2(b) shows the TEM image of individual modified CNT and no obvious defect that might be caused from sonication and modification process was observed. Fig. 2.2(c)-(e) shows the TEM images of BTO/CNT hybrid nanocomposites where BTO nanoparticles were grafted onto the surface of CNTs. The shape of BTO nanoparticles was also spherical and they were strongly adhered to the surfaces of CNTs. From Fig. 2.2(d) and (e), the diameter of BTO nanoparticles was under 15 nm, ranging from 6 to 12 nm and this shows high similarity with the calculation using Scherrer's equation (10.3 nm). Fig. 2(e) further reveals that the BTO nanoparticle form a single crystal with crystal spacing ~0.28 nm corresponds to (110) crystal plane [11, 23, 24]. Fig. 2.2(f) shows the FE-SEM image of BTO/CNT hybrid nanocomposites where BTO nanoparticles were grafted onto the surface of CNTs was also observed.

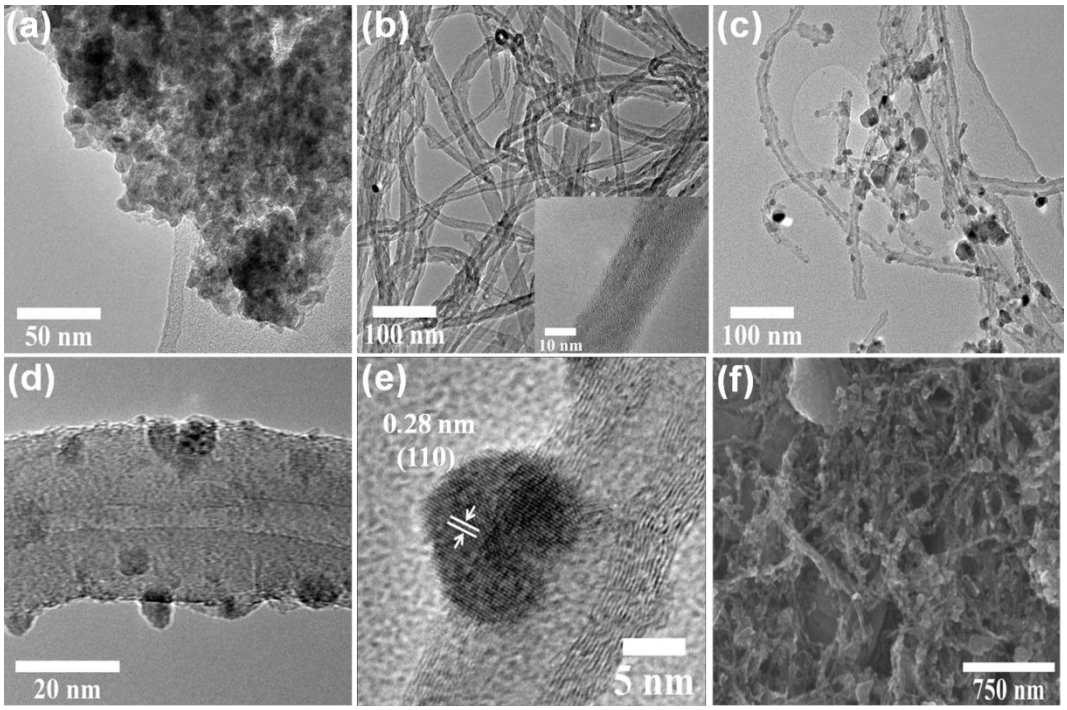

Fig. 2.2 TEM images of (a) BTO nanoparticles, (b) modified CNTs (inset: individual modified CNT), (c)-(e) BTO/CNT hybrid nanocomposites and FE-SEM image of (f) BTO/CNT hybrid nanocomposites.

Raman spectroscopy is an effective tool to probe structure at the atomic scale on the basis of vibrational symmetry. Cubic BTO inherently has no Raman active modes, but such modes are expected for the noncentrosymmetric tetragonal structure [11, 25, 26]. The Raman spectrum of BTO/CNT is shown in Fig. 2.3. From Fig. 2.3(a), the observed Raman peaks can be assigned to more than one phonon mode; sharp bands at ~313 cm^{-1} [B_1, E(TO+LO)] and ~756 cm^{-1} [A_1, E(LO)], broad bands at ~240 cm^{-1} [A_1(TO)], ~513 cm^{-1} [E, A_1 (TO)] and ~179 cm^{-1} [A_1(TO), E(LO)], all of which are suggestive of a tetragonal phase. Although XRD patterns reveal a cubic perovskite structure, a certain degree of tetragonal phase on the atomic scale from the products is expected [11, 25]. From the XRD and Raman spectroscopy, coexistence of cubic and tetragonal phase is possible [26]. The typical characteristic bands of CNTs was also observed from BTO/CNT hybrid nanocomposites, D band (defect) at ~1348 cm^{-1} and G band (graphite band) at ~1586 cm^{-1} [27, 28], as illustrated in Fig. 2.3(b). Furthermore, the relative intensity of the D and G bands (I_D/I_G) from the Raman spectroscopy is related to the amount of structural defects and sp^3-hybridized carbon atoms in a CNT sample, and thus provides direct information about the degree of sidewall functionalization [5, 27]. The D/G ratio is 1.02, 1.09, and 1.11 for the pristine CNTs, modified CNTs, and

BTO/CNT hybrid nanocomposites, respectively. The slight increase of the D/G ratio between the pristine CNTs and the modified CNTs shows that the structural defects are minimal and also indicates the successful introduction of functional groups onto the CNTs surface and that the outer layers of the CNTs were chemically modified [5, 20]. A slight increase between the D/G ratio of the modified CNTs and that of the BTO/CNT hybrid nanocomposites can be attributed to the introduction of BTO nanoparticles onto the surface of the CNTs.

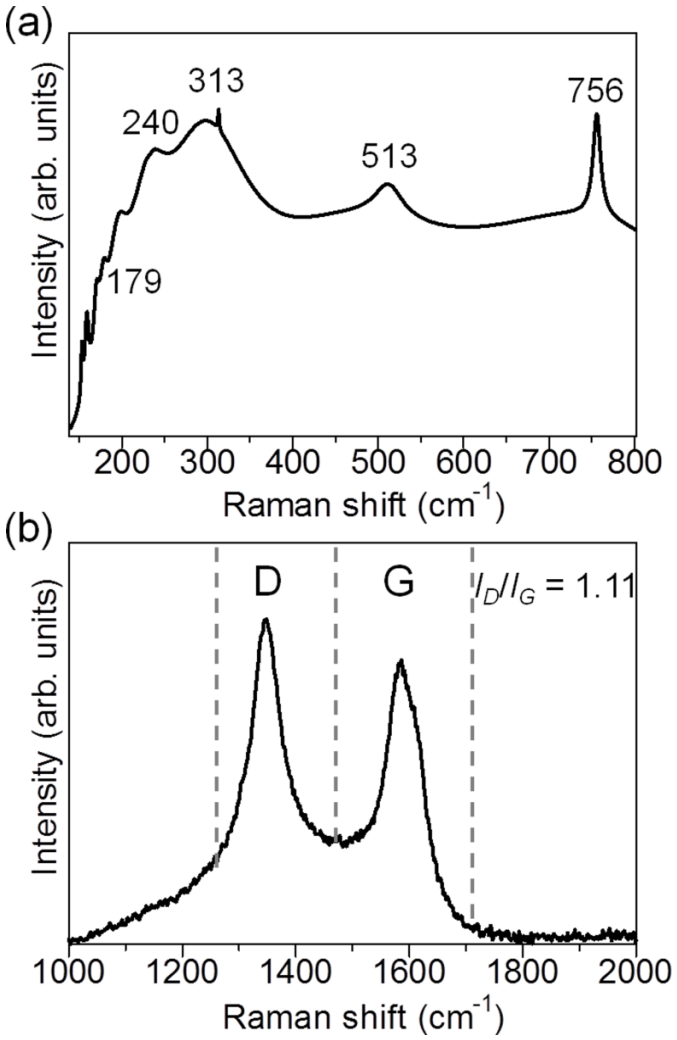

Fig. 2.3 Raman spectra (a) 150~800 cm^{-1} and (b) 1000~2000 cm^{-1} of BTO/CNT hybrid nanocomposites.

XPS evaluation was carried out to determine the elemental composition and functional groups of the modified CNTs and BTO/CNT hybrid nanocomposites, as shown in Fig. 2.4. The modified CNTs exhibited a strong carbon (C 1s) peak at 284 eV and oxygen (O 1s) peak at 531 eV. The modified CNTs showed an O 1s peak with

higher intensity than that of the pristine CNTs (not shown in the figure). The atomic percentage ratios for the pristine CNTs are 98.51% for C 1s and 1.49% for O 1s, while those of the modified CNTs are 92.87% for C 1s and 7.13% for O 1s. The higher intensity of the O 1s peak confirms that many oxygen functional groups (carboxyl and hydroxyl) were introduced onto the surface of the modified CNTs. The XPS survey spectrum of the BTO/CNT hybrid nanomaterials confirmed the presence of C 1s, O 1s, barium (Ba 3d, Ba 4d, Ba 4p, Ba 4s), and titanium (Ti 2p). The BTO/CNT samples showed a weaker peak of C 1s peak at 284 eV than that of modified CNTs after BTO nanoparticles were grafted onto the surface of CNTs and O 1s peak at 531 eV. Ba 3d peaks from Ba $3d_{5/2}$ and Ba $3d_{3/2}$ appeared at 780 and 795 eV, respectively. Ti 2p peaks from Ti $2p_{3/2}$ and Ti $2p_{1/2}$ appeared at 459 and 465 eV, respectively. The presence of Ba 3d, Ti 2p, and O 1s peaks proves the formation of BTO nanoparticles. The Ba $3d_{5/2}$ and Ti $2p_{3/2}$ binding energies measured for the BTO/CNT were in good agreement with those reported [11, 25]. The atomic percentage ratios for the BTO/CNT nanomaterials are 86.20% for C 1s, 6.22% for Ba 3d, and 7.58% for Ti 2p.

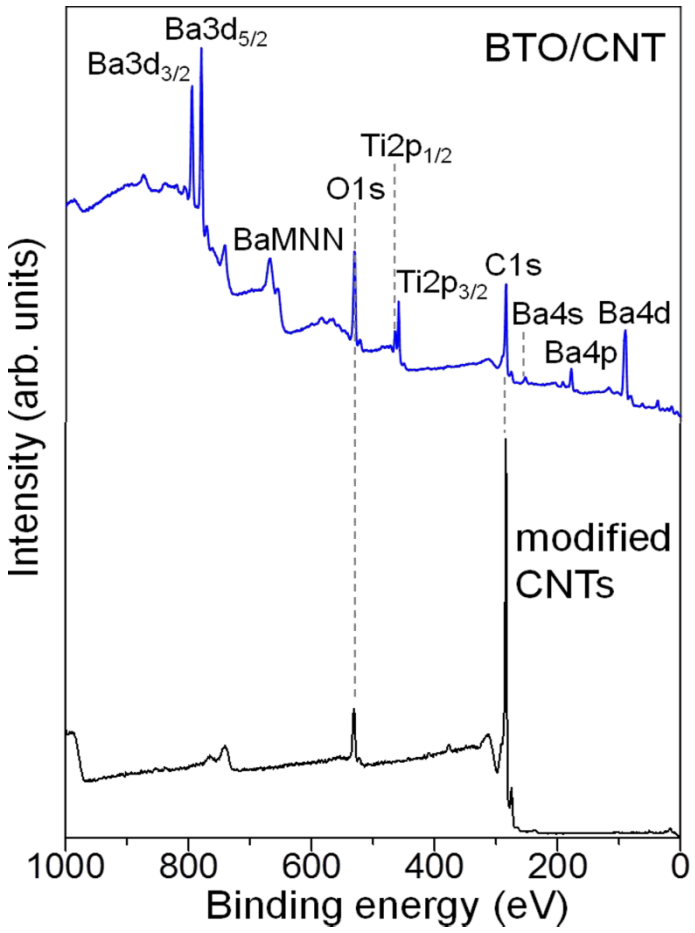

Fig. 2.4 XPS spectra of the modified CNTs and the BTO/CNT hybrid nanocomposites.

2.3.2 Electromagnetic wave absorption properties

Complex permittivity and complex permeability are basic parameters associated with the EM wave absorption properties of a material, where the real parts of complex permittivity and permeability represent the storage of electric and magnetic energies, respectively, while the imaginary parts symbolize the loss and dissipation of both energies [1, 5, 10, 13]. The complex permittivity (real part ε' and imaginary part ε'') and complex permeability (real part μ', imaginary part μ'') of the BTO/CNT nanocomposites loaded in paraffin wax in the range of 0.5-13.8 GHz are presented in Fig. 2.5 and 2.6, respectively.

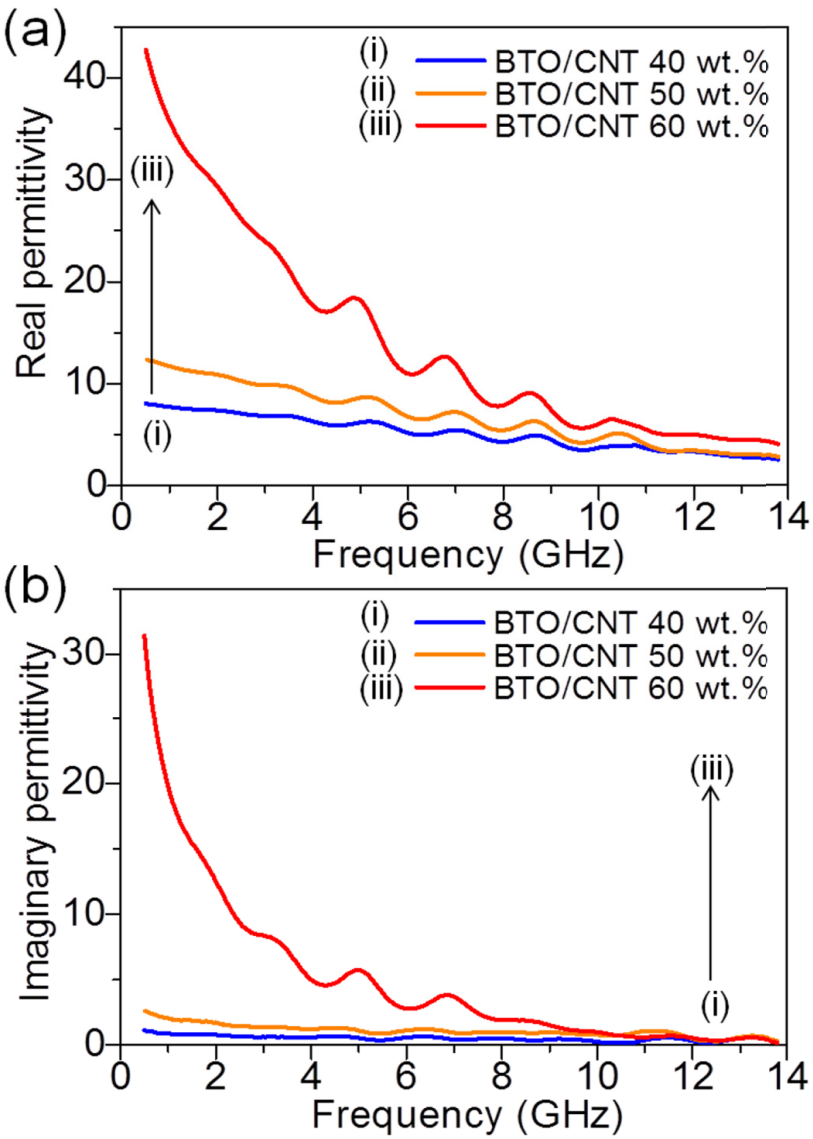

Fig. 2.5 Complex permittivity of the BTO/CNT 40~60 wt.% hybrid nanocomposites (t = 1.0 mm). (a) real part permittivity and (b) imaginary part permittivity.

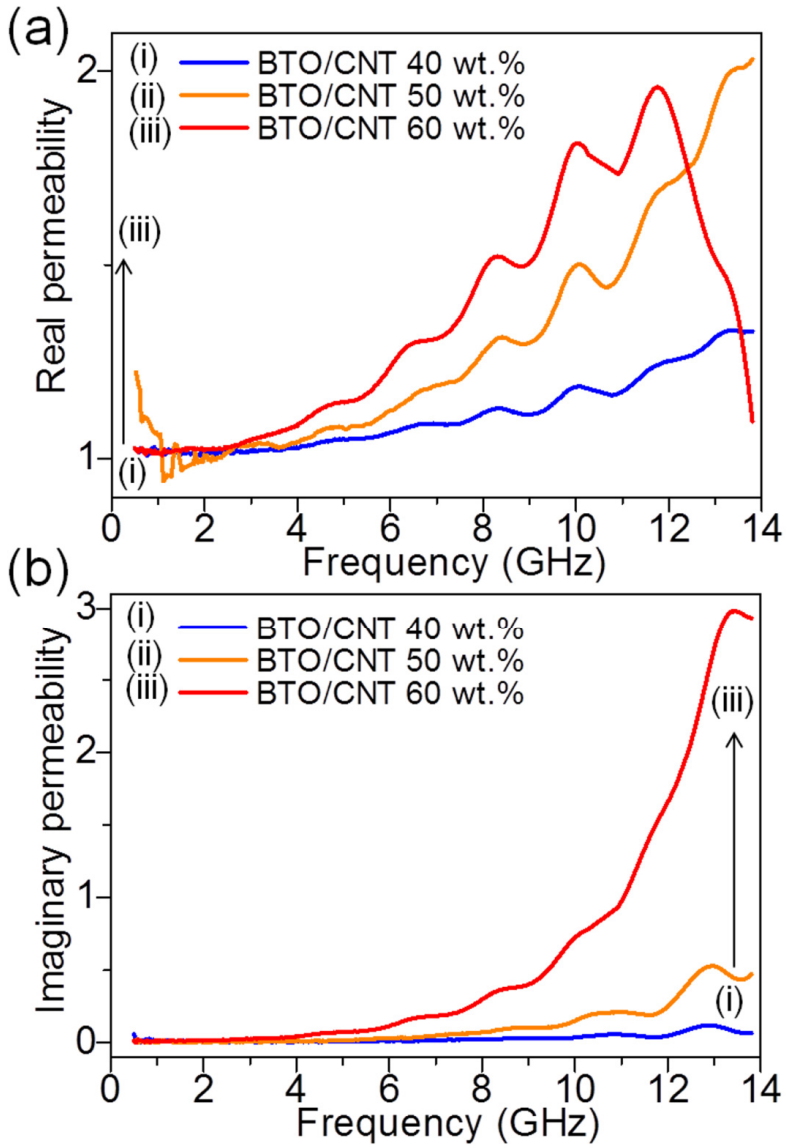

Fig. 2.6 Complex permeability of the BTO/CNT 40~60 wt.% hybrid nanocomposites (t = 1.0 mm). (a) real part permeability and (b) imaginary part permeability.

The samples are BTO/CNT 40, 50, and 60 wt.% with thickness, t = 1.0 mm. As the frequency increased, the complex permittivity decreased because the polarizabilities (electronic, ionic, and orientation) and electric displacement are not maintained in a changing EM field [2, 3, 5, 11, 13, 14]. Higher weight fraction of BTO/CNT hybrid nanocomposites shows higher complex permittivity. High ε'' of the BTO/CNT 60 wt.% indicates that this sample can cause dielectric loss, dominated primarily by dielectric polarization, spontaneous polarization, and associated relaxation phenomena [11, 14, 15]. Furthermore, with the inclusion of CNTs into BTO/CNT hybrid nanocomposites,

the high electrical conductivity of the CNTs enables strong polarization to occur, Ohmic losses, dissipation of electrostatic charges, or multiple scattering caused by the large specific area, which lead to improved complex permittivity [1, 5, 12]. For the complex permeability, as the frequency increased, the complex permeability also increased, except for μ' of BTO/CNT 60 wt.%. μ' of the BTO/CNT 60 wt.% increased until a certain frequency, after which it gradually decreased. This can be attributed to natural resonance or eddy current loss [10]. When conducting material (CNTs) was put in an alternating magnetic field, a close induced current will be produced inside the material, which would dissipate the energy and referred as eddy current loss [10]. CNTs possess high electrical conductivity and this leads to permeability decreasing rapidly at high frequency caused by the eddy current loss [5, 7]. Higher weight fraction of BTO/CNT hybrid nanocomposites also shows higher complex permeability.

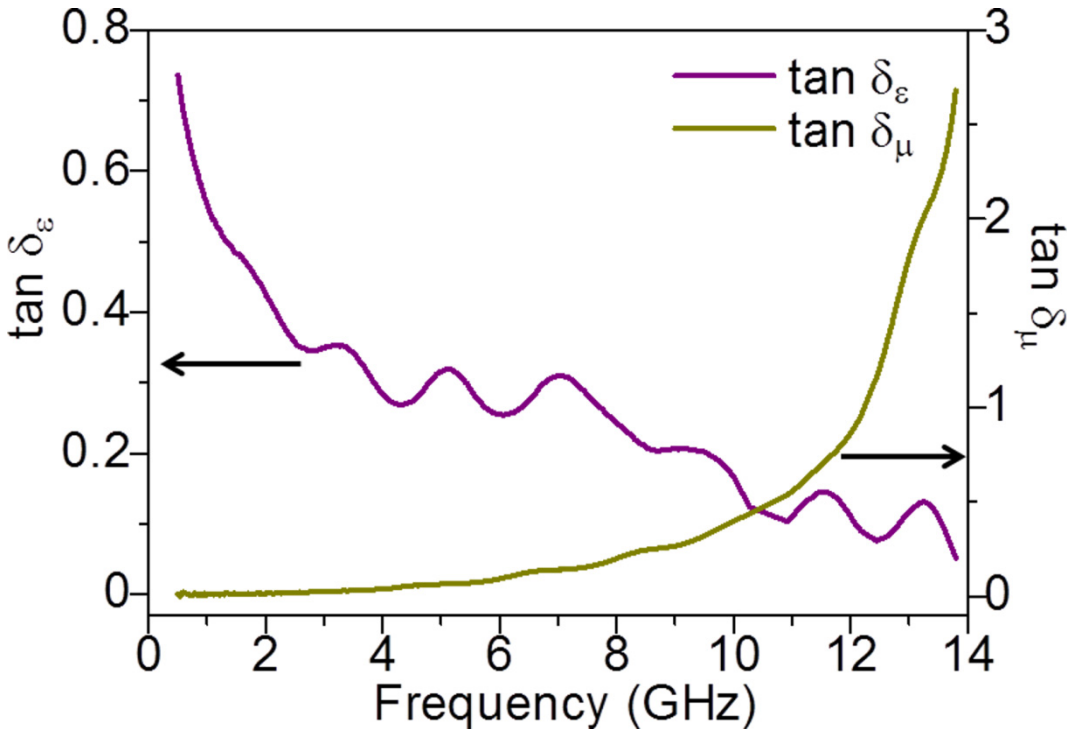

Fig. 2.7 Dielectric loss factor and magnetic loss factor of the BTO/CNT 60 wt.% hybrid nanocomposites with t = 1.0 mm.

To reveal the intrinsic reasons for the EM wave absorption by the BTO/CNT hybrid nanocomposites, their dielectric loss factor (tan $\delta_\varepsilon = \varepsilon''/\varepsilon'$) and magnetic loss factor (tan $\delta_\mu = \mu''/\mu'$) were evaluated. Fig. 2.7 presents tan δ_ε and tan δ_μ of the BTO/CNT 60 wt.% with t = 1.0 mm. The relaxation observed from tan δ_ε can be attributed from energy loss

in the materials illuminated by electromagnetic field comes about through damping forces acting on polarized atoms and molecules and trough the finite conductivity of the materials [1]. Both tan δ_ε and tan δ_μ contribute to the EM wave absorption; in the low-frequency region, tan δ_ε is sensitive to EM waves, and at high frequency, tan δ_μ is sensitive to EM waves.

To investigate the EM wave absorption properties of the samples, the reflection loss (*R.L.*) was calculated according to the transmission line theory as follows:

$$R.L. = 20 \log \left| \frac{Z_{in} - 1}{Z_{in} + 1} \right| \tag{2.2}$$

where the normalized input impedance (Z_{in}) is given by the formula,

$$Z_{in} = \sqrt{\frac{\mu_r}{\varepsilon_r}} \tanh \left[j \left(\frac{2\pi f d}{c} \right) \sqrt{\mu_r \varepsilon_r} \right] \tag{2.3}$$

where $\varepsilon_r = \varepsilon' - j\varepsilon''$, $\mu_r = \mu' - j\mu''$, f is the EM wave frequency (Hz), d is the thickness of the absorber (m), and c is the velocity of light in free space (m/s). *R.L.* of the BTO/CNT 40~60 wt.% with t = 1.0 mm are shown in Fig. 2.8. For comparison, *R.L.* of the BTO 60 wt.% (t = 1.0 mm) and modified CNTs 20 wt.% (t = 1.0 mm) were also included.

The BTO 60 wt.% showed a relatively low minimum *R.L.* of only ~-1.3 dB at 13.1 GHz. Conversely, the modified CNTs 20 wt.% showed a minimum *R.L.* of ~-11.6 dB at 9.8 GHz with a response bandwidth (*R.L.* of less than -10 dB, over 90% absorption) of 0.7 GHz (9.5-10.2 GHz). *R.L.* of the BTO/CNT hybrid nanocomposites increased as the weight fraction increased, but showed poor absorption for samples with weight fraction under 60 wt.%. Furthermore, the peak of the minimum *R.L.* was around 13.0 GHz and slightly shifted to higher frequency as the weight fraction increased. The BTO/CNT 60 wt.% showed a minimum *R.L.* of ~-29.6 dB (over 99.9% absorption) at 13.6 GHz. Furthermore, this sample also exhibited a wide response bandwidth of 1.7 GHz, where the frequency bandwidth (*R.L.* of less than -10 dB, over 90% absorption) is from 12.1 to 13.8 GHz.

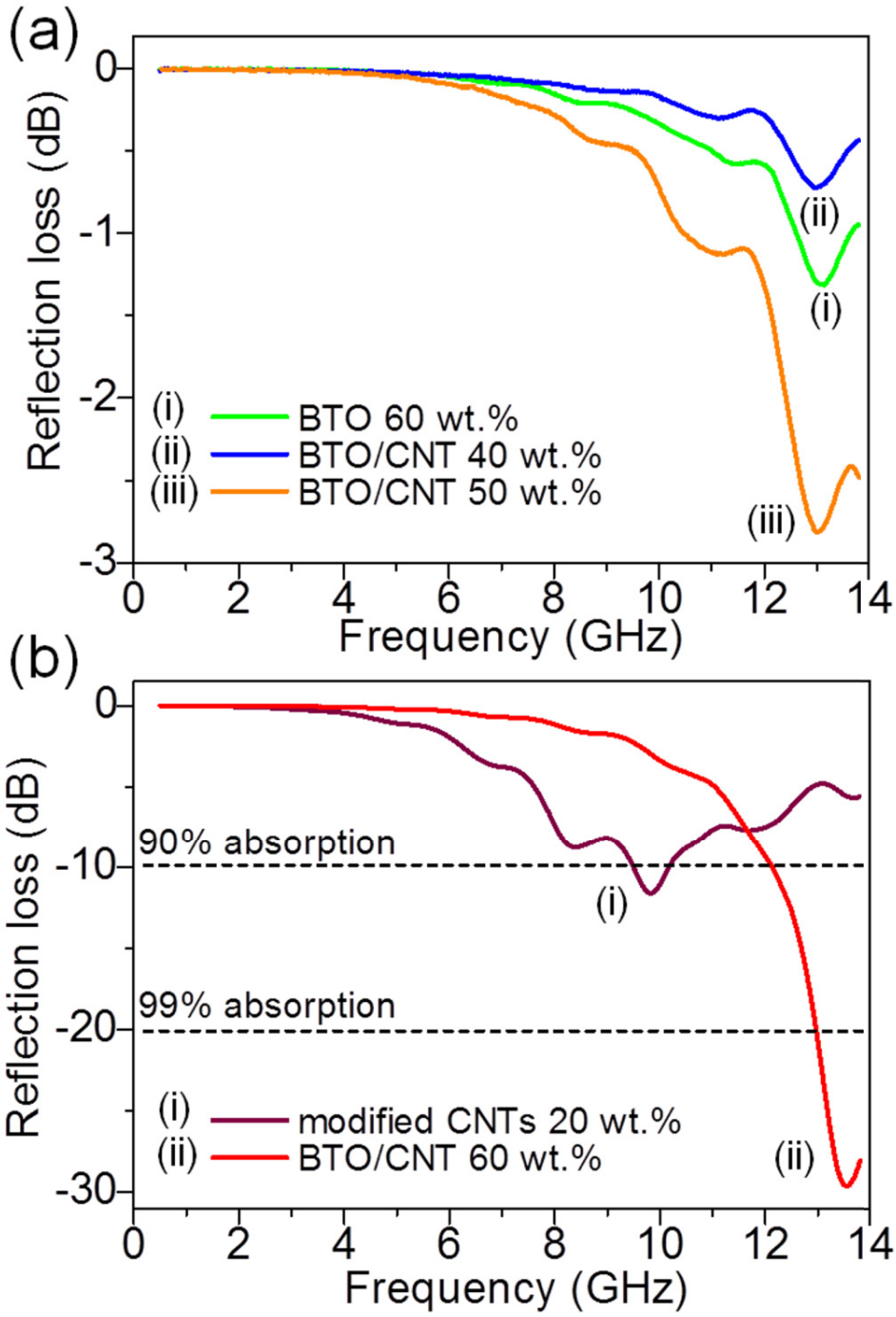

Fig. 2.8 Reflection loss (a) BTO 60 wt.% and BTO/CNT 40 and 50 wt.%; (b) modified CNTs and BTO/CNT 60 wt.% with t = 1.0 mm in the range of 0.5-13.8 GHz.

When the BTO nanoparticles were grafted onto the surface of CNTs, enhanced *R.L.* and wider response bandwidth were obtained. The BTO/CNT hybrid nanocomposites showed similar pattern of EM wave absorption with the BTO sample but improved in *R.L.*, which indicated that CNT contributed to the developed absorption ability of the

hybrid nanocomposites. BTO/CNT 60 wt.% was the best absorber when compared with the other samples and the results show that BTO/CNT hybrid nanocomposites are able to improve EM wave absorption than that of BTO or modified CNTs loaded samples.

At low weight fraction of BTO/CNT hybrid nanocomposites, the effect of EM wave absorption is not obvious. However, at high weight fraction (BTO/CNT 60 wt.%), enhanced complex permittivity and permeability contributed to the enhanced *R.L.* when EM wave transmits through the material. High weight fraction of the BTO/CNT hybrid nanocomposites made them to be able to polarize repeatedly at high frequency electric field, which causes the electric energy dissipated into other form of energy such as heat energy [2, 3, 14]. There are many boundaries in the BTO/CNT hybrid nanocomposites, including between the BTO surfaces and CNTs surfaces. The behavior of the EM wave absorption of the BTO/CNT hybrid nanocomposites can be attributed to the multiple interfacial polarizations between the BTO nanoparticles and CNTs. Moreover, because the CNTs were modified both prior to and during the process of BTO nanoparticles coating, the BTO/CNT hybrid nanocomposites may contain defects and suspended bonds, as shown in the Raman and XPS spectra of the samples (Fig. 2.3 and 2.4). As a result, the large specific areas of the surfaces of the hybrid nanocomposites triggered higher interfacial polarization, multiple scattering, and molecular polarization which leads to a high minimum *R.L.* [1, 5-7, 11, 12]. Interfacial multipoles contribute to the strong EM wave absorption of the hybrid nanocomposites. Furthermore, suitable complex permittivity and complex permeability are essential to promote EM wave absorption [1, 5, 10]. This also can be related to another important parameter connected to *R.L.*, *i.e.*, the concept of matched impedance. This concept suggests that the characteristic impedance of an absorber should be almost equal to that of the free space to achieve zero reflection on the front surface of the material [13, 15]. Obviously, to design an optimized absorber with a high minimum *R.L.*, appropriate EM impedance matching is important.

According to Eq. (2.3), the thickness of the absorber can also affect *R.L.*, so we investigated the relationship between the thickness and *R.L.* of the BTO/CNT 60 wt.% hybrid nanocomposites. *R.L.* for BTO/CNT 60 wt.% with t = 1.1, 1.2, 1.4, 1.6, 1.8, and 2.0 mm was calculated and shown in Fig. 2.9. When the thickness of the BTO/CNT 60 wt.% increased, the frequency of the *R.L.* peak decreased. The BTO/CNT hybrid nanocomposites with t = 1.1 mm showed a minimum *R.L.* of ~-56.5 dB (over 99.999% absorption) at 13.2 GHz and was the best absorber when compared with the other

samples of different thickness. Our hybrid nanocomposites showed superior *R.L.* in contrast to *R.L.* reported in Refs. [6-8], although preparation process and experimental conditions are varied. Furthermore, they also showed wide response bandwidth of 2.0 GHz (11.8–13.8 GHz). These results show that the frequency related to the minimum *R.L.* (highest absorption) of the BTO/CNT hybrid nanocomposites can be controlled by changing the thickness of the sample. Even though the minimum *R.L.* decreased as the thickness increased beyond 1.1 mm, the response bandwidth (*R.L.* of less than -10 dB, over 90% absorption) increased. The response bandwidth were 2.2, 2.6, 3.5, 3.9, and 5.3 GHz for t = 1.2~2.0 mm, respectively. We believe that the BTO/CNT hybrid nanocomposites are a promising EM wave absorber, because their absorption band can be modulated simply by manipulating the sample thickness to satisfy applications in different frequency bands.

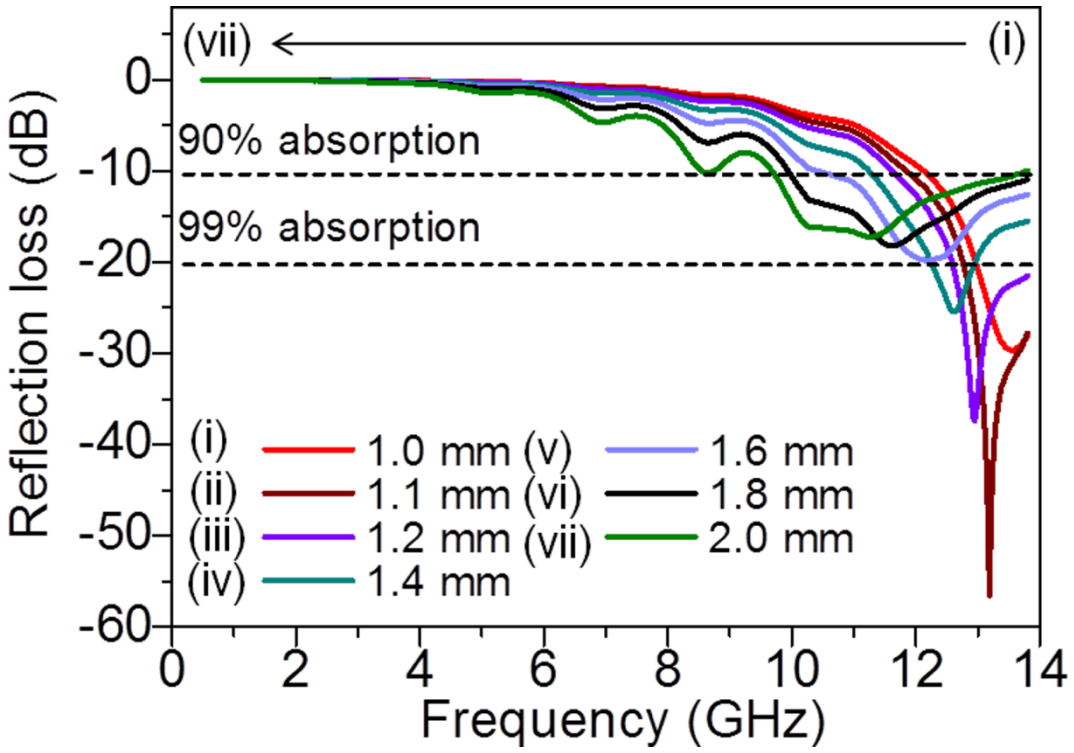

Fig. 2.9 Reflection loss of the BTO/CNT 60 wt.% hybrid nanocomposites (t = 1.0, 1.1, 1.2, 1.4, 1.6, 1.8 and 2.0 mm) in the range of 0.5-13.8 GHz.

2.4 Conclusions

BTO nanoparticles were grafted onto the surface of CNTs to fabricate BTO/CNT hybrid nanocomposites. XRD, TEM, FE-SEM, Raman and XPS spectroscopy analyses revealed the morphology, structure, and elemental composition of the hybrid

nanomaterials. The high interfacial area of the hybrid nanomaterials results in high interfacial polarization and multiple scattering, which improves EM wave absorption. The BTO/CNT 60 wt.% (t = 1.0 mm) hybrid nanomaterials exhibited a minimum *R.L.* of ~-29.6 dB (over 99.9% absorption) at 13.6 GHz with a wide response bandwidth (1.7 GHz). Furthermore, the BTO/CNT 60 wt.% hybrid nanocomposites, t = 1.1 mm showed a minimum *R.L.* of ~-56.5 dB (over 99.999% absorption) at 13.2 GHz and was the best absorber when compared with the other samples of different thickness. The *R.L.* peak decreased from high frequency to lower frequency range and their response bandwidth become wider as the thickness of the sample increased. This proves that the thickness of the samples can be manipulated to produce absorption bands at different frequencies to design highly effective EM wave absorbers.

References

[1] F. Qin, C. Brosseau, J. Appl. Phys. 111 (2012) 061301.

[2] L. Jing, G. Wang, Y. Duan, Y. Jiang, J. Alloys Compd. 475 (2009) 862-868.

[3] X. Chen, G. Wang, Y. Duan, S. Liu, J. Alloys Compd. 453 (2008) 433-436.

[4] H. L. Zhu, Y. J. Bai, R. Liu, N. Lun, Y. X. Qi, F. D. Han, X. L. Meng, J. Q. Bi, R. H. Fan, AIP Adv. 1 (2011) 032140.

[5] G. J. H. Melvin, Q.-Q. Ni, Y. Suzuki, T. Natsuki, J. Mater. Sci. 49 (2014) 5199-5207.

[6] C. Bi, M. Zhu, Q. Zhang, Y. Li, H. Wang, Mater. Chem. Phys. 126 (2011) 596-601.

[7] C. Bi, M. Zhu, Q. Zhang, Y. Li, H. Wang, J. Nanosci. Nanotechnol. 11 (2011) 1030-1036.

[8] X. Huang, Z. Chen, L. Tong, M. Feng, Z. Pu, X. Liu, Mater. Lett. 111 (2013) 24-27.

[9] T. H. Ting, K. H. Wu, J. Polym. Res. 20 (2013) 127.

[10] J. Huo, L. Wang, H. Yu, J. Mater. Sci. 44 (2009) 3917-3927.

[11] Y. F. Zhu, L. Zhang, T. Natsuki, Y. Q. Fu, Q. Q. Ni, ACS Appl. Mater. Interfaces 4 (2012) 2101-2106.

[12] T.H. Ting, Y.N. Jau, R.P. Yu, Appl. Surf. Sci. 258 (2012) 3184-3190.

[13] Y. F. Zhu, Y. Q. Fu, T. Natsuki, Q. Q. Ni, Polym. Compos. 34 (2013) 265-273.

[14] G. Wang, X. Chen, Y. Duan, S. Liu, J. Alloys Compd. 454 (2008) 340-346.

[15] Q. Yuchang, Z. Wancheng, L. Fa, Z. Dongmei, J. Magn. Magn. Mater. 323 (2011) 600-606.

[16] J. Yang, J. Zhang, C. Liang, M. Wang, P. Zhao, M. Liu, J. Liu, R. Che, ACS Appl. Mater. Interfaces 5 (2013) 7146-7151.

[17] W. Jiang, C. Jiang, X. Gong, Z. Zhang, J. Sol-Gel Sci. Technol. 52 (2009) 8-14.

[18] W. Li, Z. Xu, R. Chu, P. Fu, J. Hao, J. Alloys Compd. 482 (2009) 137-140.

[19] R. Kavian, A. Saidi, J. Alloys Compd. 468 (2009) 528-532.

[20] L. Zhang, Y. Hashimoto, T. Taishi, Q. Q. Ni, Appl. Surf. Sci. 257 (2011) 1845-1849.

[21] D. J. Guo, H. L. Li, Carbon 43 (2005) 1259-1264.

[22] G. Gao, D. Guo, C. Wang, H. Li, Electrochem. Commun. 9 (2007) 1582-1586.

[23] E. Chavez, S. Fuentes, R. A. Zarate, L. Padilla-Campos, J. Mol. Struct. 984 (2010) 131-136.

[24] J. Q. Qi, T. Peng, Y. M. Hu, L. Sun, Y. Wang, W. P. Chen, L. T. Li, C. W. Nan, H. L. W. Chan, Nanoscale Res. Lett. 6 (2011) 466.

[25] R.L. Brutchey. D. A. Morse, Angew. Chem. 118 (2006) 6714-6716.

[26] A. Gajovic, J. V. Plestina, K. Zagar, M. Plodenic, S. Sturm, M. Ceh, J. Raman Spectrosc. 44 (2013) 412-420.

[27] S. Santangelo, G. Messina, G. Faggio, M. Lanza, C. Milone, J. Raman Spectrosc.42 (2011) 593-602.

[28] R. A. DiLeo, B. J. Landi, R. P. Raffaelle, J. Appl. Phys. 101 (2007) 064307.

Chapter 3

****

Double-layer BTO/CNT EM wave absorber

****

3 Double-layer BTO/CNT EM wave absorber

3.1 Introduction

It is essential to design electromagnetic (EM) wave absorber to resolve the problem of EM radiation aroused by application of them in communication appliances and electronic tools in scientific, commercial, industrial, and military fields that can harm the health of human beings and pollute the environment [1-11]. An ideal EM wave absorber material should be lightweight, strongly absorb EM waves, possess tunable absorption frequency, and multifunctionality [1-5]. Thus, nanomaterials are among important candidates for EM wave absorber materials [2-4].

In recent years, carbon nanotubes (CNTs) and barium titanate (BTO) have been paid attention as the EM wave absorber materials. High electrical conductivity of the CNTs makes them capable of dissipating electrostatic charges or shielding EM radiation [3, 4, 12, 13]. Meanwhile, BTO perovskite possess high dielectric constant, good ferroelectric properties, and shows occurrence of relaxation at gigahertz frequencies [3, 6, 7, 14-17]. The combination of BTO with CNTs can integrate the properties of these two components to form nanocomposites for use as promising EM wave absorber materials.

However, reports on BTO/CNT materials are still very limited. Bi et al. [6] and Huang et al. [7] fabricated BTO/CNT composites and characterized their single-layer EM wave absorption properties. Even though their results showed high reflection loss (*R.L.*) (<-20 dB, over 99% absorption), it is worth to notice that certain thickness (2 mm or more) are necessary to obtain those *R.L.* values. In order to gain higher *R.L.*, thin, and possess wide response bandwidth materials, double-layer absorber can be considered as an effective method [9, 11, 17]. Yuchang et al. [17] reported double-layer absorber consist of carbonyl iron and BTO. In their reports, the samples with thickness under than 2 mm exhibited high *R.L.* and wide response bandwidth.

In this chapter, we prepared BTO nanoparticles and grafted them onto the surface of CNTs by using sol-gel method. Then, the complex permittivity and permeability of these nanocomposites are measured and their *R.L.* is calculated. Their performance as a double-layer EM wave absorber was also investigated to achieve thin sample with high

absorption ability and wide response bandwidth.

3.2 Materials and methods

3.2.1 Fabrication of BTO/CNT nanocomposites

Multi-walled CNTs (Wako Pure Chemical Industries Ltd., Japan, d = 20-30 nm) were functionalized by mild hydrothermal treatment, as we reported in Refs. [3, 18, 19], with some modifications. BTO nanoparticles were prepared by sol-gel method as reported in Ref. [3], with some modifications, and functionalized CNTs were added to fabricate BTO/CNT nanocomposites. Barium acetate $Ba(CH_3COO)_2$, titanium tetraisopropoxide $Ti[(CH_3)_2CHO]_4$, acetic acid, ethanol, and pure water were obtained from Wako Pure Chemical Industries Ltd., Japan.

$Ba(CH_3COO)_2$ was dissolved in mixed solution of 20 ml ethanol and 3 ml acetic acid (solution A), stirred in water bath at 60 °C for 0.5 h. In the same time, $Ti[(CH_3)_2CHO]_4$ was mixed in 10 ml ethanol (solution B). Solution A and B were combined and 1 ml pure water was added to perform hydrolysis. Then these two solutions were stirred at 60 °C for 2.0 h to form a sol, which contained Ba/Ti molar ratio 1:1. Next 0.15 g functionalized CNTs were added to the final solution, sonicated for 1 h, and stirred furthermore for about 1.5-2 h, 80 °C until gel was formed. The black color gel was then dried at 100 °C for 24 h to make a xerogel. Finally, the product was calcined at 800 °C for 2 h. Samples for BTO were prepared using same process excluding the addition of CNTs.

Samples for the complex permittivity and permeability measurement were prepared by loading the BTO/CNT in polyurethane (PU) with a weight fraction of 30 wt.%. For comparison, the samples of BTO 30 wt.% and CNT 3 wt.% were also fabricated with the same process. The thickness of all of the samples was 1 mm. The samples for this measurement are denoted as BTO/CNT, BTO, and CNT hereafter.

3.2.2 Evaluation method

The crystal structure of prepared nanomaterials was analyzed by using X-ray diffraction (XRD; Rigaku Rotaflex, Japan) with Cu Kα radiation (λ = 0.15406 nm). X-ray photoelectron spectroscopy (XPS; Kratos Axis Ultra DLD) was performed with a standard Mg Kα (1256.6 eV) X-ray source operating at 10 mA and 15 kV to characterize the elemental composition and chemical states of the samples. The

morphology was characterized using transmission electron microscopy (TEM; JEM-2100, JOEL, Japan) and field emission scanning electron microscopy (FE-SEM; Hitachi S-5000, Japan) with an accelerating voltage of 200 kV and 20 kV, respectively.

The complex permittivity and permeability were measured using a vector network analyzer (37247D, Anritsu Co. Ltd.) within the frequency range of 0.5-13.8 GHz. The samples were cut into a toroidal shape with an outer diameter of 7.0 mm, inner diameter of 3.0 mm. The *R.L.* of single- and double-layer was calculated from the measured complex permittivity and permeability of the samples.

3.3 Results and discussion

3.3.1 Structure and morphology of BTO/CNT nanocomposites

XRD patterns of the CNTs and BTO/CNT are shown in Fig. 3.1(a). All peaks of the BTO/CNT can be assigned to the cubic perovskite structure (JCPDS No. 31-0174) [3, 7, 14, 15]. Strong intensity of (110) peak can be observed from BTO/CNT at $2\theta = 31.8°$. The CNTs showed typical multi-walled CNTs (002) broad peak at 22° [3, 20] which overlapped with the (100) peak of BTO/CNT. Even though the peak for CNTs in the BTO/CNT was overlapped, their existence was confirmed from the XPS spectra. Using the Scherrer's equation as shown below [3, 16],

$$D = \frac{0.9\lambda}{\beta \cos\theta} \tag{3.1}$$

where D is the particle size, λ is the wavelength of the Cu Kα radiation (0.15406 nm), θ is the diffraction angle, and β is the full width at half maximum of the peak, average crystalline size of BTO nanoparticles were calculated to be 14.2 nm from the broadening of BTO/CNT (110) peak.

XPS evaluation was carried out to determine the elemental composition of the BTO/CNT, as shown in Fig. 3.1(b). The XPS survey spectrum of the BTO/CNT confirmed the presence of carbon (C 1s), oxygen (O 1s), barium (Ba 3d, Ba 4d, Ba 4p, Ba 4s), and titanium (Ti 2p). The presence of Ba 3d, Ti 2p, and O 1s peaks proves the formation of BTO nanoparticles. The atomic percentage ratios for the BTO/CNT are 56.83% for C 1s, 6.36% for Ba 3d, 6.53% for Ti 2p, and 30.28% for O 1s. The atomic percentage ratio of Ba 3d and Ti 2p is about 1:1, similar to the molar ratio of Ba/Ti in

the fabrication process.

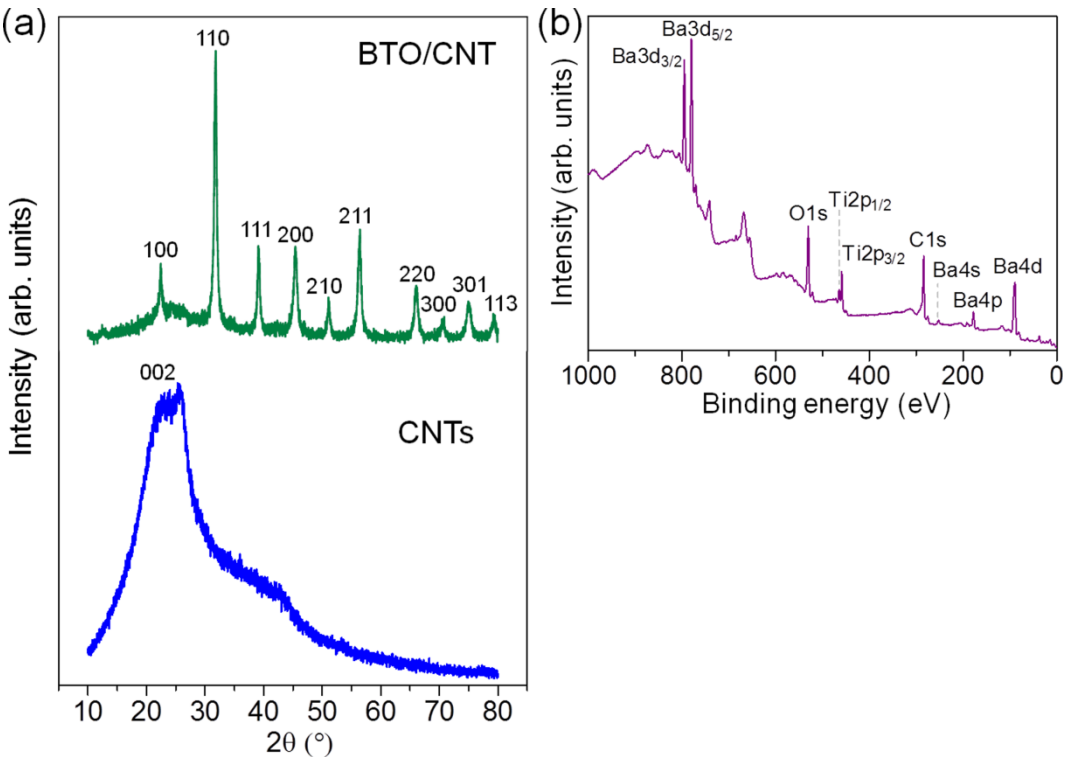

Fig. 3.1 (a) XRD patterns of the CNTs and BTO/CNT and (b) XPS spectra of the BTO/CNT.

TEM images of the CNTs, BTO, and BTO/CNT are depicted in Fig. 3.2. Fig. 3.2(a) shows the TEM image of CNTs and no agglomeration was observed. Fig. 3.2(b) shows the TEM image of BTO nanoparticles with spherical shape which exist in a bundle. Fig. 3.2(c) and (d) show the TEM images of BTO/CNT where BTO nanoparticles were grafted onto the surface of CNTs. The shape of BTO nanoparticles was also spherical and they were strongly adhered to the surfaces of CNTs. From Fig. 3.2(d), the diameter of BTO nanoparticles was under 15 nm, and this shows high similarity with the calculation using Scherrer's equation (14.2 nm). Fig. 3.2(d) also further reveals that the BTO nanoparticle form a single crystal with crystal spacing ~0.28 nm corresponds to (110) crystal plane [3, 14, 21]. FE-SEM images of the CNTs, BTO, and BTO/CNT incorporated in PU are illustrated in Fig. 3.3. All of the fillers showed good dispersion in the PU matrix. Fig. 3.3(c) shows the FE-SEM image of BTO/CNT nanocomposites where BTO nanoparticles were grafted onto the surface of CNTs was also observed.

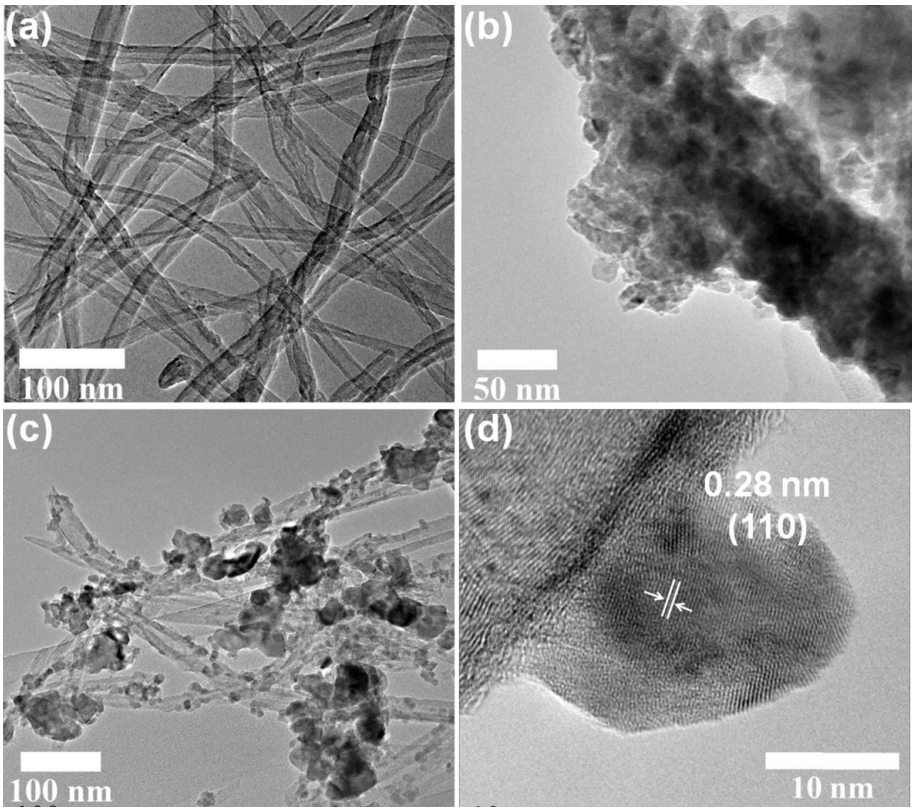

Fig. 3.2 TEM images of (a) CNTs, (b) BTO, (c) BTO/CNT, and (d) high magnification TEM image of BTO/CNT.

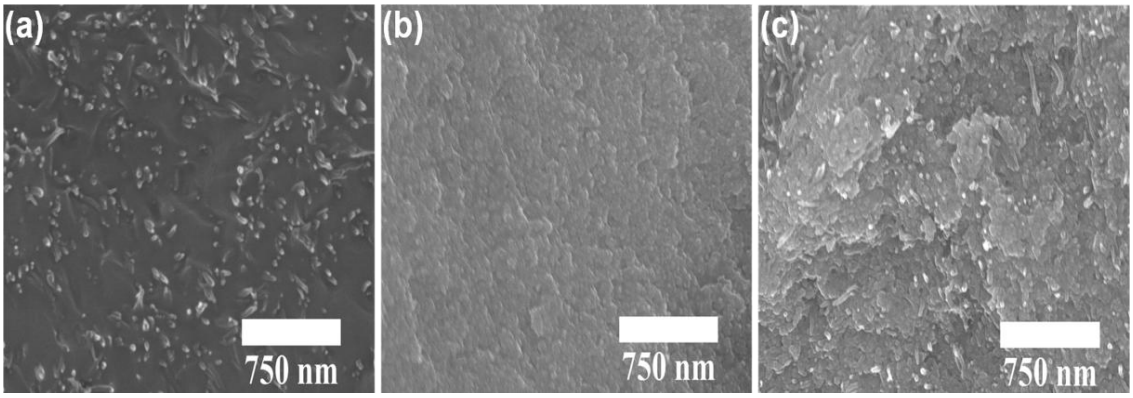

Fig. 3.3 FE-SEM cross-sectional images of (a) CNT 3 wt.%, (b) BTO 30 wt.%, and (c) BTO/CNT 30 wt.% nanocomposites.

3.3.2 Electromagnetic wave absorption properties

The real parts of permittivity (ε') and permeability (μ') represent the storage of electric and magnetic energies, respectively, while the imaginary (ε'', μ'') parts symbolize the loss and dissipation of both energies [1-4]. The complex permittivity and permeability of the CNT (3 wt.%), BTO (30 wt.%), and BTO/CNT (30 wt.%)

nanocomposites loaded in PU with thickness, t = 1.0 mm in the range of 0.5-13.8 GHz are presented in Fig. 3.4(a) and (b), respectively. When the frequency increased, the complex permittivity decreased because the polarizabilities (electronic, ionic, and orientation) and electric displacement are not maintained in a changing EM field [3, 4, 14-16]. Relatively high ε'' of the BTO/CNT indicates that this sample can cause dielectric loss, dominated primarily by dielectric polarization, spontaneous polarization, and associated relaxation phenomena [3, 14, 16, 17]. Moreover, with the insertion of CNTs into BTO/CNT nanocomposites, the high electrical conductivity of the CNTs enables strong polarization to occur, dissipation of electrostatic charges, Ohmic losses, or multiple scattering caused by the large specific area, which lead to enhanced complex permittivity [1, 3, 4, 12]. Interestingly, the presence of BTO nanoparticles affected the complex permeability. As the frequency increased, the complex permeability of BTO/CNT increased and was higher than that of other samples until a certain frequency, after which it gradually decreased. This can be attributed to natural resonance or eddy current loss [2, 3]. When conducting material (CNTs) was put in an alternating magnetic field, a close induced current will be produced inside the material, which would dissipate the energy and referred as eddy current loss [2, 3]. CNTs possess high electrical conductivity and this leads to permeability decreasing rapidly at high frequency caused by the eddy current loss [3, 4, 6].

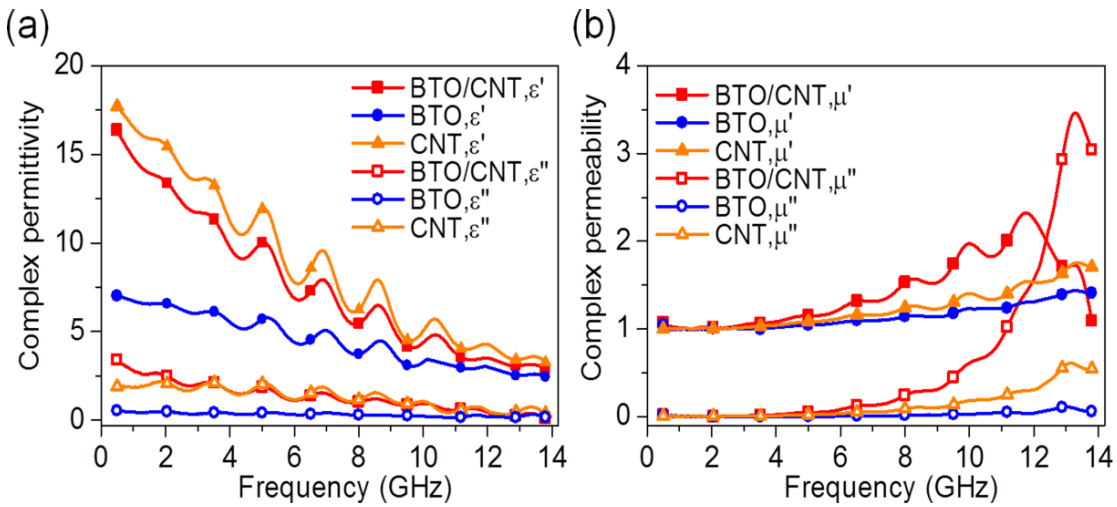

Fig. 3.4 (a) Complex permittivity and (b) complex permeability of the BTO/CNT, BTO, CNT nanocomposites (t = 1.0 mm).

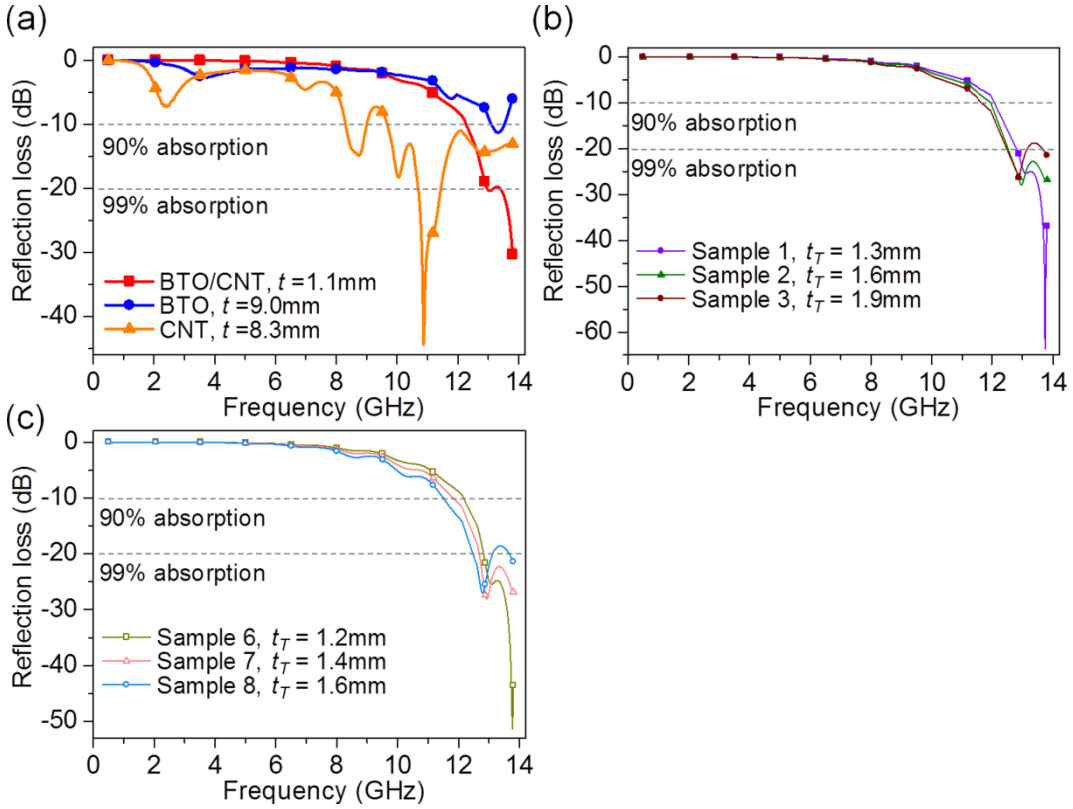

Fig. 3.5 Reflection loss of (a) single-layer absorber, (b) and (c) double-layer absorber with various thicknesses.

To investigate the EM wave absorption properties of the samples, the *R.L.* was calculated according to the transmission line theory as follows:

$$R.L. = 20 \log \left| \frac{Z_{in} - 1}{Z_{in} + 1} \right| \tag{3.2}$$

where the normalized input impedance (Z_{in}) is given by the formula,

$$Z_{in} = \sqrt{\frac{\mu_r}{\varepsilon_r}} \tanh \left[j \left(\frac{2\pi f d}{c} \right) \sqrt{\mu_r \varepsilon_r} \right] \tag{3.3}$$

where $\varepsilon_r = \varepsilon' - j\varepsilon''$, $\mu_r = \mu' - j\mu''$, f is the EM wave frequency (Hz), d is the thickness of the absorber (m), and c is the velocity of light in free space (m/s). *R.L.* of the single-layer samples with matching thickness which exhibited optimum minimum *R.L.*

is shown in Fig. 3.5(a).

The BTO nanocomposites showed a minimum *R.L.* of ~-11.3 dB at 13.3 GHz with t = 9.0 mm and their response bandwidth (*R.L.* of less than -10 dB, over 90% absorption) was 0.4 GHz (13.1–13.5 GHz). Conversely, the CNT nanocomposites with t = 8.3 mm exhibited a minimum *R.L.* of ~-44.4 dB (over 99.99% absorption) at 10.9 GHz with a response bandwidth of 0.7 GHz (8.3-9.0 GHz) and 4.1 GHz (9.7-13.8 GHz). The BTO/CNT nanocomposites with t = 1.1 mm showed a minimum *R.L.* of ~-30.3 dB (over 99.9% absorption) at 13.8 GHz with a response bandwidth of 1.5 GHz (12.3-13.8 GHz). Thick samples are necessary to obtain high *R.L.* for the BTO and CNT samples. However, the BTO/CNT nanocomposites demonstrated relatively high *R.L.* with relatively low thickness (1.1 mm) and was the best single-layer absorber considering their *R.L.* and thickness. Although this proved that single-layer BTO/CNT nanocomposites are sufficient as an excellent thin absorber, their response bandwidth is considered narrow. To improve their response bandwidth and to achieve higher *R.L.*, double-layer absorber is desirable and will be discussed in the next section. When the BTO nanoparticles were grafted onto the surface of CNTs, enhanced *R.L.* were obtained compared to the BTO sample. The BTO/CNT showed similar pattern of EM wave absorption with the BTO but improved in *R.L.*, which indicated that CNTs contributed to the developed absorption ability of the nanocomposites. There are many boundaries in the BTO/CNT, including between the BTO surfaces and CNTs surfaces. The behavior of the EM wave absorption of the BTO/CNT can be attributed to the multiple interfacial polarizations between the BTO nanoparticles and CNTs. Furthermore, the large specific areas of the surfaces of the nanocomposites triggered higher interfacial polarization, multiple scattering, and molecular polarization which leads to a high minimum *R.L.* [1, 3, 4, 6, 12, 14]. Furthermore, suitable complex permittivity and complex permeability are essential to promote EM wave absorption [1-4]. This also can be related to another important parameter connected to *R.L.*, *i.e.*, the concept of matched impedance. This concept suggests that the characteristic impedance of an absorber should be almost equal to that of the free space to achieve zero reflection on the front surface of the material [3, 4, 15, 17]. Obviously, to design an optimized absorber with a high minimum *R.L.*, appropriate EM impedance matching is important.

3.3.3 Double-layer electromagnetic wave absorber

Double-layer EM wave absorber can be manipulated to produce high *R.L.*, thin, and wide response bandwidth materials. The Z_{in} for double-layer is given by the formula,

$$Z_{in} = \frac{\sqrt{\frac{\mu_2}{\varepsilon_2}}\left(\sqrt{\frac{\mu_1}{\varepsilon_1}}\tanh\left[j\left(\frac{2\pi f d_1}{c}\right)\sqrt{\mu_1\varepsilon_1}\right] + \sqrt{\frac{\mu_2}{\varepsilon_2}}\tanh\left[j\left(\frac{2\pi f d_2}{c}\right)\sqrt{\mu_2\varepsilon_2}\right]\right)}{\sqrt{\frac{\mu_2}{\varepsilon_2}} + \sqrt{\frac{\mu_1}{\varepsilon_1}}\tanh\left[j\left(\frac{2\pi f d_1}{c}\right)\sqrt{\mu_1\varepsilon_1}\right]\tanh\left[j\left(\frac{2\pi f d_2}{c}\right)\sqrt{\mu_2\varepsilon_2}\right]} \quad (3.4)$$

where ε_1, ε_2, μ_1, μ_2 are the complex permittivity and permeability of Layer 1 and 2, respectively. d_1 and d_2 are the thickness of Layer 1 and 2, respectively. f and c are similar with Eq. (3.3). Layer 1 is the absorption layer and Layer 2 is the matching layer [9]. The details of double-layer samples and their properties are presented in Table 3.1. *R.L.* of the double-layer samples with various thicknesses was calculated by substituting Eq. (3.4) into Eq. (3.2) and the results are shown in Fig. 3.5(b), (c), and Table 3.1.

From Fig. 3.5(b), (c), and Table 3.1, the results showed that high *R.L*, thin (under 2 mm), and wide response bandwidth can be obtained for double-layer samples than that of single-layer samples. Sample 1, where the absorption layer is BTO/CNT and matching layer is BTO, with total thickness, t_T = 1.3 mm showed the highest minimum *R.L.* of ~-63.7 dB (over 99.9999% absorption) and was the best absorber when compared with the other samples. Sample 6, where the absorption layer is BTO/CNT and matching layer is CNT, with t_T = 1.2 mm also showed relatively high minimum *R.L.* of ~-51.3 dB (over 99.999% absorption). Our nanocomposites showed superior *R.L.* in contrast to other double-layer absorbers reported in Refs. [8-10,17], although the preparation process, type of fillers, and experimental conditions are varied.

Furthermore, the response bandwidth of Sample 1-10 (> 1.5 GHz) was improved in contrast to BTO (0.4 GHz) and BTO/CNT (1.5 GHz) single-layer absorber. Although the minimum *R.L.* of Sample 1-3 and 6-8 decreased as the t_T increased, wider response bandwidth can be obtained. Moreover, the *R.L.* peak also shifted to the lower frequency as the t_T increased. These results show that the frequency related to the minimum *R.L.* (highest absorption) and response bandwidth of the double-layer absorber can be controlled by changing the thickness of the samples. Sample 4 (~-51.3 dB) and Sample 9 (~-44.9 dB) show that relatively high *R.L.* and wide response bandwidth, 2.0 and 2.4

GHz, respectively, also can be achieved by manipulating the thickness of Layer 1 and 2. Sample 1 and Sample 5 show the optimum *R.L.* of double-layer absorber where BTO/CNT are the absorption layer and matching layer, respectively. When using BTO/CNT as the absorption layer, minimum *R.L.* was higher. Similar results also can be observed for Sample 6 and Sample 10. For the double-layer absorber, the matching layer with excellent transmission capacity firstly achieved an excellent impedance matching, and then the absorption layer could achieve a favorable absorption capacity [9]. Overall, we believe that the BTO/CNT nanocomposites are a promising EM wave absorber, because their absorption and response bandwidth can be modulated simply by manipulating the sample thickness of double-layer absorber to satisfy applications in different frequency bands.

Table 3.1 Details of double-layer absorber and their properties.

Sample	Material	Thickness (mm)	Total thickness (mm)	Minimum *R.L.* (dB)	*R.L.* peak (GHz)	Bandwidth *R.L.* < -10 dB(GHz)
1	Layer1: BTO/CNT	1.0	1.3	-63.7	13.7	12.1-13.8
	Layer2: BTO	0.3				(1.7)
2	Layer1: BTO/CNT	1.0	1.6	-27.9	13.0	12.0-13.8
	Layer2: BTO	0.6				(1.8)
3	Layer1: BTO/CNT	1.0	1.9	-26.2	12.9	11.7-13.8
	Layer2: BTO	0.9				(2.1)
4	Layer1: BTO/CNT	0.8	2.0	-51.3	13.0	11.8-13.8
	Layer2: BTO	1.2				(2.0)
5	Layer1: BTO	0.1	1.1	-25.5	13.8	12.1-13.8
	Layer2: BTO/CNT	1.1				(1.7)
6	Layer1: BTO/CNT	1.0	1.2	-51.3	13.8	12.1-13.8
	Layer2: CNT	0.2				(1.7)
7	Layer1: BTO/CNT	1.0	1.4	-28.1	12.9	11.8-13.8
	Layer2: CNT	0.4				(2.0)
8	Layer1: BTO/CNT	1.0	1.6	-27.0	12.8	11.5-13.8
	Layer2: CNT	0.6				(2.3)
9	Layer1: BTO/CNT	0.7	1.8	-44.9	12.9	11.4-13.8
	Layer2: CNT	1.1				(2.4)
10	Layer1: CNT	0.1	1.1	-25.6	13.8	12.3-13.8
	Layer2: BTO/CNT	1.0				(1.5)

3.4 Conclusions

BTO nanoparticles were grafted onto the surface of CNTs and then loaded into PU to fabricate BTO/CNT nanocomposites. The high interfacial area of the nanomaterials results in high interfacial polarization and multiple scattering, which improves EM wave absorption. The single-layer BTO/CNT nanocomposites (t = 1.1 mm) exhibited a minimum *R.L.* of ~-30.3 dB (over 99.9% absorption) at 13.8 GHz with a response bandwidth of 1.5 GHz. The double-layer absorber showed that they can be manipulated

to produce high *R.L.*, thin, and wide response bandwidth materials. Furthermore, the double-layer absorber where the absorption layer is BTO/CNT and matching layer is BTO, t_T = 1.3 mm showed the highest minimum *R.L.* of ~-63.7 dB (over 99.9999% absorption) and was the best absorber when compared with the other samples. The *R.L.* peak decreased from high frequency to lower frequency range and their response bandwidth become wider as the thickness of the double-layer absorber increased. This proves that the thickness of the samples can be manipulated to produce absorption bands at different frequencies to design highly effective EM wave absorbers.

References

[1] F. Qin, C. Brosseau, J. Appl. Phys. 111 (2012) 061301.

[2] J. Huo, L. Wang, H. Yu, J. Mater. Sci. 44 (2009) 3917-3927.

[3] G. J. H. Melvin, Q. Q. Ni, T. Natsuki, J. Alloys Compd. 615 (2014) 84-90.

[4] G. J. H. Melvin, Q.-Q. Ni, Y. Suzuki, T. Natsuki, J. Mater. Sci. 49 (2014) 5199-5207.

[5] D. Micheli, C. Apollo, R. Pastore, M. Marchetti, Compos. Sci. Technol. 70 (2010) 400-409.

[6] C. Bi, M. Zhu, Q. Zhang, Y. Li, H. Wang, J. Nanosci. Nanotechnol. 11 (2011) 1030-1036.

[7] X. Huang, Z. Chen, L. Tong, M. Feng, Z. Pu, X. Liu, Mater. Lett. 111 (2013) 24-27.

[8] Q. Liu, B. Cao, C. Feng, W. Zhang, S. Zhu, D. Zhang, Compos. Sci. Technol. 72 (2012) 1632-1636.

[9] H. Wu, L. Wang, S. Guo, Z. Shen, Appl. Phys. A 108 (2012) 439-446.

[10] Y. Liu, X. Liu, X. Wang, J. Alloys Compd. 584 (2014) 249-253.

[11] C. Wei, X. Shen, F. Song, Y. Zhu, Y. Wang, Mater. Des. 35 (2012) 363-368.

[12] T.H. Ting, Y.N. Jau, R.P. Yu, Appl. Surf. Sci. 258 (2012) 3184-3190.

[13] Y. Qing, W. Zhou, S. Huang, Z. Huang, F. Luo, D. Zhu, Compos. Sci. Technol. 89 (2013) 10-14.

[14] Y. F. Zhu, L. Zhang, T. Natsuki, Y. Q. Fu, Q. Q. Ni, ACS Appl. Mater. Interfaces 4 (2012) 2101-2106.

[15] Y. F. Zhu, Y. Q. Fu, T. Natsuki, Q. Q. Ni, Polym. Compos. 34 (2013) 265-273.

[16] G. Wang, X. Chen, Y. Duan, S. Liu, J. Alloys Compd. 454 (2008) 340-346.

[17] Q. Yuchang, Z. Wancheng, L. Fa, Z. Dongmei, J. Magn. Magn. Mater. 323 (2011) 600-606.

[18] G. J. H. Melvin, Q. Q. Ni, T. Natsuki, Appl. Phys. A 117 (2014) 2043-2050.

[19] L. Zhang, Y. Hashimoto, T. Taishi, Q. Q. Ni, Appl. Surf. Sci. 257 (2011) 1845-1849.

[20] D. J. Guo, H. L. Li, Carbon 43 (2005) 1259-1264.

[21] J. Q. Qi, T. Peng, Y. M. Hu, L. Sun, Y. Wang, W. P. Chen, L. T. Li, C. W. Nan, H. L. W. Chan, Nanoscale Res. Lett. 6 (2011) 466.

Chapter 4

****

Ag/CNT hybrid nanocomposites EM wave absorber

****

4 Ag/CNT hybrid nanocomposites EM wave absorber

4.1 Introduction

The advancement of electronic devices and communication instruments in commercial, industrial, scientific, and military fields, such as mobile phones, computers, radar technology, and wireless network systems is progressing rapidly [1-4]. Although these technologies are convenient, electromagnetic (EM) radiation has restricted their development and is becoming a serious problem. EM radiation can pollute the environment and harm the health of human beings, especially expectant mothers and children [1-4]. Therefore, it is essential to protect electronic devices and human beings from excessive exposure to EM radiation. EM wave absorbing materials have received much attention to effectively solve the problem of exposure to EM radiation. An ideal EM wave absorber should be lightweight, strongly absorb EM waves, and possess tunable absorption frequency, and multifunctionality [1, 2].

Nanomaterials such as nanoparticles and nanocomposites are among important candidates as EM wave absorbing materials [5]. The relative density of nanomaterials is lower and their specific surface area is larger than those of the corresponding bulk materials. As a result, there are a large number of active atoms at the nanomaterial surface, which has a large interfacial dielectric loss induced by interface polarization [1]. Metal nanoparticles such as silver (Ag) nanoparticles hybridized with carbon nanotubes (CNTs) have potential to be developed as advanced materials for a wide range of applications [6-11], including as EM wave absorbing materials [12, 13]. CNTs are light, possess a high aspect ratio and unique magnetic properties, and exhibit favorable mechanical, chemical, and electric properties that have attracted considerable attention [2, 7-9, 13-16]. Their high electrical conductivity makes CNTs capable of dissipating electrostatic charges or shielding EM radiation [16]. However, CNTs disperse poorly in organic and aqueous solvents because of a strong intrinsic van der Waals attraction [11, 17]. Many techniques have been used to solve the problem by functionalizing the CNTs using acid treatment [12, 13, 18], mild hydrothermal treatment [17], microwave-induced radical polymerization [19], and so on. In this study, we used acid treatment method to

functionalize the CNTs. This treatment is fast, easy, and leads to the introduction of carboxyl and hydroxyl groups to the surface of the CNTs, which allows them to be highly dispersed in polar solvents. Furthermore, Ag is a good conductor, abundant, easy to prepare, and inexpensive [9-11]. Ag nanoparticles decoration would have a beneficial effect on the electrical conductivity of CNTs because the inherent electrical conductivity of Ag is superior to the CNTs without Ag [9]. Metal nanoparticles such as Ag nanoparticles, produced large electric or magnetic loss and have been demonstrated to show promising EM wave absorption [1, 4]. Furthermore, metal nanoparticles such as Ag nanoparticles decorated on the CNTs will absorb the EM wave energy through electrons hopping and shows enhanced EM wave absorption bandwidth [2]. The combination of Ag nanoparticles with CNTs can integrate the properties of these two components to form hybrid nanocomposites for use as EM wave absorbing materials.

Reports on Ag nanoparticles or Ag/CNT hybrid materials as EM wave absorbers are very limited. Ramesh et al. [4] investigated the EM wave absorbing properties of Ag nanoparticles embedded in thin polymer films. Meanwhile, Zhao et al. [12, 13] investigated the EM wave absorbing properties of CNTs filled with Ag nanowires. To the best of our knowledge, the EM wave absorbing properties of Ag/CNT hybrid nanocomposites where Ag nanoparticles are decorated on the surface of CNTs have not been examined.

In this chapter, we prepare Ag nanoparticles and graft them onto the surface of CNTs. We then evaluate the ability of these materials to absorb EM waves by measuring their dielectric and/or magnetic losses when penetrated by an EM wave [1, 16]. The complex permittivity and complex permeability of these hybrid nanocomposites are measured, and their reflection loss is also evaluated.

4.2 Materials and methods

4.2.1 Modification of CNTs

CNTs can be modified with a single or mixture of acids [12, 13, 18]. Multi-walled CNTs (Wako Pure Chemical Industries Ltd., Japan, d = 40-70 nm) were functionalized by chemical oxidation in nitric acid (HNO_3). The CNTs were heated under reflux in boiling HNO_3 at 120°C for 10 h. The resulting mixture was centrifuged with pure water, diluted with pure water and left overnight until the pH was neutral. The CNTs were centrifuged again with pure water to separate them and then dried overnight at 60°C.

The acid-treated CNTs are denoted as modified CNTs hereafter. The samples for pristine CNTs were prepared by using obtained CNTs without any further modification.

4.2.2 Preparation of Ag nanoparticles

Ag nanoparticles can be produced by chemical reduction, which only requires simple equipment, is convenient, inexpensive and gives a high yield [18, 20, 21]. The preparation is based on Refs. [20, 21], where method in Ref. [20] was done by one of our research group. This method has advantages including: short reaction time; small and relatively uniform particles can be fabricated; the reaction proceeds rapidly at room temperature; high purity and good conductivity. Silver nitrate ($AgNO_3$), sodium citrate (Na_3Ct), and 2-dimethylaminoethanol (DMAE) were obtained from Wako Pure Chemical Industries Ltd., Japan. Polyvinylpyrrolidone (PVP, K 15, Tokyo Chemical Industry Co. Ltd., Japan) was used to prevent aggregation of the Ag nanoparticles.

PVP (1.0 g) was stirred in pure water (20 ml) for 10 min. $AgNO_3$ (0.5 g) was added and the mixture was stirred vigorously for 10 min. Na_3Ct (0.88 g) diluted in pure water (20 ml) was added dropwise to the stirred mixture. Then, DMAE (0.03 g) was added and the mixture was stirred for 1 h. Finally, the mixture was centrifuged, washed with pure water, and dispersed in ethanol (10 ml). The Ag nanoparticles dispersed in ethanol (solution A) were used to prepare Ag/CNT hybrid nanocomposites.

4.2.3 Preparation of Ag/CNT hybrid nanocomposites

Ag nanoparticles were grafted onto the surface of the CNTs according to the method reported in Ref. [18] with some modification. Cysteamine hydrochloride and 2,5-dihydroxybenzoic acid (DHB) obtained from Wako Pure Chemical Industries Ltd., Japan were used to link the Ag nanoparticles to the surface of the CNTs.

Ag nanoparticles in ethanol (5 ml, obtained from solution A) were sonicated for 10 min and then reacted with cysteamine hydrochloride (0.23 g) in ethanol (95 ml) at 80°C for 6 h in an oil bath (mixture A). The total volume of mixture A was 100 ml. At the same time, modified CNTs (0.05 g) were sonicated in ethanol (100 ml) for 1 h (mixture B). DHB (0.08 g) was added to mixture B, which was then sonicated for 30 min. Mixture A and B were combined and then stirred for 24 h. The resulting product was centrifuged, washed with pure water, and then dried overnight at 60°C.

4.2.4 Evaluation method

Transmission electron microscopy (TEM) images of the Ag nanoparticles, modified CNTs, and Ag/CNT hybrid nanomaterials were obtained using a TEM (JEM-2100, JOEL, Japan) with an accelerating voltage of 200 kV. X-ray photoelectron spectroscopy (XPS, Kratos Axis Ultra DLD) was performed with a standard Mg Kα (1256.6 eV) X-ray source operating at 10 mA and 15 kV to characterize the elemental composition and chemical states of the samples. Raman spectroscopy measurements were performed on a Raman spectrometer (HoloLab series 5000, Kaiser Optical Systems) with 532 nm laser excitation.

The real and imaginary parts of complex permittivity ε ($\varepsilon = \varepsilon' - j\varepsilon''$) and permeability μ ($\mu = \mu' - j\mu''$) were measured by scattering parameters measurement method in reflection mode using a vector network analyzer (37247D, Anritsu Co. Ltd.) within the frequency range of 0.5-14.0 GHz. Samples for these measurements were prepared by loading the Ag/CNT hybrid nanocomposites in paraffin wax with a weight percentage of Ag/CNT hybrid nanocomposite to paraffin of 30%. The complex permittivity and permeability of the paraffin wax are low and constant throughout the frequency range [12]. Furthermore, the paraffin wax shows almost no absorption. The powder-wax composites were pressed into a toroidal shape using a mold designed with an outer diameter of 7.0 mm, inner diameter of 3.0 mm, and thickness of 1.0 mm. The reflection loss was calculated from the measured complex permittivity and permeability of the samples.

4.3 Results and discussion

4.3.1 Morphology of Ag/CNT hybrid nanocomposites

TEM images of the Ag nanoparticles, modified CNTs and Ag/CNT hybrid nanocomposites are depicted in Fig. 4.1. Fig. 4.1(a) and (b) show that the Ag nanoparticles had diameters of less than 10 nm, ranging from 5 to 10 nm. Fig. 4.1(c) shows the modified CNTs before Ag nanoparticles were grafted on their surfaces. The diameter of the CNTs was about 40 nm, and they contained some defects on their walls after modification by acid treatment. Fig. 4.1(d)-(f) show TEM images of the Ag/CNT hybrid nanocomposites with Ag nanoparticles grafted onto the surface of the CNTs. Ag nanoparticles were homogeneously dispersed with no agglomeration and strongly adhered to the surfaces of the CNTs. The diameter of the Ag nanoparticles grafted onto

the surface of the CNTs was also less than 10 nm.

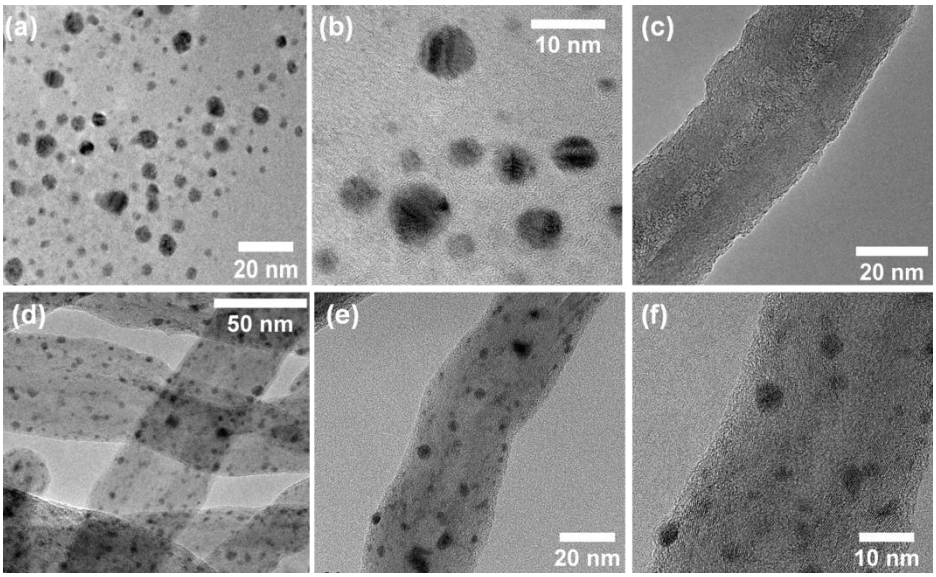

Fig. 4.1 TEM images of (a), (b) Ag nanoparticles; (c) modified CNTs; (d), (e), and (f) Ag/CNT hybrid nanocomposites.

4.3.2 XPS analysis of Ag/CNT hybrid nanocomposites

XPS evaluation was carried out to determine the elemental composition and functional groups of the pristine CNTs, modified CNTs, and Ag/CNT hybrid nanocomposites, as shown in Fig. 4.2. The pristine and modified CNTs exhibited a strong carbon (C 1s) peak at 284 eV and oxygen (O 1s) peak at 532 eV. The modified CNTs clearly showed an O 1s peak with higher intensity than that of the pristine CNTs. The atomic percentage ratios for the pristine CNTs are 98.59% for C 1s and 1.41% for O 1s, while those of the modified CNTs are 92.40 % for C 1s and 7.60 % for O 1s. The higher intensity of the O 1s peak confirms that many oxygen functional groups (carboxyl and hydroxyl) were introduced onto the surface of the CNTs modified by acid treatment.

The XPS survey spectrum of the Ag/CNT hybrid nanomaterial confirmed the presence of C 1s, O 1s, nitrogen (N 1s), chlorine (Cl $2p_{3/2}$), silver (Ag 3d, Ag 3p), and sulfur (S 2s, S 2p). The Ag/CNT samples showed a strong C 1s peak at 284 eV, O 1s peak at 531 eV, N 1s peak at 400 eV, and Cl $2p_{3/2}$ peak at 198 eV. Ag 3d peaks from Ag $3d_{5/2}$ and Ag $3d_{3/2}$ appeared at 368 and 374 eV, respectively. Ag 3p peaks from Ag $3p_{3/2}$ and Ag $3p_{1/2}$ were observed at 573 and 604 eV, respectively. The S 2s and S 2p peaks appeared at 227 and 163 eV, respectively. The presence of Ag 3d and Ag 3p peaks

proves the formation of Ag nanoparticles. Furthermore, the observation of N 1s, Cl $2p_{3/2}$, S 2s, S 2p, Ag 3d, and Ag 3p peaks confirmed that the amidation reaction between cysteamine hydrochloride ($NH_2(CH_2)_2SH$·HCl) and Ag nanoparticles was successful [18]. The CNTs were oxidized using acid treatment in order to introduce carboxyl and hydroxyl groups onto the surface of CNTs. Ag nanoparticles were modified with self-assembled monolayers cysteamine hydrochloride, resulting in cysteamine hydrochloride-Ag groups. Using DHB as a coupling agent, the modified CNTs functionalized with carboxyl and hydroxyl groups on the surface reacted with the amino groups on the silver surface through amide bonds [18]. The Ag 3d doublet peaks with separation energy of 6 eV shown in Fig. 4.3 are consistent with Ag metal, further confirming that Ag on the surface of the CNTs exists in the zero-valent state [7, 8, 18]. The atomic percentage ratios for the Ag/CNT nanomaterials are 87.02% for C 1s, 7.04% for O 1s, 2.73% for Ag 3d, and 3.22% for Ag 3p.

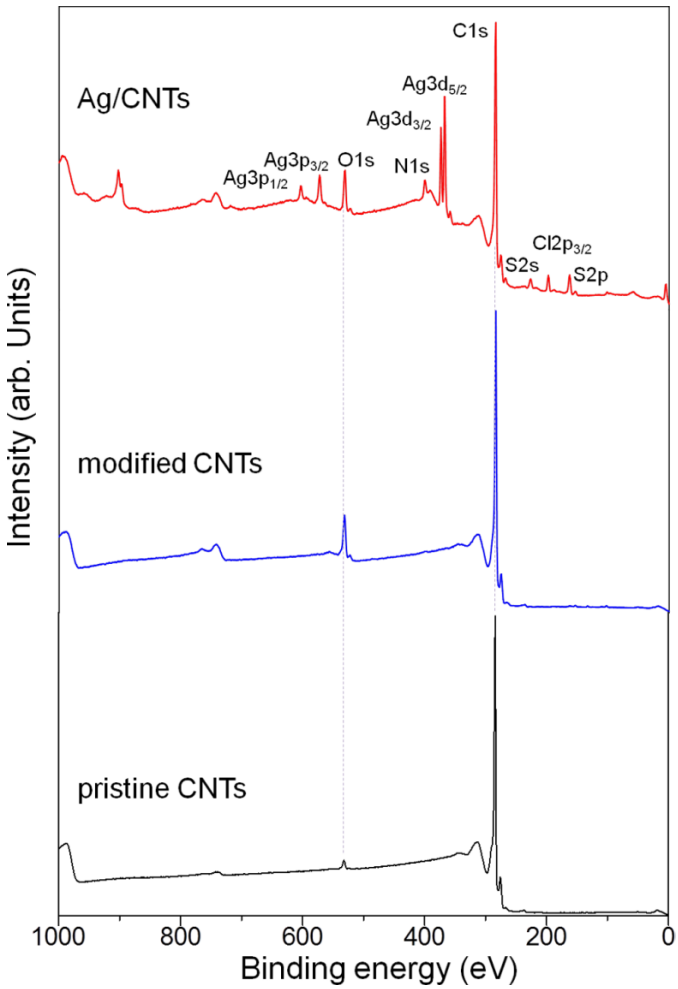

Fig. 4.2 XPS spectra of pristine CNTs, modified CNTs, and Ag/CNT hybrid nanocomposites.

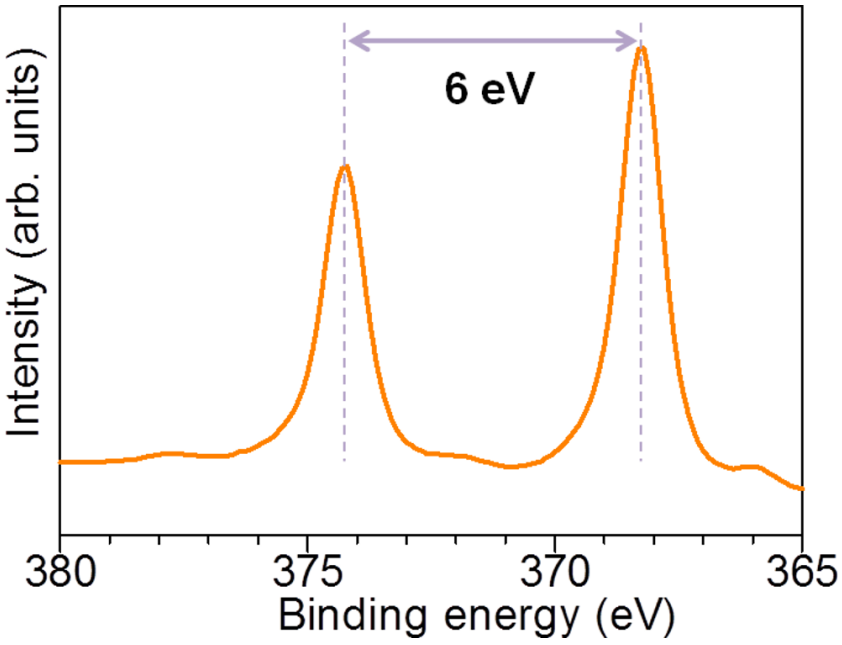

Fig. 4.3 XPS of the Ag 3d core level of the Ag/CNT hybrid nanocomposites.

4.3.3 Raman spectroscopy of Ag/CNT hybrid nanocomposites

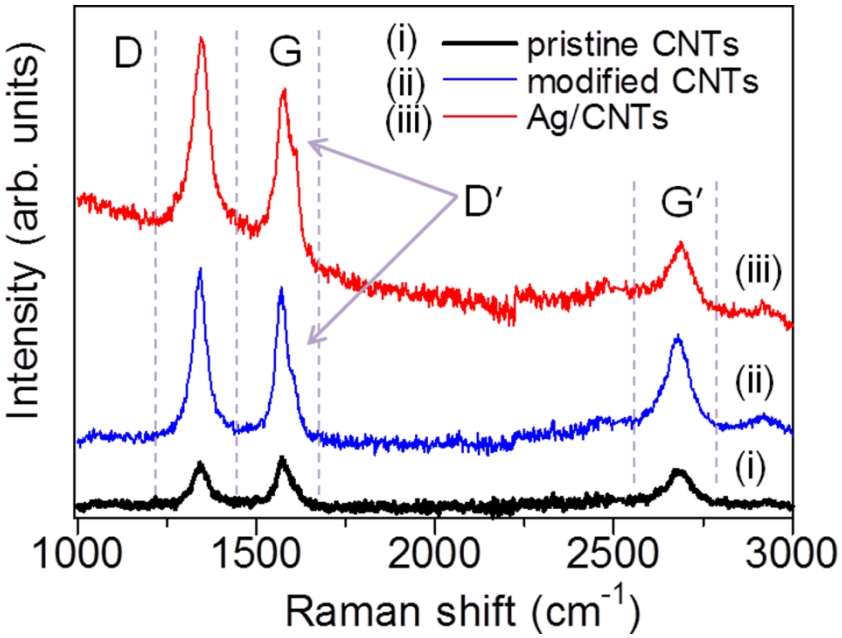

Fig. 4.4 Raman spectra of pristine CNTs, modified CNTs, and Ag/CNT hybrid nanocomposites.

Raman spectroscopy is an effective tool to characterize carbon-based materials [17, 19, 22-24], so Raman spectra of the pristine CNTs, modified CNTs, and Ag/CNT hybrid nanocomposites were measured. The characteristic bands of CNTs, D band (defect) at

~1350 cm^{-1}, G band (graphite band) at ~1580 cm^{-1}, and G′ band (D overtone) at ~2700 cm^{-1} were observed, as illustrated in Fig. 4.4. The D′ band of the modified CNTs and Ag/CNT hybrid nanocomposites ranging from 1600 to 1620 cm^{-1}, which is attributed to structural defects and broadened caused by modification with Ag [24], was also observed. For the Ag/CNT hybrid nanocomposites, the G′ peak shifted to higher wavenumber, ~2688 cm^{-1} (pristine CNTs: ~2679 cm^{-1}, modified CNTs: ~2680 cm^{-1}), because of a substantial charge transfer interaction between the Ag nanoparticles and CNTs [24].

The relative intensity of the D and G bands (I_D/I_G) is related to the amount of structural defects and sp^3-hybridized carbon atoms in a CNT sample, and thus provides direct information about the degree of sidewall functionalization [19, 22]. Furthermore, the relative intensity of the G′ and G bands ($I_{G'}/I_G$) and the relative intensity of the G′ and D bands ($I_{G'}/I_D$), which are related to the scale on which the graphitic order extends and the degree of crystallinity [22], respectively, were also evaluated. The relative intensities of the D/G, G′/G, and G′/D ratios are presented in Fig. 4.5.

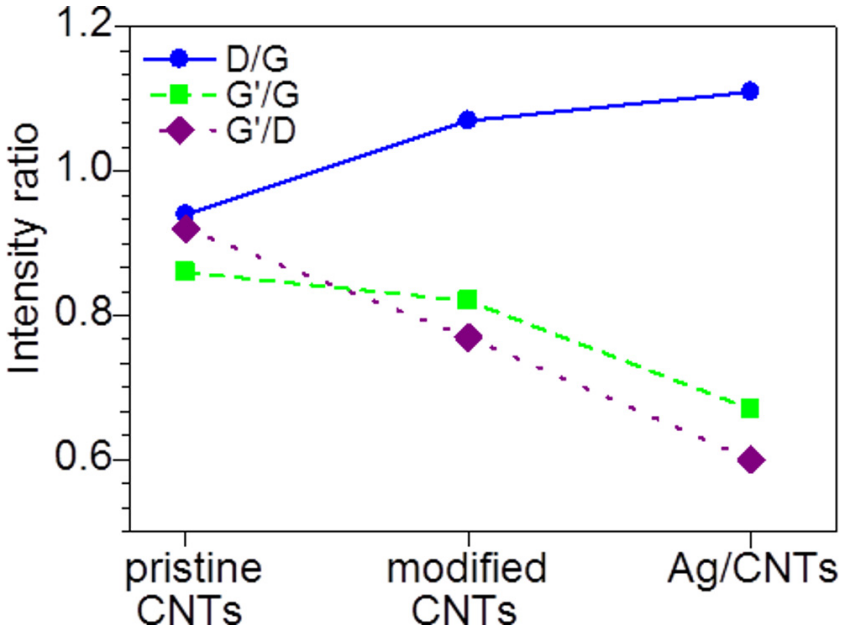

Fig. 4.5 Relative intensity ratios of D/G, G′/G, and G′/D peaks of pristine CNTs, modified CNTs, and Ag/CNT hybrid nanocomposites.

The D/G ratio is 0.94, 1.07, and 1.11 for the pristine CNTs, modified CNTs, and Ag/CNT hybrid nanocomposites, respectively. The increase of the D/G ratio of the modified CNTs compared with that of the pristine CNTs confirms the successful

introduction of functional groups onto the CNTs surface and that the outer layers of the CNTs were chemically modified [17, 19]. The slight increase between the D/G ratio of the modified CNTs and that of the Ag/CNT hybrid nanocomposites can be attributed to the introduction of Ag nanoparticles onto the surface of the CNTs. The G′/G ratio is 0.86, 0.82, and 0.67 for the pristine CNTs, modified CNTs, and Ag/CNT hybrid nanocomposites, respectively. Moreover, the G′/D ratio is 0.92, 0.77, and 0.60 for the pristine CNTs, modified CNTs, and Ag/CNT hybrid nanocomposites, respectively. The decrease of the G′/G and G′/D ratios of the modified CNTs compared with those of the pristine CNTs reveals a higher density of lattice defects in the acid-treated CNTs [22]. A decrease of the intensity of the G′ peak of the Ag/CNT hybrid nanocomposites (Fig. 4.4) as the mass fraction of CNTs in the hybrid material decreases is also clear. The G′ peak arises from a two-phonon process, so it is reasonable that its intensity decreases as the sample becomes less ordered (i.e., more impurities or introduced surface species), not allowing for the coupling effect that is required for the two-phonon process [25]. The G′/G and G′/D ratios of the Ag/CNT hybrid nanocomposites showed the lowest values because the CNTs were sonicated before being attached with Ag nanoparticles, which promotes the formation of structural defects. Attachment of Ag nanoparticles could also cause the G′/G and G′/D ratios to decrease through the interaction between the Ag nanoparticles and CNTs.

4.3.4 Electromagnetic wave absorption properties

Complex permittivity and complex permeability are basic parameters associated with the EM wave absorption properties of a material, where the real parts of complex permittivity and permeability represent the storage of electric and magnetic energies, respectively, while the imaginary parts symbolize the loss and dissipation of both energies [1, 2]. The complex permittivity (real part ε' and imaginary part ε'') of the modified CNTs composite (thickness, t = 1.0 mm) and Ag/CNT composite (t = 1.0 mm) loaded in paraffin wax in the range of 0.5-14.0 GHz is presented in Fig. 4.6. As the frequency increased, the complex permittivity decreased because the polarizabilities (electronic, ionic, and orientation) and electric displacement are not maintained in a changing EM field [26, 27]. The modified CNTs composite exhibited higher complex permittivity than the Ag/CNT hybrid nanocomposite. This can be explained by the high electrical conductivity of the CNTs that enables strong polarization to occur, Ohmic losses, dissipation of electrostatic charges, or multiple scattering caused by the large

specific area, which lead to improved complex permittivity [2, 16]. The behavior of the complex permittivity of the Ag/CNT hybrid nanocomposites can be attributed to the multiple interfacial polarizations between the Ag nanoparticles, CNTs, and paraffin wax [27]. Furthermore, the polarization mainly contains thermal ion polarization, dipole rotation polarization, electronic displacement polarization, ion polarization, and so on [1]. The time for electronic displacement and ion polarization is very short, thus these polarizations produce energy loss at high frequency region [1].

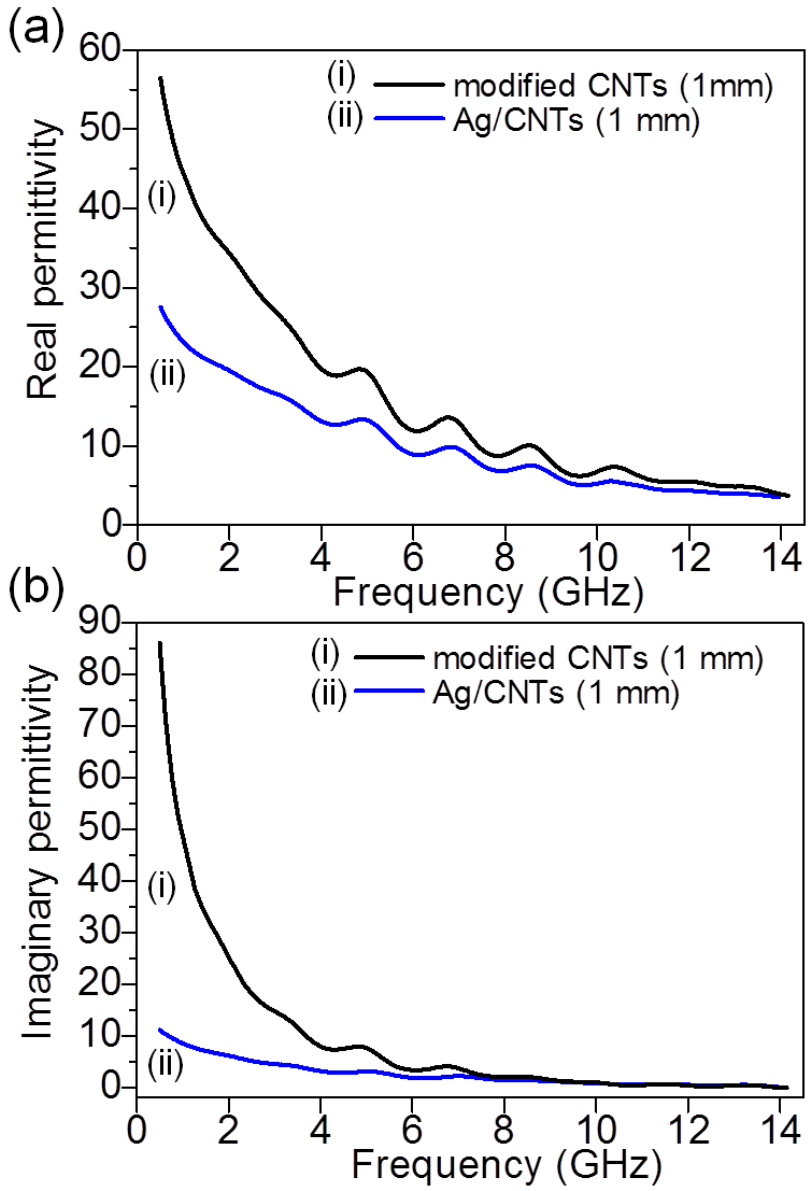

Fig. 4.6 Complex permittivity of the modified CNT composite (t = 1.0 mm) and Ag/CNT hybrid nanocomposite (t = 1.0 mm). (a) Real part permittivity, and (b) imaginary part permittivity.

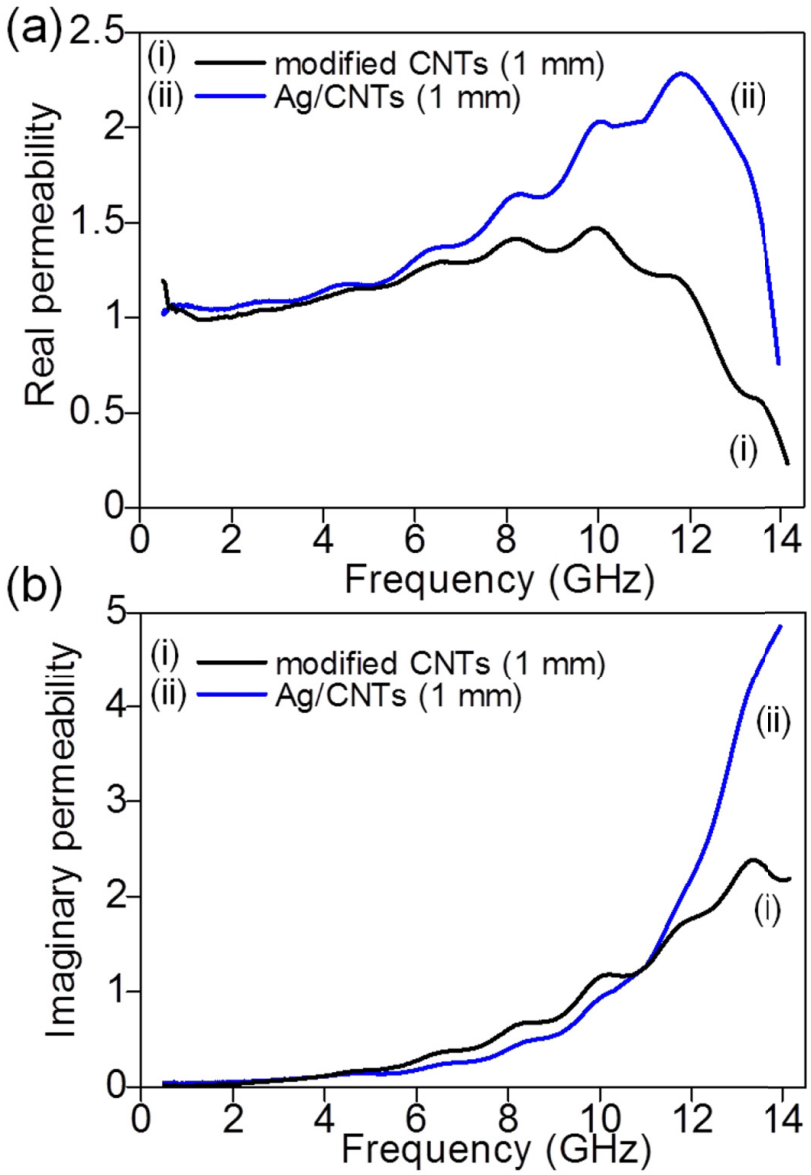

Fig. 4.7 Complex permeability of the modified CNT composite (t = 1.0 mm) and Ag/CNT hybrid nanocomposite (t = 1.0 mm). (a) Real part permeability, and (b) imaginary part permeability.

The complex permeability (real part μ', imaginary part μ'') of the modified CNTs composite (t = 1.0 mm) and Ag/CNT hybrid nanocomposite (t = 1.0 mm) in the range of 0.5-14.0 GHz is shown in Fig. 4.7. Interestingly, the presence of Ag nanoparticles affected the complex permeability of the hybrid nanocomposites. μ' of the Ag/CNT hybrid nanocomposite was higher than that of the modified CNTs composite, and increased until a certain frequency, after which it gradually decreased. This can be attributed to natural resonance or eddy current loss [1, 27]. When Ag (conducting

material) was put in an alternating magnetic field, a close induced current will be produced inside the material, which would dissipate the energy and referred as eddy current loss [1]. Both Ag and CNTs possess high electrical conductivity. This leads to permeability decreasing rapidly at high frequency caused by the eddy current loss. The strong attenuation of permeability with increasing frequency is due to the screening of the electromagnetic field by eddy currents [28]. This reduces the initial permeability and introduces a typical decaying envelope in the intrinsic permeability signal [28]. When a composite is exposed to a changing EM field, the Lorentz force on the electrons in the Ag nanoparticles provokes them to circulate, producing eddy currents [27]. A magnetic field induced by the eddy currents that opposes the applied field causes the composites to radiate an EM wave, which increases the total magnetic energy and results in decreased permeability [15, 27].

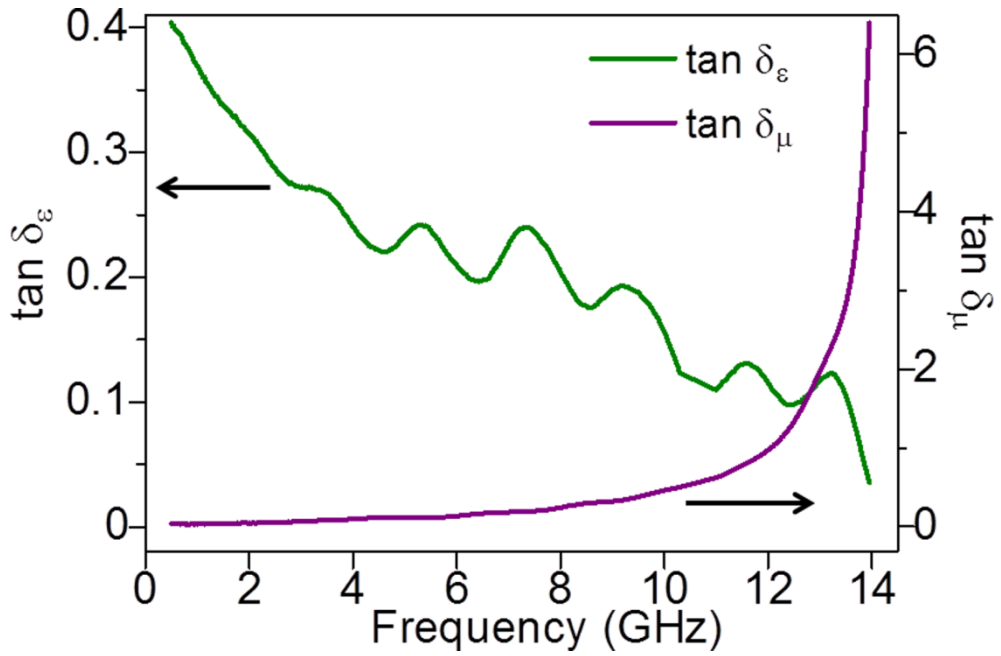

Fig. 4.8 Dielectric loss factor and magnetic loss factor of the Ag/CNT hybrid nanocomposite with t = 1.0 mm.

To reveal the intrinsic reasons for the EM wave absorption by the Ag/CNT hybrid nanocomposites, their dielectric loss factor (tan $\delta_\varepsilon = \varepsilon''/\varepsilon'$) and magnetic loss factor (tan $\delta_\mu = \mu''/\mu'$) were evaluated. Fig. 4.8 presents tan δ_ε and tan δ_μ of the Ag/CNT hybrid nanocomposite with t = 1.0 mm. The relaxation observed from tan δ_ε can be attributed from energy loss in the materials illuminated by EM field comes about through damping forces acting on polarized atoms and molecules and trough the finite conductivity of the

materials [2]. Both tan δ_ε and tan δ_μ contribute to the EM wave absorption; in the low-frequency region, tan δ_ε is sensitive to EM waves, and at high frequency, tan δ_μ is sensitive to EM waves.

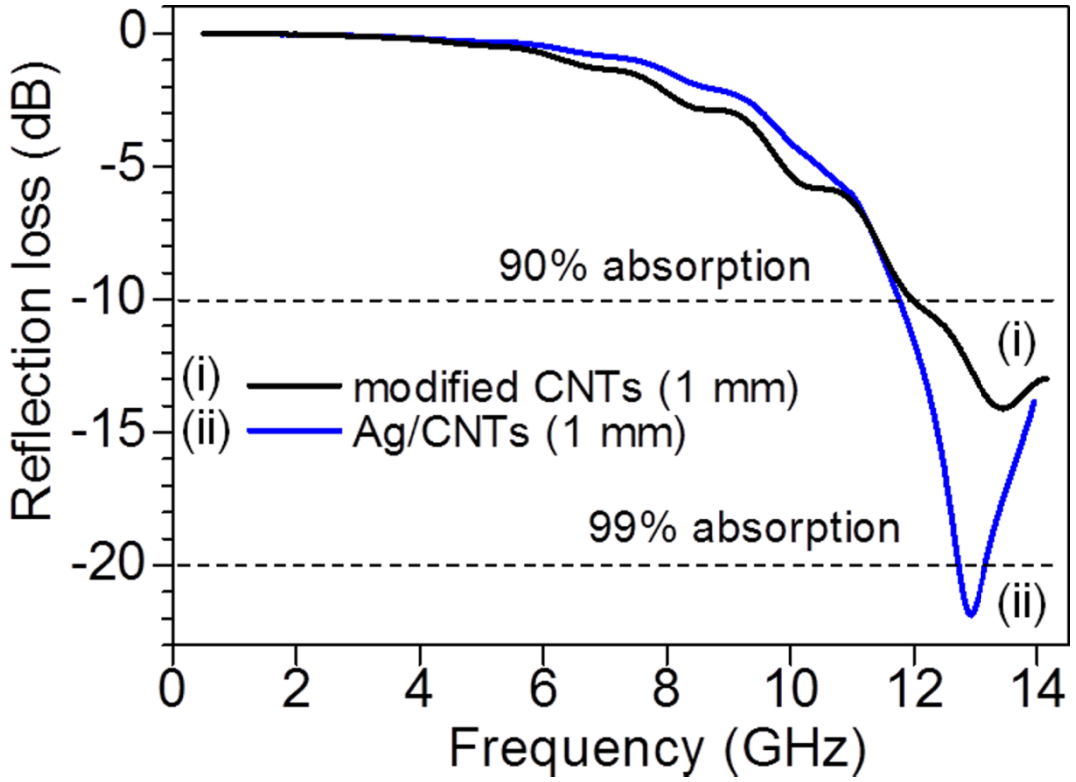

Fig. 4.9 Reflection loss of the modified CNT composite (t = 1.0 mm) and Ag/CNT hybrid nanocomposite (t = 1.0 mm) in the range of 0.5-14.0 GHz.

To investigate the EM wave absorption properties of the samples, the reflection loss (*R.L.*) was calculated according to the transmission line theory as follows:

$$R.L. = 20 \log \left| \frac{Z_{in} - 1}{Z_{in} + 1} \right| \tag{4.1}$$

where the normalized input impedance (Z_{in}) is given by the formula,

$$Z_{in} = \sqrt{\frac{\mu_r}{\varepsilon_r}} \tanh \left[j \left(\frac{2\pi f d}{c} \right) \sqrt{\mu_r \varepsilon_r} \right] \tag{4.2}$$

where $\varepsilon_r = \varepsilon' - j\varepsilon''$, $\mu_r = \mu' - j\mu''$, f is the EM wave frequency (Hz), d is the thickness of the absorber (m), and c is the velocity of light in free space (m/s). *R.L.* of the modified CNTs composite with t = 1.0 mm and the Ag/CNT hybrid nanocomposites with t = 1.0 mm are shown in Fig. 4.9.

The Ag/CNT hybrid nanocomposite with t = 1.0 mm showed a minimum *R.L.* of ~-21.9 dB (over 99% absorption) at 12.9 GHz. Furthermore, this sample also exhibited a wide response bandwidth of 2.3 GHz, where the frequency bandwidth (*R.L.* of less than -10 dB, over 90% absorption) is from 11.7 to 14.0 GHz. Conversely, the modified CNTs composite with t = 1.0 mm showed a minimum *R.L.* of ~-14.1 dB at 13.5 GHz with a response bandwidth of 2.0 GHz (12.0–14.0 GHz). The peak of the minimum *R.L.* shifted to lower frequency for the Ag/CNT hybrid nanocomposite compared with that of the modified CNTs composite of similar thickness. Moreover, *R.L.* and the response bandwidth of the Ag/CNT hybrid nanocomposite are both superior to the equivalent values of the modified CNTs composite. Even though the modified CNTs composite exhibited higher complex permittivity and complex permeability, the Ag/CNT hybrid nanocomposite was the better absorber because it showed a higher minimum *R.L.* According to Refs. [1, 2], suitable complex permittivity and complex permeability are essential to promote EM wave absorption. This also can be related to another important parameter connected to *R.L.*, *i.e.*, the concept of matched impedance. This concept suggests that the characteristic impedance of an absorber should be almost equal to that of the free space to achieve zero reflection on the front surface of the material [29-31]. Obviously, to design an optimized absorber with a high minimum *R.L.*, appropriate EM impedance matching is important.

There are many boundaries in the Ag/CNT hybrid nanocomposites, including between the Ag surfaces, CNT surfaces, and paraffin wax. Moreover, because the CNTs were modified both prior to and during the process of Ag nanoparticle coating, the Ag/CNT hybrid nanocomposites contain many defects and suspended bonds, as shown in the Raman spectra of the samples (Figs. 4.4 and 4.5). As a result, the large specific areas of the surfaces of the hybrid nanocomposites triggered higher interfacial polarization and multiple scattering, which leads to a high minimum *R.L.*. Interfacial multipoles contribute to the strong EM wave absorption of the hybrid nanocomposites.

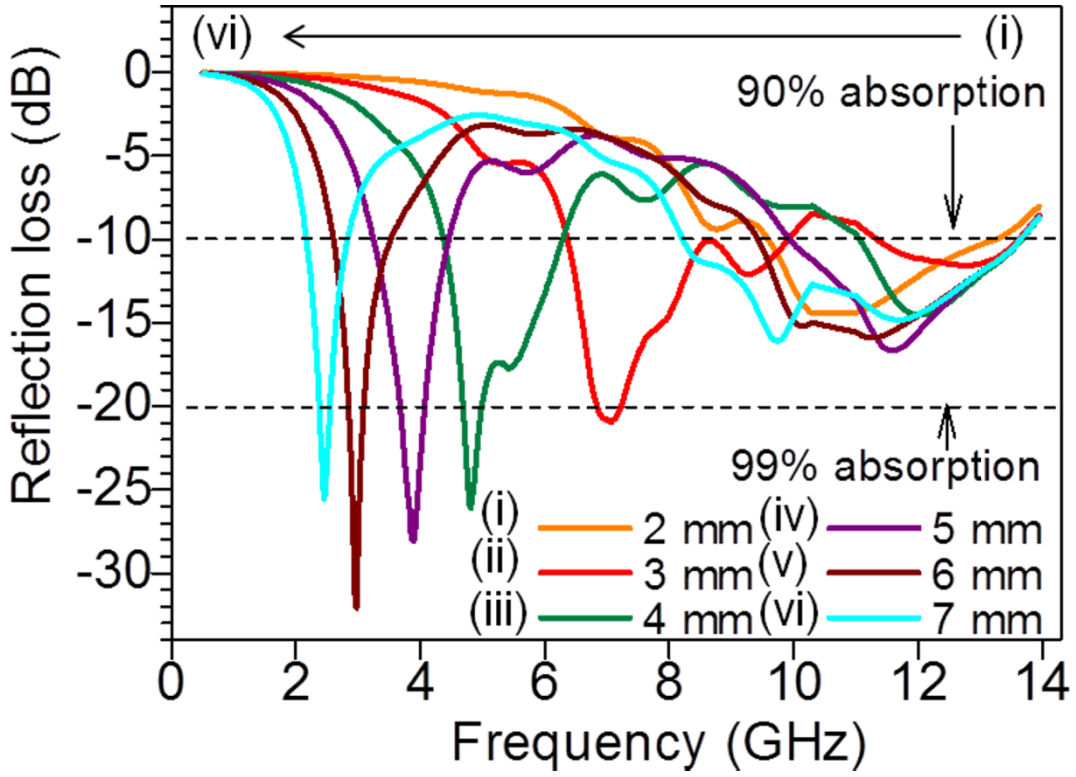

Fig. 4.10 Reflection loss of the Ag/CNT hybrid nanocomposite (t = 2.0, 3.0, 4.0, 5.0, 6.0, and 7.0 mm) in the range of 0.5-14.0 GHz.

According to Eq. (4.2), the thickness of the absorber can also affect *R.L.*, so we investigated the relationship between the thickness and *R.L.* of the Ag/CNT hybrid nanocomposites. *R.L.* for Ag/CNT hybrid nanocomposites with t = 2.0, 3.0, 4.0, 5.0, 6.0, and 7.0 mm was calculated and shown in Fig. 4.10. When the thickness of the Ag/CNT hybrid nanocomposite increased, the frequency of the *R.L.* peak decreased. When t = 3.0 mm and above, extra peak was observed at lower frequency region, between 0.5 to 9.0 GHz. The *R.L.* peaks at higher frequency showed over 90% absorption (<-10 dB) meanwhile the *R.L.* peaks at lower frequency showed over 99% absorption (<-20 dB). As the thickness increased beyond t = 3.0 mm, the *R.L.* peak (response bandwidth) at high frequency region become broader; and *R.L.* peak at low frequency region become narrower. The Ag/CNT hybrid nanocomposite with t = 6.0 mm showed a minimum *R.L.* of ~-32.1 dB (over 99.9% absorption) at 3.0 GHz and was the best absorber when compared with the other samples of different thickness. Furthermore, they also showed *R.L.* of less than -10 dB, from 2.6 to 3.5 GHz (low frequency region) and 9.4 to 13.7 GHz (high frequency region), respectively. These results show that the frequency related to the minimum *R.L.* (highest absorption) of the Ag/CNT hybrid nanocomposites

can be controlled by changing the thickness of the sample. Furthermore, absorption at low and high frequency region also can be archived by changing the thickness of Ag/CNT hybrid nanocomposites. We believe that the Ag/CNT hybrid nanocomposites are a promising EM wave absorber, because their absorption band can be modulated simply by manipulating the sample thickness to satisfy applications in different frequency bands.

4.4 Conclusions

Ag nanoparticles were grafted onto the surface of CNTs to fabricate Ag/CNT hybrid nanomaterials. TEM, XPS, and Raman spectroscopy analyses revealed the morphology, structure, and elemental composition of the hybrid nanomaterials. The Ag nanoparticles were less than 10 nm in diameter and showed no agglomeration when adhered to the surface of CNTs. The high interfacial area of the hybrid nanomaterials results in high interfacial polarization and multiple scattering, which improves EM wave absorption. The Ag/CNT hybrid nanomaterials exhibited a minimum *R.L.* of ~-21.9 dB (over 99% absorption) at 12.9 GHz with a wide response bandwidth (2.3 GHz), superior than the modified CNTs composite with same thickness of 1.0 mm. Furthermore, the Ag/CNT hybrid nanomaterials, t = 6.0 mm showed a minimum *R.L.* of ~-32.1 dB (over 99.9% absorption) at 3.0 GHz and was the best absorber when compared with the other samples of different thickness. The Ag/CNT hybrid nanomaterials showed two *R.L.* peaks, at low and high frequency region, as the thickness of the sample increased. They also showed wide minimum *R.L.* of over -10 dB (over 90% absorption). This proves that the thickness of the samples can be manipulated to produce absorption bands at different frequencies to design highly effective EM wave absorbers.

References

[1] J. Huo, L. Wang, H. Yu, J. Mater. Sci. 44 (2009) 3917-3927.

[2] F. Qin, C. Brosseau, J. Appl. Phys. 111 (2012) 061301.

[3] H. L. Zhu, Y. J. Bai, R. Liu, N. Lun, Y. X. Qi, F. D. Han, X. L. Meng, J. Q. Bi, R. H. Fan, AIP Adv. 1 (2011) 032140.

[4] G. V. Ramesh, K. Sudheendran, K. C. J. Raju, B. Shreedhar, T. P. Radhakrishnan, J. Nanosci. Nanotechnol. 9 (2009) 261-266.

[5] C. H. Peng, H. W. Wang, S. W. Kan, M. Z. Shen, Y. M. Wei, S. Y. Chen, J. Magn. Magn. Mater. 284 (2004) 113-119.

[6] P. C. Ma, B. Z. Tang, J. K. Kim, Carbon 46 (2008) 1497-1505.

[7] Y. Jiang, Y. Lu, L. Zhang, L. Liu, Y. Dai, W. Wang, J. Nanopart. Res. 14 (2012) 938.

[8] L. Chen, H. Xie, W. Yu, J. Mater. Sci. 47 (2012) 5590-5595.

[9] W. Zhang, W. Li, J. Wang, C. Qin, L. Dai, Fibers Polym. 11 (2010) 1132-1136.

[10] G. W. Yang, G. Y. Gao, C. Wang, C. L. Xu, H. L. Li, Carbon 46 (2008) 747-752.

[11] R. X. Dong, C. T. Liu, K. C. Huang, W. Y. Chiu, K. C. Ho, J. J. Lin, ACS Appl. Mater. Interfaces 4 (2012) 1449-1455.

[12] D. L. Zhao, X. Li, Z. M. Shen, Mater. Sci. Eng. B 150 (2008)105-110.

[13] D. L. Zhao, X. Li, Z. M. Shen, Compos. Sci. Technol. 68 (2008) 2902-2908.

[14] A. Katsounaros, K. Z. Rajab, Y. Hao, M. Mann, W. I. Milne, Appl. Phys. Lett. 98 (2011) 203105.

[15] L. Deng, M. Han, Appl. Phys. Lett. 91 (2007) 023119.

[16] T. H. Ting, Y. N. Jau, R. P. Yu, Appl. Surf. Sci. 258 (2012) 3184-3190.

[17] L. Zhang, Y. Hashimoto, T. Taishi, Q. Q. Ni, Appl. Surf. Sci. 257 (2011) 1845-1849.

[18] S. H. Lee, C. C Teng, C. C. M. Ma, I. Wang, J. Colloid Interface Sci. 364 (2011) 1-9.

[19] L. Zhang, Q. Q. Ni, A. Shiga, T. Natsuki, Y. Fu, Polym. Eng. Sci. 51 (2011) 1525-1532.

[20] J. Natsuki, T. Natsuki, T. Abe, J. Nanopart. Res. 15 (2013) 1483.

[21] J. Natsuki, T. Abe, J. Colloid Interface Sci. 359 (2011) 19-23.

[22] S. Santangelo, G. Messina, G. Faggio, M. Lanza, C. Milone, J. Raman. Spectrosc. 42 (2011) 593-602.

[23] Y. Lin, K. A. Watson, M. J. Fallbach, S. Ghose, J. G. Smith Jr., D. M. Delozier, W.

Cao, R. E. Crooks, J. W. Connell, ACS Nano 3 (2009) 871-884.

[24] P. Corio, A. P. Santos, P. S. Santos, M. L. A. Temperini, V. W. Brar VW, M.A. Pimenta, M.S. Dresselhaus, Chem. Phys. Lett. 383 (2004) 475-480.

[25] R. A. DiLeo, B. J. Landi, R. P. Raffaelle J. Appl. Phys. 101 (2007) 064307.

[26] G. Wang, X. Chen, Y. Duan, S. Liu, J. Alloys Compd. 454 (2008) 340-346.

[27] H. Wu, L. Wang, Y. Wang, S. Guo, Z. Shen, Mater. Sci. Eng. B 177 (2012) 476-482.

[28] A. D. C. Viegas, M. A. Correa, L. Santi, R. B. da Silva, F. Bohn, M. Carara, R. L. Sommer, J. Appl. Phys. 101 (2007) 033908.

[29] J. H. Kim, S. S. Kim, J. Alloys Compd. 509 (2011) 4399-4403.

[30] C. Cui, Y. Du, T. Li, X. Zheng, X. Wang, X. Han, P. Xu, J. Phys. Chem. B 116 (2012) 9523-9531.

[31] Q. Yuchang, Z. Wancheng, L. Fa, Z. Dongmei Z, J. Magn. Magn. Mater. 323 (2011) 600-60

Chapter 5

****

EAP actuator incorporated with microwave-induced polymerization treated CNTs

****

5 EAP actuator incorporated with microwave-induced polymerization treated CNTs

5.1 Introduction

Shape memory materials have recently received much attention as they are promising smart materials. In contrast to other shape memory materials such as shape memory alloys or shape memory ceramics, shape memory polymers (SMPs) are light, have low density, have low cost, and are easy to fabricate [1-11]. The shape memory effects can be obtained by external stimulations such as heat, electric fields, magnetic fields, pH, light, or vapor [1-11]. Generally, SMPs have been evaluated using heat stimulation. However, not only heat, stimulations such as electric fields will enable the manipulation of shape memory behavior at ambient temperature and eliminate the temperature constraints arising from external heating [2, 3]. An electric field-stimulated polymer-based actuators are referred to as electroactive polymers (EAPs) and can be considered as a type of SMP [11-14]. They are soft and flexible materials that can convert electrical energy to mechanical energy and thus impart a force and produce large strain [11-19]. They can be applied for actuator materials, sensors, artificial muscles, smart devices, and microswitches [4, 10-12, 14, 15, 19-21].

Generally, polyurethane (PU) are insulators and they are light, soft, flexible, easy to fabricate, and have been reported to generate deformation and large strain under electric field stimulation [12-14, 22]. Meanwhile, carbon nanotubes (CNTs) are also light, possess a high aspect ratio, and have outstanding mechanical, chemical, and electric properties [12, 15, 19, 23-27]. Upon combining a polymer (PU) with an electric conductor (CNTs) as a filler, new and unique polymer-based nanocomposites can be fabricated. However, CNTs disperse poorly in organic and aqueous solvents because of a strong intrinsic van der Waals attraction [23-26]. Sahoo et al. [10] investigated the influence of CNTs in a PU nanocomposite actuator. To improve the dispersion of CNTs they conducted strong acid treatment. In contrast, microwave-induced polymerization treatment that is relatively environment friendly, fast, efficient, and allows for easy modification has been performed [25, 26]. No harsh organic or aqueous solvents were

used in this process and it is thus a less destructive modification route.

Jo et al. [13] and Nakama et al. [28] investigated the bending electrostriction of PU-based films. The bending deformation of PU-based films under the application of an electric field was measured and the mechanism was briefly discussed in their reports. Furthermore, Watanabe et al. [14, 22] and Ali et al. [20] reported bending deformation of PU-based films and polyvinyl chloride (PVC) gels, respectively. Electrical properties were evaluated and presented in their reports. Charge transfer and accumulation within the samples when voltage is applied are discussed and can be considered as a new approach to understand the charge distribution behavior and actuation behavior.

In this chapter, we combined PU and microwave-induced polymerization-treated CNTs to develop a polymer-based nanocomposite actuator. The structure and morphology of modified CNTs were also examined. The objective was to evaluate their actuation behavior, electrical properties, and charge distribution behavior. This also included investigation to understand the mechanism of actuation when an electric field is applied.

5.2 Materials and methods

5.2.1 Microwave-induced polymerization treatment

Microwave-induced polymerization treatment [25, 26] that is fast and efficient was performed to improve the dispersion of the CNTs. Multi-walled CNTs (Wako Pure Chemical Industries, Japan, d = 20-30 nm) were used. N,N-dimethylformamide (DMF; Wako Pure Chemical Industries), methyl methacrylate (MMA; Wako Pure Chemical Industries), and benzoyl peroxide (BPO; Acros Organics) were used as the reagent in radical reaction treatment. Fifty milligrams of CNTs were ultrasonically mixed in 15 ml DMF solution containing 1 ml MMA, and 10 mg BPO in 5 ml DMF solution was added to the total solution. The total solution was then ultrasonically mixed for 5 min and irradiated for about 12 s with microwaves. The process was repeated five times for a total addition of 50 mg BPO. Then, the solution was centrifuged and DMF was added once again for three times repetition. Finally, the solutions were filtered and rinsed with pure water and ethanol. The products were dried overnight at 50°C. The treated CNTs were denoted as modified CNTs hereafter.

5.2.2 Fabrication of PU/CNTs film

The modified CNTs and DMF were ultrasonically mixed for 10 min. Then, the solution was added to PU (DiARY MS-4510, Diaplex) and mixed at 8000 rpm for 5 min using a high-speed homogenizer. After this mixing the mixture was degassed. The mixture was then applied to the glass plate of an auto film applicator and dried at 50°C for 8 h using a heat gun. The fabricated samples are PU films and PU/CNTs films combined with modified CNTs. PU films were fabricated using the same method excluding the addition of CNTs. PU/CNTs films were fabricated by loading the modified CNTs into the PU with a weight fraction of 0.1, 0.5, and 1.0 wt.% (thickness: 0.1 mm). Some of the films were coated with thin silver coating (about 3 μm) for the evaluation of actuator performance. Uncoated films are denoted as PU and PU/CNTs, meanwhile coated films are denoted as C-PU and C-PU/CNTs, hereafter.

5.2.3 Evaluation method

The dispersion of pristine CNTs (10 mg) and modified CNTs (10 mg) in a polar solvent (DMF, 10 ml) after mixing and after 1 week were evaluated. Transmission electron microscopy (TEM) images were obtained using a TEM (JEM-2100, JOEL, Japan) with an accelerating voltage of 200 kV. The cross-sectional morphology of the films was observed using field emission scanning electron microscopy (FE-SEM, Hitachi S-5000, 20 kV). The films were fractured in liquid nitrogen and the cross-sectional surfaces were coated with thin platinum-palladium coating for FE-SEM observation. Thermogravimetric analysis (TGA, Rigaku Thermo Plus TG8120) was conducted in the presence of Argon gas flow from room temperature to 550°C at a heating rate of 10°C/min. X-ray photoelectron spectrometry (XPS, Kratos Axis Ultra DLD) was carried out to measure elemental composition of the samples with a standard Mg Kα (1256.6 eV) X-ray source operating at 10 mA and 15 kV.

Actuator performance was evaluated by measuring the bending displacement of the films using a laser displacement meter (Keyence LK-G3000V), a controller (Keyence LK-GD500) and a high-voltage power supply (Matsusada Precision, HJPQ-30P1). The experimental setup is shown in Fig. 5.1(a). The films were cut into 5 × 35 mm rectangles, vertically suspended in air, and sandwiched between the electrodes. Upon the application of DC voltage, the bending displacement of the films was measured at room temperature.

Volume resistivity of the film was measured using resistivity meter (Mitsubishi

Chemical Analytech, MCPHT450). Constant-voltage supplied method and ring probe were used to measure the volume resistivity. The samples with diameter larger than the ring probe diameter and thickness 0.1 mm were evaluated.

The permittivity (dielectric spectroscopy) of the film was measured using an impedance analyzer and a dielectric interface (Solartron Analytical Co.). The films were analyzed using an applied voltage of 100 mV and sweep frequencies from 1 Hz to 1 MHz at room temperature. Then, the impedance analysis of the films was performed. Furthermore, the complex impedance spectra were analyzed using ZView software to conduct Cole-Cole plot analysis and equivalent circuit evaluation.

To determine the charge distribution in the thickness direction of the films, space charge measurement was conducted. The space charge measurement was obtained using a pulsed electroacoustic nondestructive test system (Five Lab, PEANUTS). The experimental setup is shown in Fig. 5.1(b). When a pulsed voltage is applied to the films they deform instantaneously and produce an elastic wave within the films (thickness direction). If charge exists within the films, the Coulomb force of the charge produced an elastic wave. This signal (elastic wave) will be detected by a piezoelectric sensor and observed as amplitude that depends on the amount of charge. The pulsed voltage is 100 V and applied voltage is varied from 100-1000 V at room temperature. Circular samples with a diameter of 12 mm (larger than the sensor diameter) and a thickness of 0.1 mm were used and placed between the sensor electrodes under normal pressure for measurements.

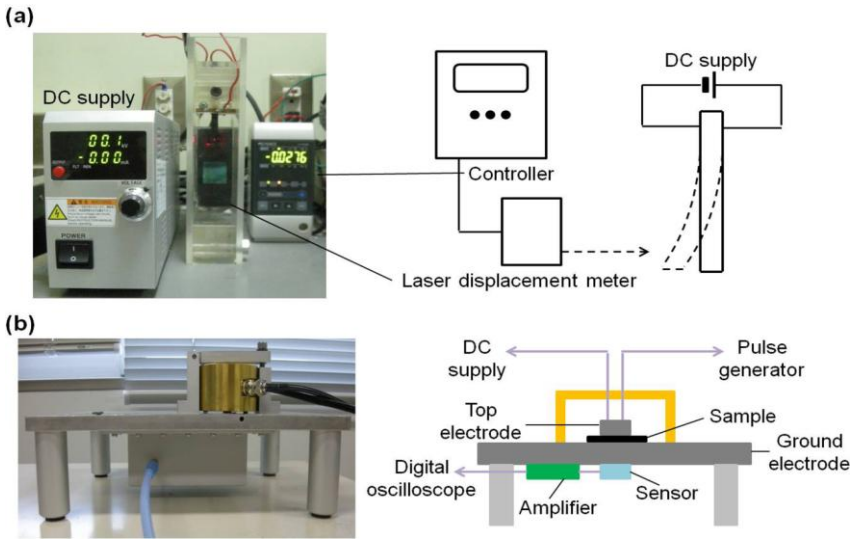

Fig. 5.1 Experimental setup (a) actuation performance test and (b) space charge measurement.

5.3 Results and discussion

5.3.1 Evaluation of microwave-induced polymerization treated CNTs

The dispersion of modified CNTs in the DMF improved compared with pristine CNTs, as shown in Fig. 5.2(a) and (b). After mixing, all the CNTs dispersed well in DMF (Fig. 5.2(a)). However, after 1 week (Fig. 5.2(b)), the pristine CNTs precipitated while the modified CNTs were uniformly dispersed in DMF. The introduction of MMA onto the surface of CNTs led to enhanced oxygen functional groups and thus uniform dispersion in the polar solvent (DMF).

TEM images of the pristine CNTs and modified CNTs are depicted in Fig. 5.3(a)-(c). FE-SEM images of the modified CNTs and dispersion of them in the PU are presented in Fig. 5.3(d) and Fig. 5.3(e) and (f), respectively. From Fig. 5.3(a), the pristine CNTs showed some aggregation between them. From Fig. 5.3(b) and (c), modified CNTs showed less aggregation between them and better dispersion compared with the pristine CNTs. Furthermore, from Fig. 5.3(b)-(d), MMA grafted onto the surface of CNTs can be confirmed. Moreover, from Fig. 5.3(e) and (f), the modified CNTs showed uniform distribution and no aggregation in the PU matrix. The good dispersion of CNTs is due to that the modification of CNTs enhanced the interaction between the CNTs and PU. Carboxyl and hydroxyl functional groups of the modified CNTs led to well-dispersed PU/CNTs films. The introduction of functional groups to the CNTs allows covalent bonding of PU directly to the nanotube framework and significantly improves the interface between the PU and the modified CNTs [12, 29]. Microwave-induced polymerization treatment thus improves the dispersion of pristine CNTs. The carboxyl and hydroxyl groups of treated CNTs will be discussed in the XPS result below.

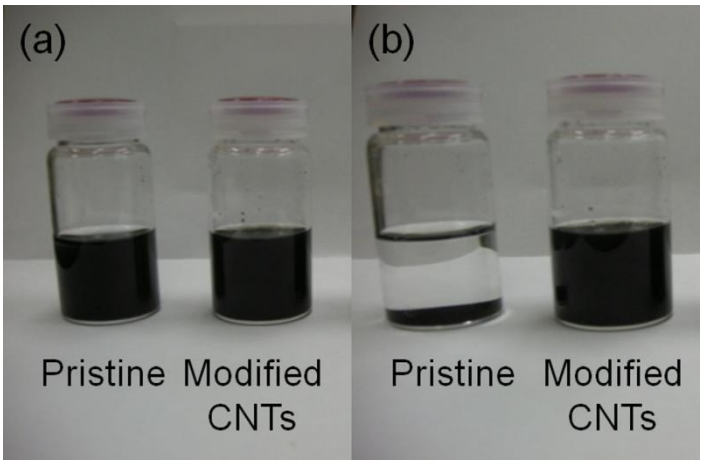

Fig. 5.2 Dispersion of the CNTs in a polar solvent (a) after mixing and (b) after 1 week.

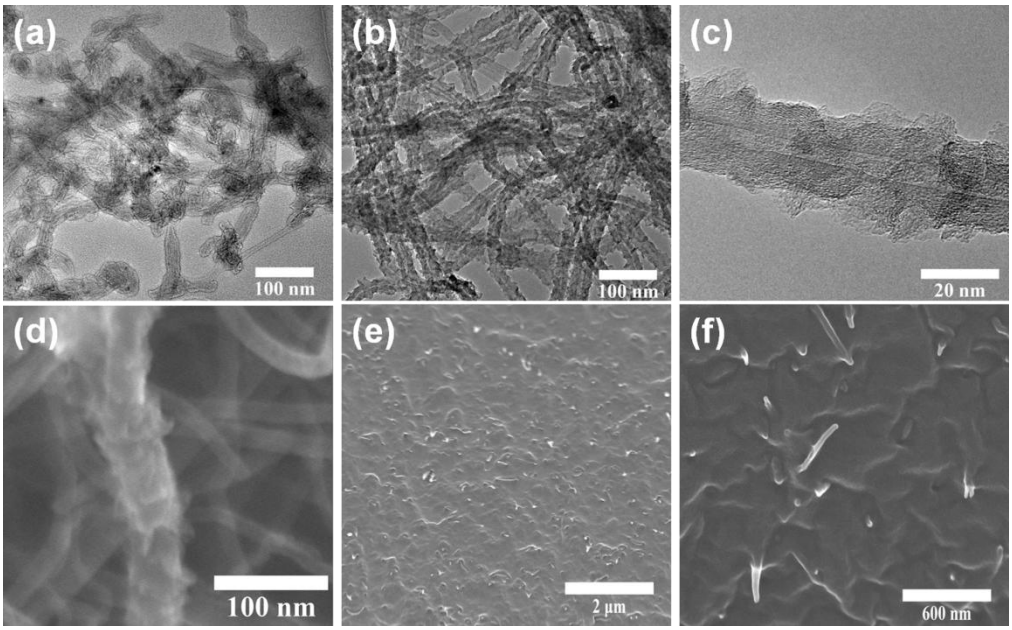

Fig. 5.3 TEM images of (a) pristine CNTs, (b) and (c) modified CNTs; FE-SEM images of (d) modified CNTs, (e) and (f) cross section of PU/CNTs film.

TGA was used to examine the amount of mass reduction of the MMA that was grafted onto the surface of CNTs and the results are as shown in Fig. 5.4. Up to about 170°C, the weight loss of pristine CNTs and modified CNTs corresponded to the evaporation of the absorbed water. At the temperature range of 170-550°C, the weight loss of modified CNTs was attributed to the decomposition of the surface-grafted MMA. The weight loss of the modified CNTs was about 4 wt.%.

To investigate the oxygen functional groups (carboxyl and hydroxyl groups) of the modified CNTs, XPS evaluation was carried out. The XPS spectra are shown in Fig. 5.5. The modified CNTs showed a higher intensity oxygen (O 1s) peak compared with the pristine CNTs. The atomic percentage ratios for the pristine CNTs are 98.51% for C 1s and 1.49% for O 1s. Meanwhile, the modified CNTs gave 94.05% for C 1s and 5.95% for O 1s. The higher O 1s peak confirmed that many oxygen functional groups were attached to the surface of these CNTs. These oxygen functional groups are the reason for the modified CNTs dispersing uniformly in the polar solvent and PU matrix. From the TEM, FE-SEM, TGA, and XPS results we also can conclude that this modification was successful as the MMA was grafted onto the surface of CNTs and carboxyl and hydroxyl groups were also introduced to the surface of the CNTs.

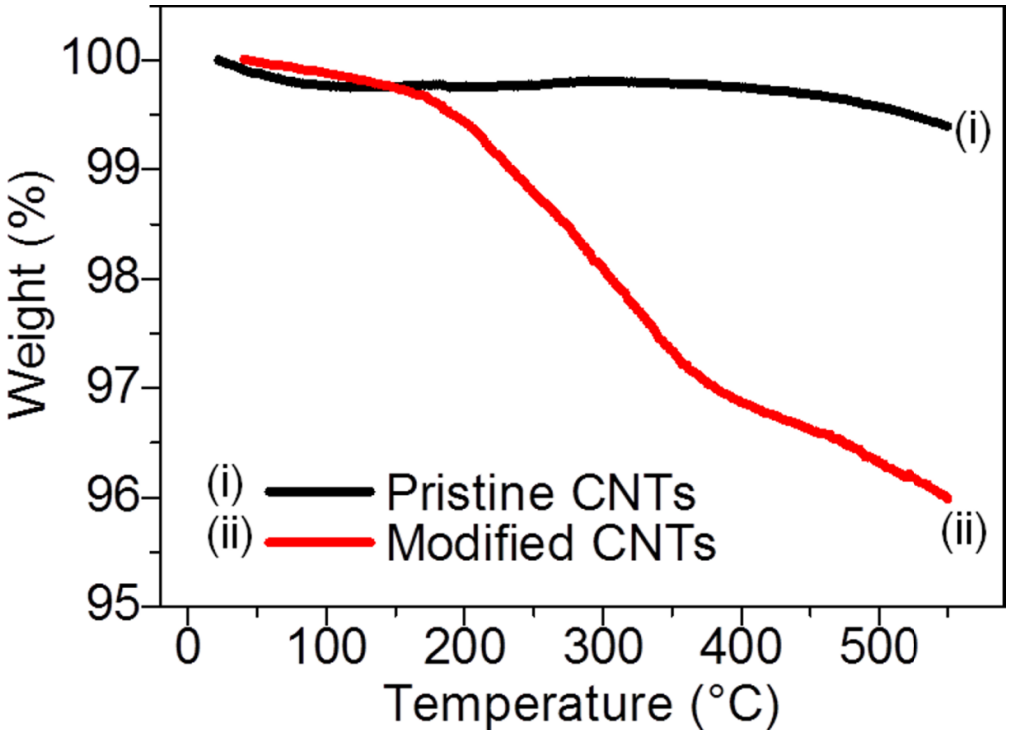

Fig. 5.4 TGA curves of pristine and modified CNTs.

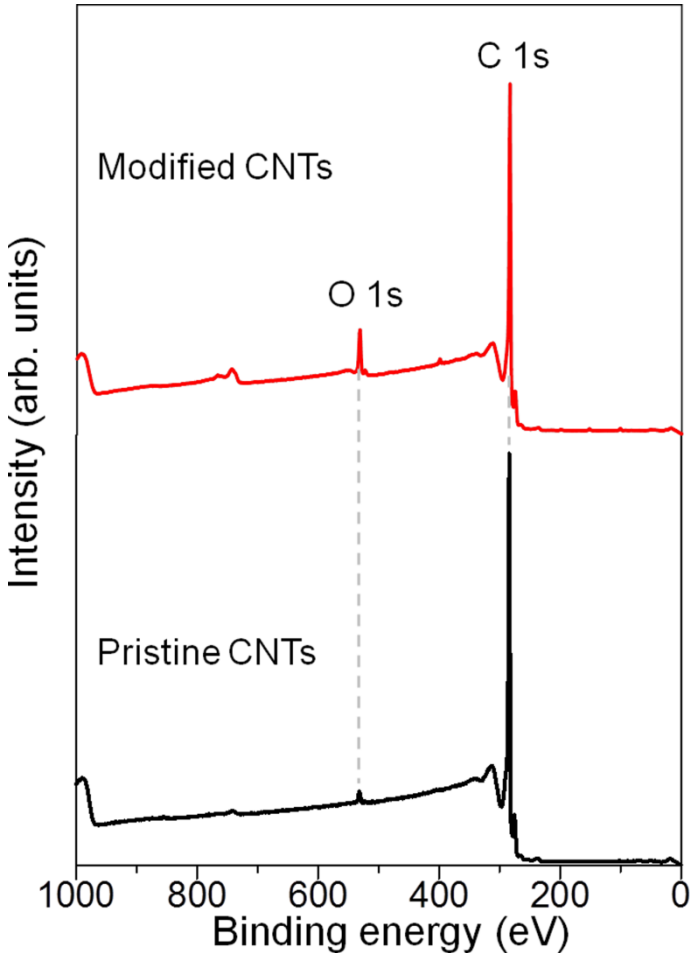

Fig. 5.5 XPS spectra of pristine CNTs and modified CNTs.

5.3.2 Actuator performance

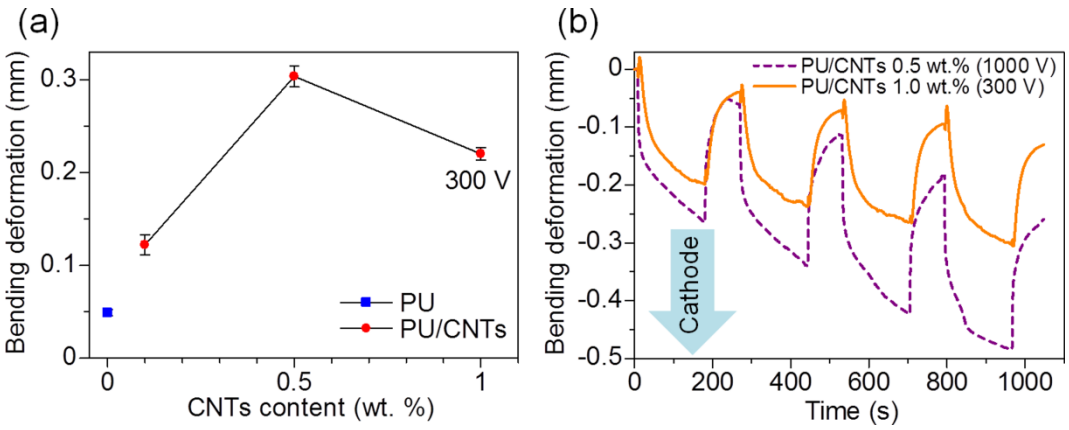

Fig. 5.6 Actuation performance of uncoated films: (a) bending deformation and (b) representative actuation upon application of 300 V and 1000 V.

The bending displacement of the uncoated films when voltage was applied is shown in Fig. 5.6(a). The representative actuation upon application of 300 V (PU/CNTs 1.0 wt.%) and 1000 V (PU/CNTs 0.5 wt.%) are as shown in Fig. 5.6(b). The films bent toward the cathode when the voltage was applied and reverted close to the original position when the voltage was removed. The voltage applied to the films was 1000 V except for PU/CNTs 1.0 wt.% that was 300 V. High voltage damages some films, i.e., burnt holes caused by overheating in the area sandwiched between the electrodes. The bending displacement increased as the CNTs content increased. Even with the application of a lower voltage for PU/CNTs 1.0 wt.%, they showed relatively high bending displacement. This shows that low energy consumption is adequate for higher CNT content films and they are more efficient at energy conversion. The highest bending displacement was obtained for the PU/CNTs 0.5 wt.% film and its average bending displacement was found to be about 0.3 mm. The PU/CNTs films gave a higher bending displacement compared with the PU films; thus, the PU/CNTs films had better actuation properties compared with the PU films. From Fig. 5.6(b), similar bending displacement can be observed in each voltage cycle. This phenomenon can be considered to be a type of memory where the electric field reminds the films of the electrically memorized strain, which also indicates that the actuation is reproducible and stable upon voltage cycling [12, 20]. Furthermore, the recovery after the application of voltage for PU/CNTs 0.5 wt.% was lower than PU/CNTs 1.0 wt.%. The application of 1000 V to PU/CNTs 0.5 wt.% might have caused higher residual strain in contrast to

PU/CNTs 1.0 wt% (300 V). Thus, with the low recovery and higher residual strain of PU/CNTs 0.5 wt.%, their bending displacement decreased as the voltage cycle and time increased.

Furthermore, we also investigated the bending displacement of PU/CNTs films that were coated with thin silver coating. The coated films also bent to the cathode side when voltage was applied. The bending displacement and ratio of d/L (where d is bending displacement and L is the length of the sample) of the coated films are shown in Fig. 5.7(a). The bending actuation of C-PU/CNTs 0.1 wt.% is shown in Fig. 5.7(c) and (d). The coated film showed bending actuation and shifted from its original position when the voltage was applied. The C-PU/CNTs films gave a higher bending displacement compared with the C-PU films. The C-PU/CNTs 0.1 wt.% film showed the highest average bending displacement and d/L ratio, about 3.0 mm and 0.093, respectively, upon the application of 1000 V. However, the C-PU/CNTs 1.0 wt.% upon the application of 10 V showed comparably high average bending displacement about 2.4 mm. Even with the application of a lower voltage, the bending displacement of the coated films increased as the CNTs content increased. The comparison of other EAPs actuation performance is not straightforward because the test performed for each type of actuator is different [11]. In comparison with some common EAPs, PU with various polyols [13], PU that had phenylimino (N-PU) and nitrophenyl (Nt-PU) groups [14], polyvinyl chloride (PVC) gel actuator [20], and electroactive paper actuator coated with polypyrrole [16], our C-PU/CNTs films showed superior bending displacement, although the applied voltage and conditions are varied. The nanocomposite films that were fabricated also can be applied to a wider application considering the special features of CNTs that were incorporated in PU. The relationship between voltage and actuation of C-PU and C-PU/CNTs 0.1 wt.% films is plotted in Fig. 5.7(b). No significant actuation was observed in the coated films for an applied voltage less than 300 V but the bending displacement increased as the applied voltage increased beyond 300 V. This showed that the films are dependent on the applied voltage and this greatly affected the actuation. To evaluate the films as part of a practical actuator it is important to evaluate the films under repetitive voltage cycle. A repeat voltage of 10 V was applied to the coated PU/CNTs 0.5 wt.% and 1.0 wt.% film and the bending displacement is shown in Fig. 5.8. The coated films bent toward the cathode when the voltage was applied and reverted close to the original position when the voltage was removed. As the time (repetitive voltage cycle) increases, the bending displacement

curves shifted up. After the voltage was removed, the films reverted to their original position and gradually the reversion over 0 mm (y-axis, upper) increased. The films are considered to be an elastic body and they showed elastic recovery when the voltage was removed. Furthermore, small amount of heat generated upon the actuation might enhance the reversion over 0 mm. C-PU/CNTs 1.0 wt.% film showed higher bending displacement rather than C-PU/CNTs 0.5 wt.% and the result is in agreement with the result shown in Fig. 5.7(a). Each cycle is about 65 s and the films showed maximum bending displacement over the cycle. The films showed maximum bending displacement about 25 s after voltage was applied, thus gave a fast response. The coated films also exhibited electrically memorized strain actuation. Furthermore, their stable and reproducible actuation under repetitive voltage cycling also proved that they can be used for practical application and a promising actuator material.

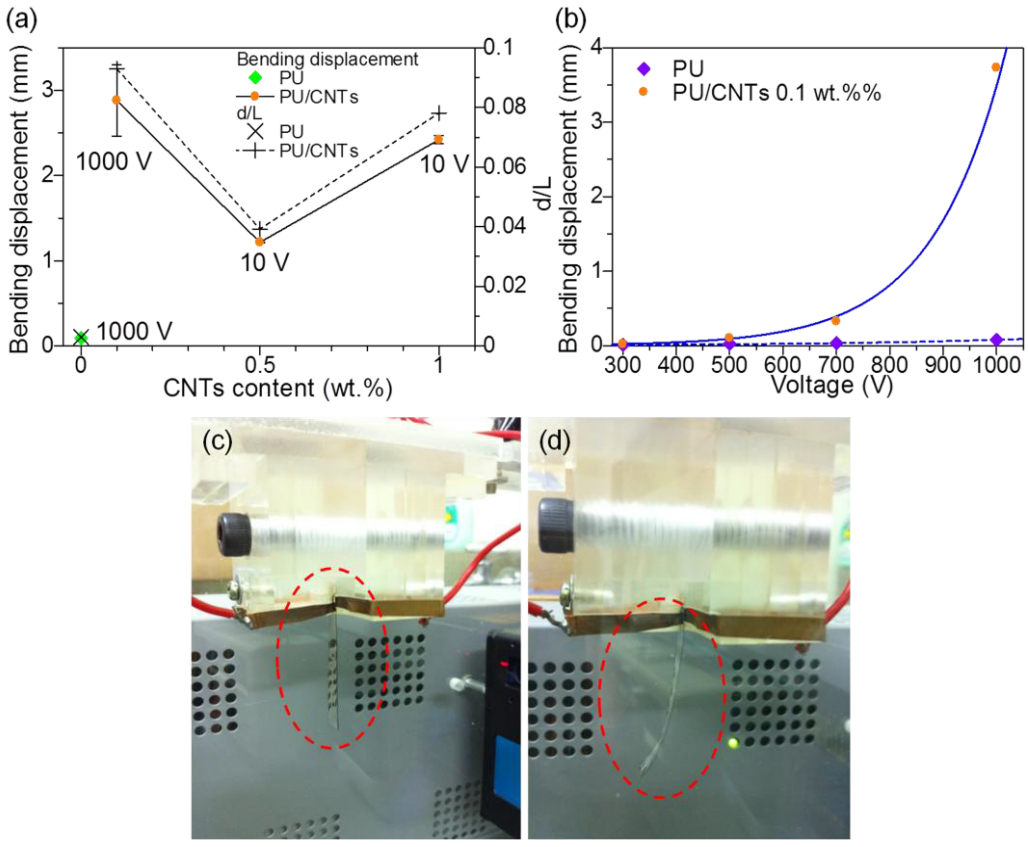

Fig. 5.7 Actuator behavior of coated films (a) bending displacement and *d*/*L* ratio of C-PU and C-PU/CNTs 0.1 wt.% film (1000 V) and C-PU/CNTs 0.5 wt.% and 1.0 wt.% (10 V) (b) relationship between voltage and bending displacement (c) before actuation C-PU/CNTs 0.1 wt.% film (1000 V) (d) after actuation C-PU/CNTs 0.1 wt.% film (1000 V).

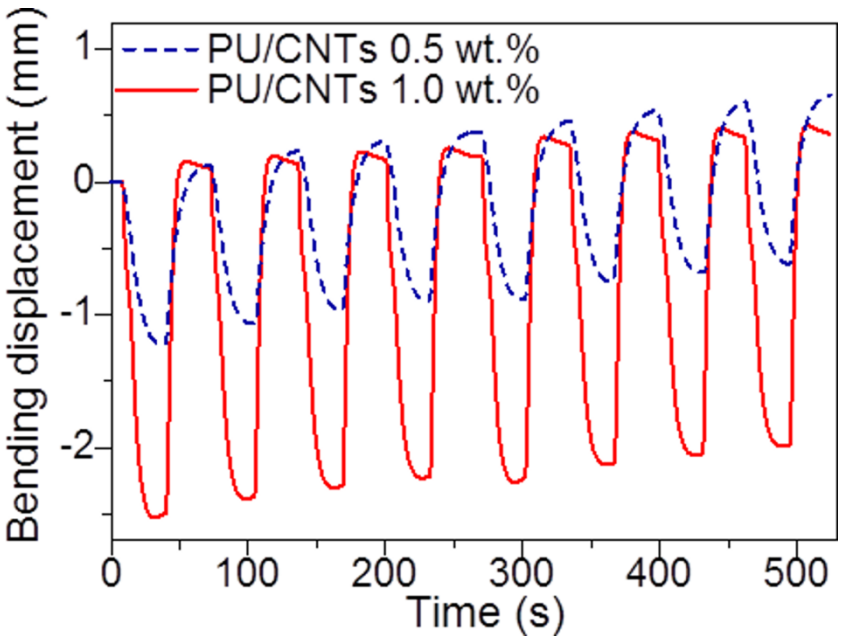

Fig. 5.8 Actuator performance of C-PU/CNTs 0.5 wt.% and 1.0 wt.% film under repetitive voltage of 10 V.

5.3.3 Volume resistivity

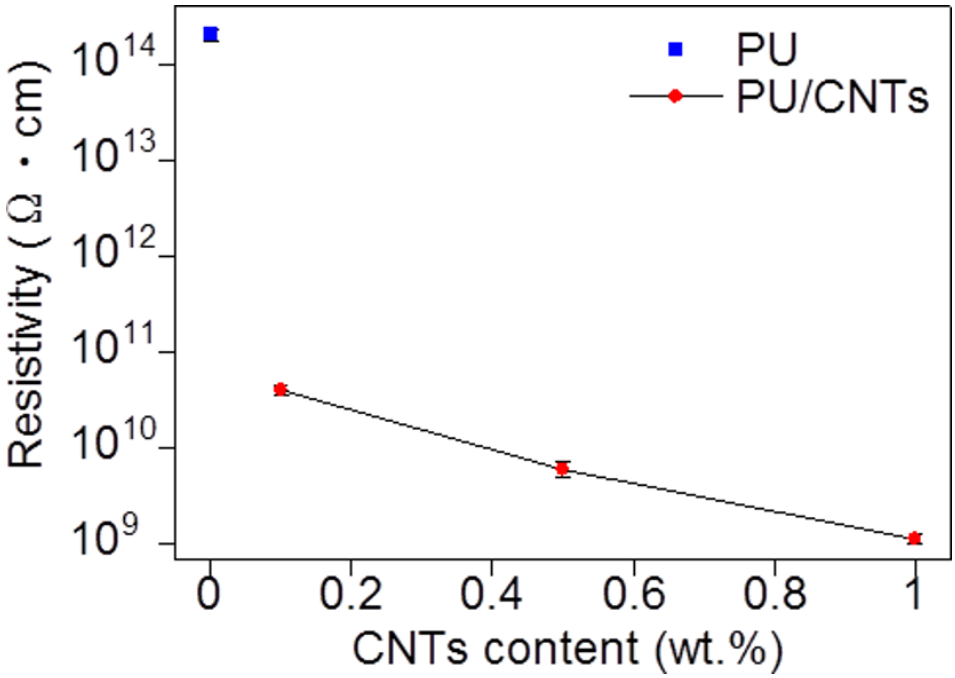

Fig. 5.9 Volume resistivity of the PU and PU/CNTs films.

Volume resistivity is the resistance to current distributed through the body or unit volume of the films. This quantifies how much a material can resist the electric current.

Volume resistivity of PU and PU/CNTs films is shown in Fig. 5.9. Volume resistivity was measured 10 times and the result is the average volume resistivity. PU/CNTs films showed a lower volume resistivity in contrast with the PU films. When CNTs, which are good conductor filler, were incorporated into the PU matrix, the volume resistivity decreased. Furthermore, with increasing of the CNTs content, volume resistivity also decreased. The lowest resistivity is 1.13×10^{9} Ω・cm (PU/CNTs 1.0 wt.%) and this confirmed that all of the films can be considered as the dielectric body.

5.3.4 Dielectric spectroscopy and impedance analysis

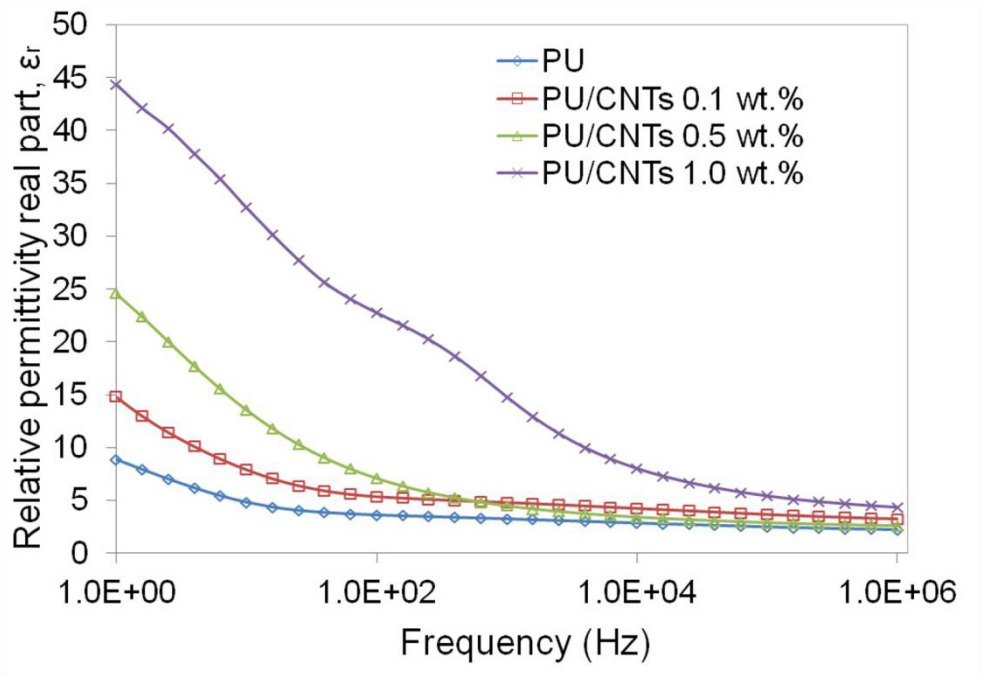

Fig. 5.10 Relative permittivity of the films in a frequency range from 1 Hz to 1 MHz.

The real part of relative permittivity is shown in Fig. 5.10. The PU/CNTs films had higher relative permittivity than the PU film and this increased as the CNTs content increased. From the permittivity, polarization behavior can be observed. From the result, we concluded that polarization is faster in the PU/CNTs films. Highly polarized samples are considered to be essential in the actuation of polymeric materials because of Maxwell pressure. Maxwell pressure can be assumed as the compressive stress in the thickness direction, which changes the width and length of the samples when voltage is applied [17, 30-32]. If the electrodes and the films are compliant, the equation for the generated Maxwell pressure is:

$$p = \varepsilon_0 \varepsilon_r E^2, \quad (5.1)$$

where ε_0 is the vacuum permittivity, ε_r is the relative permittivity, and E is the applied electric field. From this equation, a higher relative permittivity will produce a higher Maxwell pressure if the vacuum permittivity and the applied electric field are constant. The relative permittivity increased as the CNTs content increased. We thus considered that the PU/CNTs films are highly polarized and actuate because of Maxwell pressure. When voltage was applied to the films the electrostatic force from the polarized charges caused the films to contract in the thickness direction and they were found to enlarge elastically in the plane (Maxwell stress) and this assisted the bending actuation of the films.

The Cole-Cole plots of the complex impedance (real part: Z', imaginary part: Z'') for the PU and PU/CNTs films are shown in Fig. 5.11. The real part of impedance corresponds to resistance while the imaginary part corresponds to capacitance (reactance) of the materials. Furthermore, the electric and dielectric properties of the materials can be determined from the Cole-Cole plot. The Z' and Z'' become lower as the CNTs content increased and produced smaller semicircle arc. This also indicates that the resistance of the films is lower as the CNTs content increased, suggesting more conductive paths were formed [33]. The relaxation time was determined from $1/\omega_{max}$, where ω_{max} is the frequency of the maximum imaginary impedance. The relaxation time of PU/CNTs 0.1, 0.5, and 1.0 wt.% film was 6.6, 1.5, and 0.3 s, respectively. Lower relaxation time indicates the films are more conductive [34, 35] and these results are in agreement with the results of volume resistivity, as the volume resistivity decreased when the CNTs content increased. Higher conductivity was also obtained for polyaniline-clay nanocomposites and polyaniline-zinc oxide (ZnO) nanocomposites when the relaxation time was lower, as reported by Bekri-Abbes et al. [34] and Roy et al. [35], respectively. The content of ZnO nanoparticles improved the conductivity of the nanocomposites fabricated by Roy et al. [35], whereas in our case the content of CNTs enhanced the conductivity of the films. Chen et al. [15] also reported that the conductivity of their silicone/CNTs actuator showed higher conductivity as the CNTs content increased. The complex impedance was fitted with a single parallel resistor-capacitor combination and their estimated volume resistivity and estimated capacitance are as shown in Table 5.1. As the resistance is inversely proportional to the electrical conductivity and the capacitance is proportional to the dielectric constant, this

evaluation is an effective way to predict the conductivity and dielectric constant by estimating the resistance and capacitance [36]. The measured and estimated volume resistivity showed a certain degree of match. The estimated volume resistivity also decreased as the content of CNTs increased. Furthermore, from Table 5.1, the films also showed a certain amount of capacitance. From the results of estimated capacitance, we can expect that charges were stored within the films. PU/CNTs films showed higher capacitance than that of PU films and the capacitance also increased as the content of CNTs increased. Higher dielectric constant of the PU/CNTs films also can be expected as they showed higher capacitance. The permittivity results that were presented in Fig. 5.10 are in agreement with the estimated capacitance of the films, where higher capacitance suggests for higher dielectric constant. Higher dielectric constant indicates that the films have higher polarization which was believed to assist the actuation [12]. Wang et al. [33, 36] reported the dielectric properties of double-layer materials based on expanded graphite/cyanate ester (CE) layer with CNT/CE layer and polyethyl film with CNT/CE composite. From their reports related to the fitting for complex impedance using equivalent circuits, lower resistance and higher capacitance was also obtained when CNTs content increased (depends on the percolation threshold). Moreover, to clear the distribution of stored charges within the films, space charge measurement was conducted and will be discussed below.

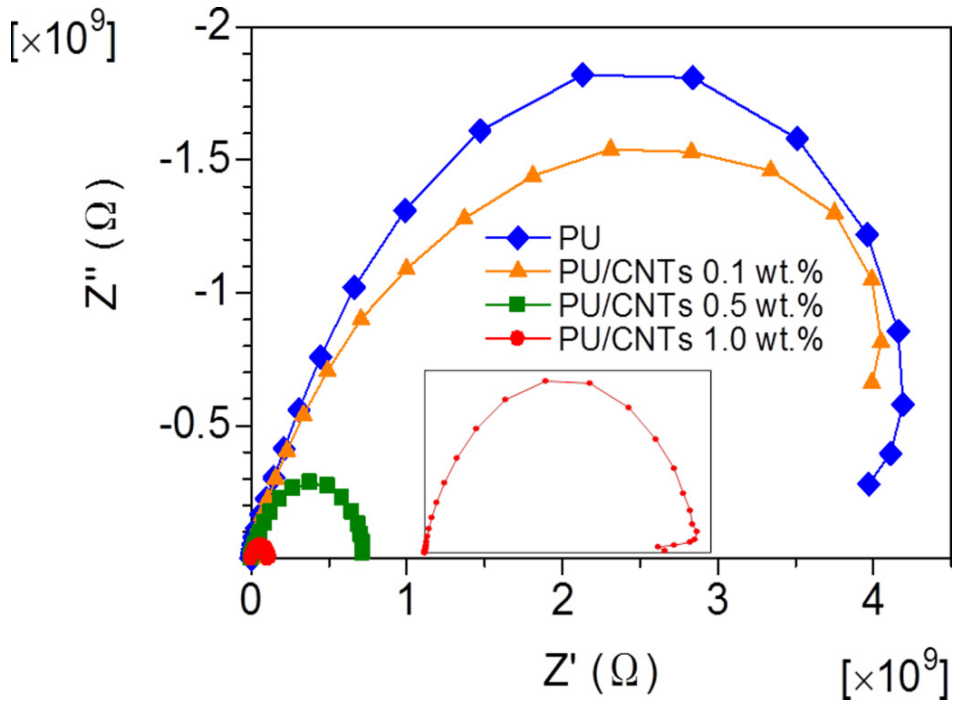

Fig. 5.11 Cole-Cole plot of the PU and PU/CNTs films, inset: PU/CNTs 1.0 wt.%.

Table 5.1 Estimated volume resistivity and estimated capacitance.

Samples	Measured resistivity (Ω・cm)	Estimated resistivity (Ω・cm)	Estimated capacitance (pF)
PU	2.04×10^{14}	3.42×10^{11}	149.27
PU/CNTs 0.1 wt.%	4.03×10^{11}	3.27×10^{11}	203.66
PU/CNTs 0.5 wt.%	6.00×10^{10}	5.90×10^{10}	319.66
PU/CNTs 1.0 wt.%	1.13×10^{9}	9.24×10^{9}	389.89

5.3.5 Charge distribution behavior

To examine the actuation mechanism further, space charge measurement was conducted. Space charge distribution of the PU and PU/CNTs films upon the application of 1000 V is shown in Fig. 5.12. Interestingly, the charge distribution behavior within the films was asymmetric. The first peak appeared is the anode side, followed by accumulated charge within the films, and lastly is the cathode side. The accumulation of negative charge can be observed next to the anode side for all the samples. No accumulated charge was observed next to the cathode side for the PU/CNTs films, but accumulation of positive charge was observed next to the cathode side for the PU films. The accumulated charge density near the anode side becomes higher as the contents of CNTs increased and the PU/CNTs 1.0 wt.% films showed the highest among the samples. The relationship between accumulated charge density with various voltages is illustrated in Fig. 5.13. The accumulated charge density is dependent on the applied voltage as it increased upon application of higher voltage. The PU/CNTs films showed higher accumulated charge density than PU films. The PU/CNTs 1.0 wt.% films gave the highest accumulated charge density in the range of 100-1000 V compared to the other films. The asymmetric and charge accumulation phenomenon were also observed for PU-based films and PVC gels, as reported by Watanabe et al. [14, 22] and Ali et al. [20], respectively. From their studies, the charge accumulation was believed to contribute to the bending deformation and explained the actuation behavior. Furthermore, Wang et al. [36] also reported that the accumulation of the charges led to the increased dielectric constant, which is favorable for the actuation [12]. We thus considered that the space charge measurement is an effective method to investigate the charge distribution behavior and the actuation mechanism of the films.

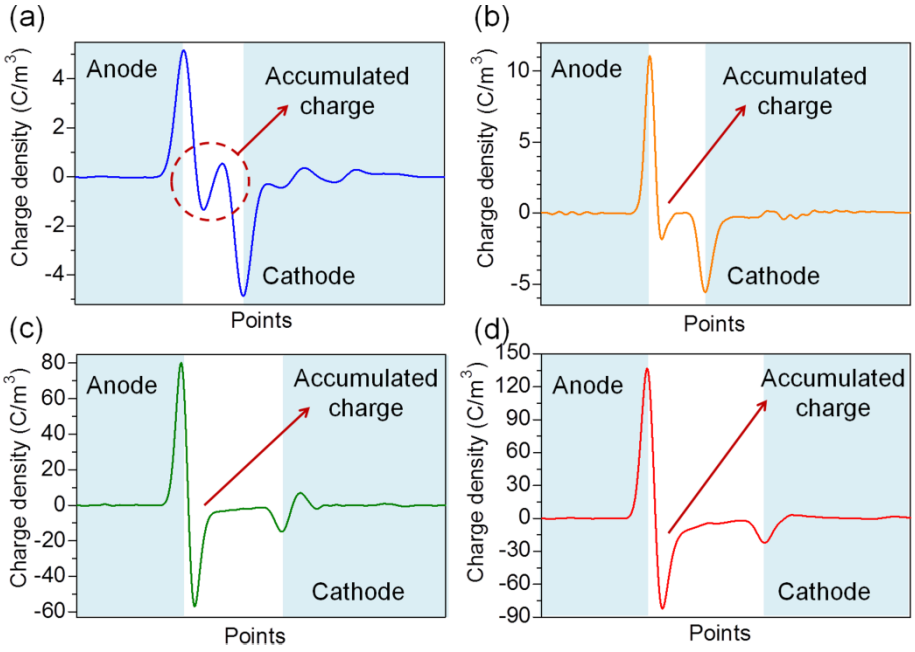

Fig. 5.12 Charge distribution behavior of (a) PU, (b) PU/CNTs 0.1 wt.%, (c) PU/CNTs 0.5 wt.%, and (d) PU/CNTs 1.0 wt.% film.

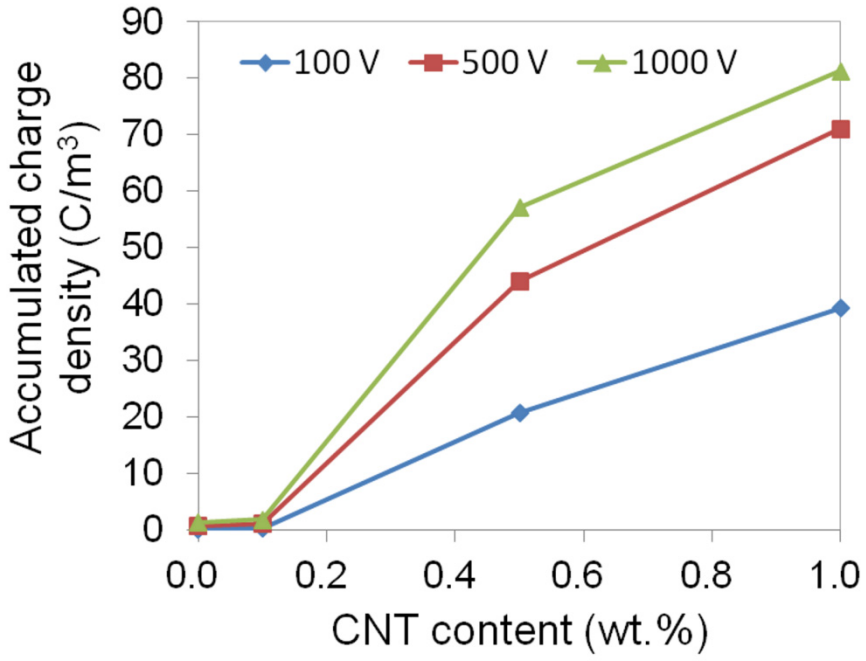

Fig. 5.13 Relationship between accumulated charge density with various voltages.

Illustration of the electric conduction in an insulator or in dielectric polymers under an electric field application is as shown in Fig. 5.14(a) [37]. The injection current (I_i) and the bulk conduction current (I_c) play a role in balancing the charge distribution

within the polymers upon electrical conduction. Higher current is suppressed and lower current is thus promoted. When $I_i < I_c$ the injection current from the anode is strengthened and negative charges accumulate near the anode. The charge distribution of the films (Fig. 5.12) is asymmetric and can be explained by the accumulated space charge phenomenon.

For all of the samples, asymmetric charge distribution, where negative charge accumulated near the anode side, can be observed. The asymmetric charge distribution causes asymmetric strains within the films as illustrated in the model of bending deformation in Fig. 5.14 (b). In the thickness direction of the films, we can assume that there is phase separation between high and low charge density area. The anode side can be considered as the high-actuation ability area because the charge is accumulated there and meanwhile the cathode side as the low-actuation ability area. Negative charge accumulation causes contraction in the direction of the thickness near the anode [12]. Additionally, the contraction results in an expansion of the anode plane as the films maintain a constant volume [12]. Asymmetric strain, i.e., the strain near the anode, causes the films to bend toward the cathode. From the bending deformation, the results are also in agreement, which shows that the films bend toward the cathode when voltage is applied. We considered that the asymmetric strain that causes contraction and expansion of the films assisted the actuation and the bending direction toward cathode side. Overall, we considered that Maxwell pressure and the asymmetric strain causes contraction and expansion of the films which assisted the actuation and the bending direction toward cathode.

Although charge accumulation was observed both near the anode and cathode side for the PU films, the charge density of the accumulated charge near the anode side is relatively higher than the cathode side. Thus, the actuation ability is higher at the anode side rather than the cathode side and they also showed bending deformation toward the cathode. However, the charge accumulated near the cathode side might be the reason for small deformation of the PU films because certain amount of strain might be produced at the cathode side. For the samples with higher accumulated charge density as observed in the PU/CNTs films, higher strain (contraction and expansion) that leads to higher bending deformation can be expected.

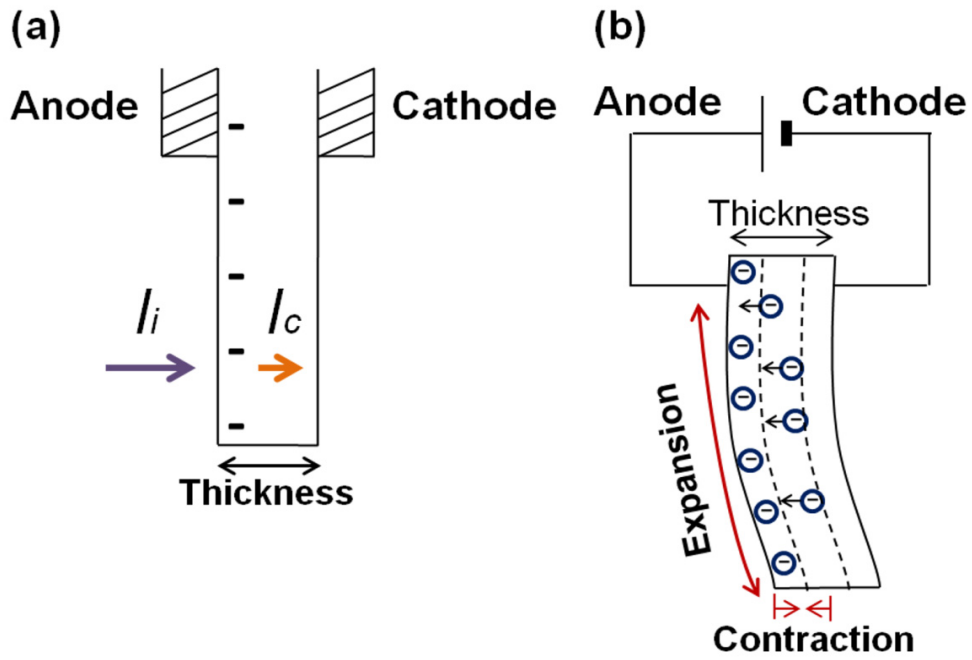

Fig. 5.14 Mechanism (a) electric conduction in the polymer (b) model of bending actuation mechanism.

5.4 Conclusions

A polymer-based electroactive nanocomposite was fabricated using PU and microwave-induced polymerization treated CNTs as the filler. The modified CNTs were found to be highly dispersed in a polar solvent and PU matrix. They contained more carboxyl and hydroxyl groups and showed less aggregation compared with pristine CNTs. The films showed bending deformation toward the cathode when voltage was applied and reverted close to their original position when voltage was removed. The application of 1000 V to the PU/CNTs 0.5 wt.% film gave bending displacement of about 0.3 mm. The application of 1000 V to the C-PU/CNTs 0.1 wt.% film gave the highest bending displacement of about 3.0 mm. However, even upon the application of a lower voltage, we found that the films can show good bending deformation (C-PU/CNTs 1.0 wt.%) as the CNTs content increased. The films also showed a stable bending displacement upon repetitive voltage cycle. The films also showed similar bending displacement upon voltage cycling and this is considered to be a type of memory. Maxwell pressure and the charge accumulation phenomenon cause contraction and expansion in the direction of the thickness of the films that triggered bending actuation in the films. This helped us to understand the actuation mechanism and bending deformation direction of this kind of electroactive nanocomposite material.

References

[1] M. Haghayegh, G. M. M. Sadeghi, Polym. Compos. 33 (2012) 843-849.

[2] D. Ratna, J Karger-Kocsis, J. Mater. Sci. 43 (2008) 254-269.

[3] Y. Liu, H. Lv, X. Lan, J. Leng, S. Du, Compos. Sci. Technol. 69 (2009) 2064-2068.

[4] C. Liu, H. Qin, P. T. Mather, J. Mater. Chem. 17 (2007) 1543-1558.

[5] J. Ding, Y. Zhu, Y. Fu, Polym. Compos. 35 (2014) 412-417.

[6] T. Ohki, Q. Q. Ni, N. Ohsako, M. Iwamoto, Composites Part A 35 (2004) 1065-1073.

[7] C. S. Zhang, Q. Q. Ni, Compos. Struct. 78 (2007) 153-161.

[8] B. Xu, Y. Q. Fu, M. Ahmad, J. K. Luo, W. M. Huang, A. Kraft, R. Reuben, Y. T. Pei, Z. G. Chen, J. Th. M. De Hosson, J. Mater. Chem. 20 (2010) 3442-3448.

[9] N. G. Sahoo, Y. C. Jung, N. S. Goo, J. W. Cho, Macromol. Mater. Eng. 290 (2005) 1049-1055.

[10] N. G. Sahoo, Y. C. Jung, H. J. Yoo, J. W. Cho, Compos. Sci. Technol. 67 (2007) 1920-1929.

[11] R. Shankar, T. K. Ghosh, R. J. Spontak, Soft Matter 3 (2007) 1116-1129.

[12] G. J. H. Melvin, Q. Q. Ni, T. Natsuki, Appl. Phys. A 117 (2014) 2043-2050.

[13] N. J. Jo, D. H. Lim, G. M. Bark, H. H. Chun, I. W. Lee, H. Park, J. Mater. Sci. Technol. 26 (2010) 763-768.

[14] M. Watanabe, N. Wakimoto, H. Shirai, T. Hirai, J. Appl. Phys. 94 (2003) 2494-2497.

[15] L. Z. Chen, C. H. Liu, C. H. Hu, S. S. Fan, Appl. Phys. Lett. 92 (2008) 263104.

[16] K. Y. Cho, H. G. Lim, S. R. Yun, J. Kim, K. S. Kang, J. Phys. Chem. C 112 (2008) 7001-7004.

[17] X. Zhang, C. Löwe, M. Wissler, B. Jähne, G. Kovacs, Adv. Eng. Mater. 7 (2005) 361-367.

[18] Z. Cai, J. Kim, J. Appl. Polym. Sci. 115 (2010) 2044-2049.

[19] L. Chen, C. Liu, K. Liu, C. Meng, C. Hu, J. Wang, S. Fan, ACS Nano 5 (2011) 1588-1593.

[20] M. Ali, T. Hirai, J. Mater. Sci. 46 (2011) 7681-7688.

[21] M. Ali, T. Hirai, J. Mater. Sci. 47 (2012) 3777-3783.

[22] M. Watanabe, Polym. Int. 56 (2007) 1265-1271.

[23] H. Kalita, N. Karak, Polym. Compos. 35 (2014) 636-643.

[24] L. Zhou, S. Fang, J. Tang, L. Gao, J. Yang, Polym. Compos. 33 (2012) 1866-1873.

[25] Y. L. Hsin, J. Y. Lai, K. C. Hwang, S. C. Lo, F. R. Chen, J. J. Kai, Carbon 44 (2006) 3328-3335.

[26] L. Zhang, Q. Q. Ni, A. Shiga, T. Natsuki, Y. Fu, Polym. Eng. Sci. 51 (2011) 1525-1532.

[27] O. Breuer, U. Sundararaj, Polym. Compos. 25 (2004) 630-645.

[28] Y. Nakama, J. Kyokane, K. Tokugi, T. Ueda, K. Yoshino, Synth. Met. 135-136 (2003) 749-750.

[29] L. V. Karabanova, R. L. D. Whitby, A. Korobeinyk, O. Bondaruk, J. P. Salvage, A. W. Lloyd, S. V. Mikhalovsky, Compos. Sci. Technol. 72 (2012) 865-872.

[30] G. Kofod, R. Kornbluh, R. Pelrine, P. Sommer-Larsen, J. Intell. Mater. Syst. Struct. 14 (2003) 787-793.

[31] R.E. Pelrine, R.D. Kornbluh, J.P. Joseph, Sens. Actuators, A 64 (1998), 77-85.

[32] L. Petit, B. Guiffard, L. Seveyrat, D. Guyomar, Sens. Actuators, A 148 (2008), 105-110.

[33] B. Wang, G. Liang, Y. Jiao, A. Gu, L. Liu, L. Yuan, W. Zhang, Carbon 54 (2013) 224-233.

[34] I. Bekri-Abbes, E. Srasra, React. Funct. Polym. 70 (2010) 11-18.

[35] A. Roy, A. Parveen, R. Deshpande, R. Bhat, A. Koppalkar, J. Nanopart. Res. 15 (2013) 1337.

[36] B. Wang, Y. Jiao, A. Gu, G. Liang, L. Yuan, Compos. Sci. Technol. 91 (2014) 8-15.

[37] K. Yoshino, Y. Inuishi, Oyo Buturi 49 (1980) 212-227.

Chapter 6

****

EAP actuator incorporated with mild hydrothermally treated CNTs

****

6 EAP actuator incorporated with mild hydrothermally treated CNTs

6.1 Introduction

In recent years, there has been intensive investigation of polymers that respond to electrical stimulation that can be applied for actuator materials, sensors, artificial muscles, smart devices, and micro-switches [1-9]. An electric field-stimulated polymer-based actuators are referred to as electroactive polymers (EAPs) [2, 3, 7, 9, 10]. EAPs have the advantages, such as light weight, flexible, tolerance against fracture, and easy to fabricate, and they can convert electrical energy to mechanical energy and thus impart a force and produce large strain [2, 3, 6-13]. EAPs can be divided into two types based on their actuation mechanism, which is electronic EAPs (dry) and ionic EAPs (wet) [3, 8-12]. Electronic EAPs actuate because of forces from the shift or motion of electrical charge, while most of ionic EAPs function in an electrochemical system and require liquid electrolytes for ion transport [3, 8-12]. Ionic EAPs are inconvenient for practical application as most of them required a liquid medium to maintain their wetness, and a high-standard safety encapsulation is required for the liquid electrolyte [3, 8, 12]. Thus, we focused on electronic EAPs as they can function in a dry environment and are appropriate for practical applications.

Polymers are generally good electrical insulators, and upon combining a polymer with an electric conductor as a filler, new and unique polymer-based composites can be fabricated. Jo et al. [10], Watanabe et al. [7, 14], and Nakama et al. [15] investigated the bending electrostriction of polyurethane (PU)-based films. The bending deformation of PU-based films under the application of an electric field was measured, and the mechanism was briefly discussed in their reports. Discussions and reports about the bending deformation mechanism of PU-based nanocomposite actuators are limited. PU are insulators, and they are generally light, soft, flexible and easy to fabricate, and have been reported to generate deformation and large strain under electric field stimulation [3, 7, 10, 14]. Conversely, carbon nanotubes (CNTs) are also light, possess a high aspect ratio, and have outstanding mechanical, chemical, and electric properties [3, 6, 8, 16-20]. CNTs can improve the mechanical and electrical properties of polymer-based

composites and are thus a good candidate for use as a filler in actuators.

However, CNTs disperse poorly in organic and aqueous solvents because of a strong intrinsic van der Waals attraction [18-20]. Sahoo et al. [21] investigated the influence of CNTs in a PU nanocomposites actuator. To improve the dispersion of CNTs, they conducted strong acid treatment. In contrast, a mild hydrothermal treatment that is environment friendly, fast, and allows for easy modification has been performed [20]. No harsh organic or aqueous solvents were used in this process, and it is thus a less destructive modification route. This treatment leads to the introduction of carboxyl and hydroxyl groups to the surface of the CNTs, which allows them to be highly dispersed in polar solvents.

In this chapter, we combined the PU and mild hydrothermally treated CNTs to produce a polymer-based composite actuator. The objective was to evaluate the film and its electrical properties for the development of polymer-based electroactive actuators and to understand the mechanism of actuation when an electric field is applied.

6.2 Materials and methods

6.2.1 Mild hydrothermal treatment

Multi-walled CNTs (Wako Pure Chemical Industries Ltd., Japan, d = 20-30 nm) were used as the filler. Two types of mild hydrothermal treatment were conducted, as reported by our research group in Ref. [20], with some modifications. Pure water, potassium hydroxide (KOH), and potassium persulfate (KPS) were used in the treatment, and they were also obtained from Wako Pure Chemical Industries Ltd., Japan.

For the type 1, CNTs were added to the aqueous solution of KOH and ultrasonically mixed in a stainless steel reaction autoclave with a polytetrafluoroethylene liner. For the type 2 treatment, both KOH and KPS were used. First, CNTs were ultrasonically mixed in the aqueous solution of KOH, similar process as the type 1. Then, KPS was added to the solution of KOH and further ultrasonically mixed as a next step. The autoclave was then sealed and heated at 160°C for 2 h.

Finally, the solutions were filtered and rinsed with pure water and ethanol for several times. The products were dried overnight in vacuum at 30°C. Type 1 and type 2 mild hydrothermally treated CNTs were denoted as KOH and KPS, respectively.

6.2.2 Fabrication process

The modified CNTs and N,N-dimethylformamide (DMF, Wako Pure Chemical Industries Ltd., Japan) were ultrasonically mixed for 10 min. The solution was then added to PU (DiARY MS-4510, Diaplex) and mixed at 8000 rpm for 5 min using a high-speed homogenizer. After this mixing, the mixture was degassed. The mixture was then applied to the glass plate of an auto film applicator and dried at 50°C for 8 h using a heat gun.

The fabricated samples are PU films, PU/CNTs films combined with type 1 mild hydrothermally treated CNTs (KOH 0.1, 0.5, 1.0 wt.%), and PU/CNTs films combined with type 2 mild hydrothermal treated CNTs (KPS 0.1, 0.5, 1.0 wt.%). The thickness of the films was 0.1 mm. Each film was coated with thin silver coating for the evaluation of actuator performance.

6.2.3 Evaluation method

The dispersion of the pristine CNTs (0.01 g) and mild hydrothermal treated CNTs (0.01 g) in a polar solvent (DMF, 10 ml) after mixing and after 1 week was evaluated. Transmission electron microscopy (TEM) images of the pristine CNTs and mild hydrothermal treated CNTs were obtained using a TEM (JEM-2100, JOEL, Japan) with an accelerating voltage of 200 kV. The cross-sectional morphology of the films incorporated with mild hydrothermally treated CNTs was observed using field emission scanning electron microscopy (FE-SEM, Hitachi S-5000, 20 kV). The films were fractured in liquid nitrogen, and the cross-sectional surfaces were coated with thin platinum-palladium coating for FE-SEM observation. The pristine CNTs and mild hydrothermally treated CNTs were also evaluated using X-ray photoelectron spectrometry (XPS, Kratos Axis Ultra DLD) with a standard Mg Kα (1256.6 eV) X-ray source operating at 10 mA and 15 kV.

Actuator performance was evaluated by measuring the bending displacement of the films using a laser displacement meter (Keyence LK-G3000V), a controller (Keyence LK-GD500), and a high-voltage power supply (Matsusada Precision, HJPQ-30P1). The films were cut into 5 × 35 mm rectangles, vertically suspended in air, and sandwiched between the electrodes. Upon the application of DC voltage, silver-coated film's bending displacement was measured at room temperature.

The permittivity of the film was measured using an impedance analyzer and a dielectric interface (Solartron Analytical Co.). The films were analyzed using an applied

voltage of 100 mV and sweep frequencies from 1 Hz to 1 MHz at room temperature. Circular samples with a diameter of 12 mm (larger than the electrodes diameter) and a thickness of 0.1 mm were used and placed between the parallel plate electrodes for measurement.

To determine the charge distribution in the thickness direction of the films, space charge measurement was conducted. The space charge measurement was obtained using a pulsed electroacoustic non-destructive test system (Five Lab, PEANUTS). When a pulsed voltage is applied to the films, they deform instantaneously and produce an elastic wave within the films (thickness direction). If charge exists within the films, the Coulomb force of the charge will produce an elastic wave. This signal (elastic wave) will be detected by a piezoelectric sensor and will be observed as amplitude that depends on the amount of charge. The pulsed voltage and applied voltage are both 100 V at room temperature. Circular samples with a diameter of 12 mm (larger than the sensor diameter) and a thickness of 0.1 mm were used and placed between the sensor electrodes under normal pressure for measurements.

6.3 Results and discussion

6.3.1 Evaluation of mild hydrothermally treated CNTs

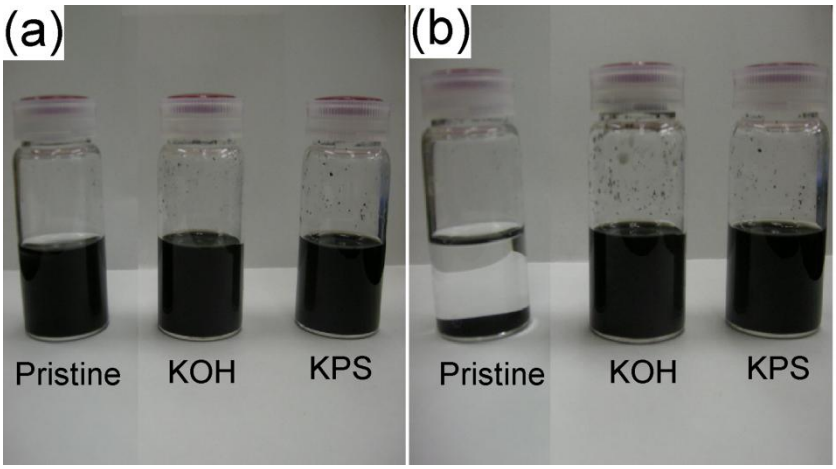

Fig. 6.1 Dispersion of the CNTs in a polar solvent (a) after mixing and (b) after 1 week.

The dispersion of modified CNTs in the DMF improved compared with pristine CNTs, as shown in Fig. 6.1(a) and (b). After mixing, all the CNTs dispersed well in DMF (Fig. 6.1(a)). However, after 1 week (Fig. 6.1(b)), the pristine CNTs precipitated, while the modified CNTs were uniformly dispersed in DMF. For the mild

hydrothermally treated CNTs, oxygen functional groups were introduced to the surface of the CNTs and this led to uniform dispersion in the polar solvent (DMF).

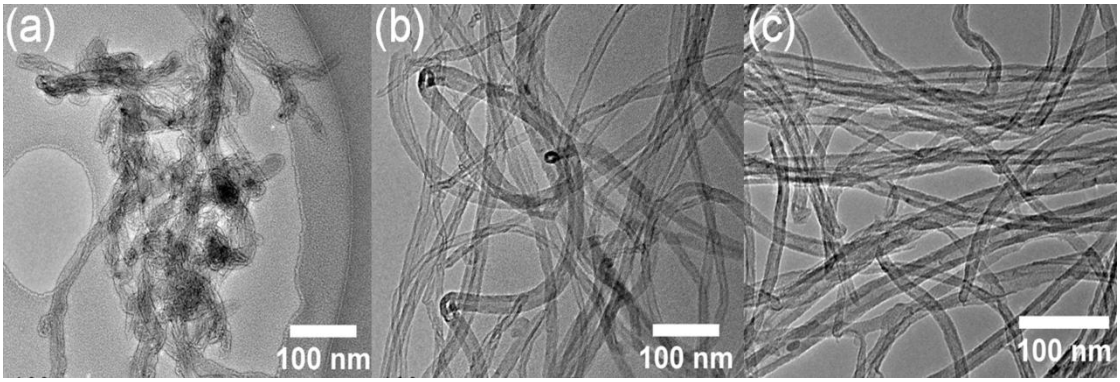

Fig. 6.2 TEM images of pristine CNTs and mild hydrothermally treated CNTs (a) pristine CNTs, (b) KOH, and (c) KPS.

TEM images of the pristine CNTs and mild hydrothermally treated CNTs are depicted in Fig. 6.2. From Fig. 6.2(a), the pristine CNTs showed some aggregation between the CNTs. From Fig. 6.2(b) and (c), both mild hydrothermally treated CNTs showed less aggregation between the CNTs and better dispersion compared with the pristine CNTs. Mild hydrothermal treatment thus improves the dispersion of pristine CNTs.

Cross-sectional images of the pristine CNTs, KOH, and KPS 1.0 wt% film are shown in Fig. 6.3. Pristine CNTs film showed a certain degree of aggregation between the CNTs when incorporated into PU compared to KOH and KPS films. Both treated CNTs showed uniform distribution and no aggregation in the PU matrix. The good dispersion of CNTs is due to that the modification of CNTs enhanced the interaction between the CNTs and PU. The mild hydrothermal treatment increased the carboxyl and hydroxyl functional groups of CNTs, and this led to well-dispersed KOH and KPS 1.0 wt% film. The introduction of functional groups to the CNTs allows covalent bonding of PU directly to the nanotube framework and significantly improving the interface between the PU and the treated CNTs [19]. The carboxyl and hydroxyl groups of treated CNTs will be discussed in the XPS result below.

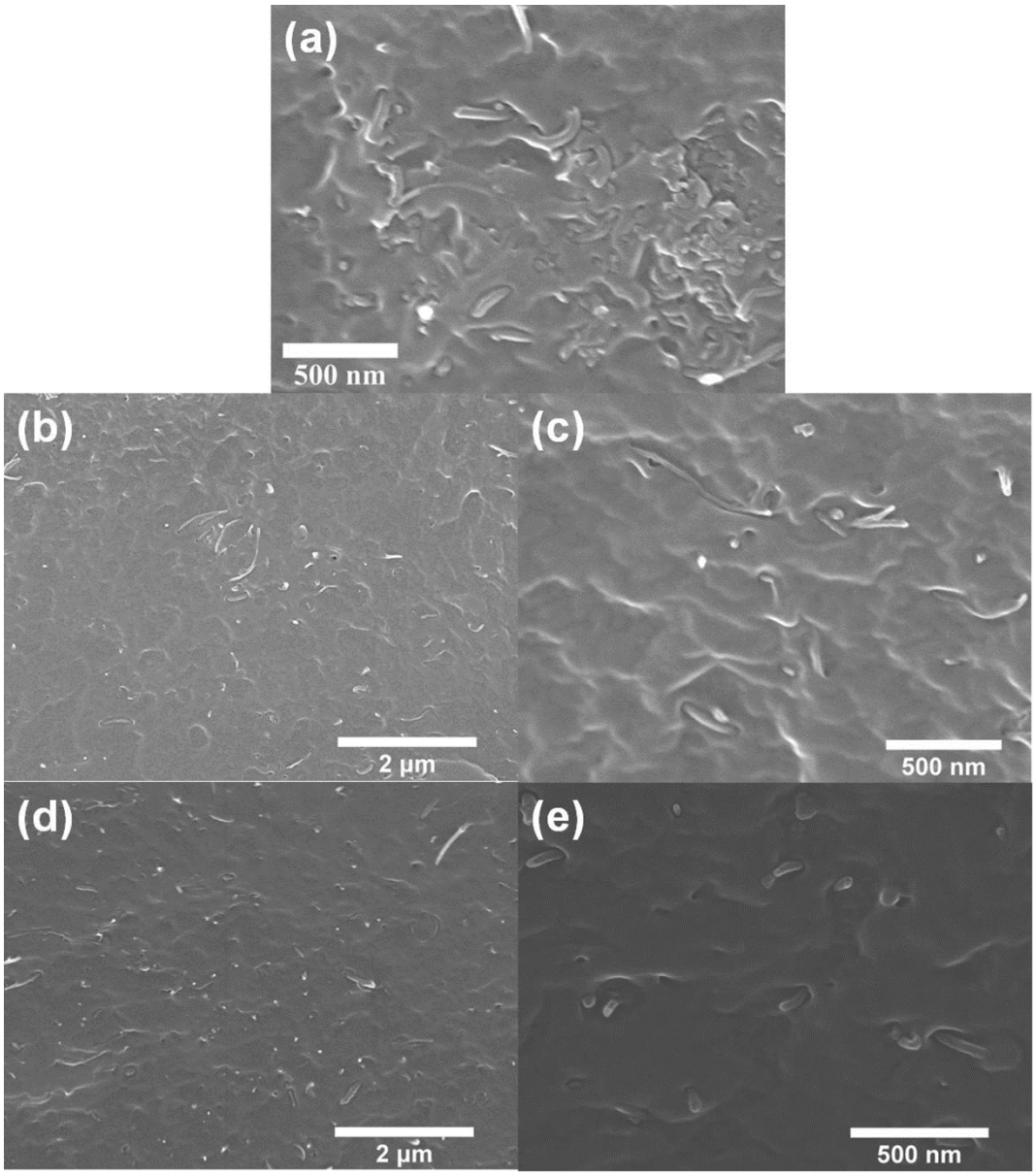

Fig. 6.3 FE-SEM cross section images of films incorporated with (a) pristine CNTs, (b) and (c) KOH, (d) and (e) KPS.

To investigate the oxygen functional groups (carboxyl and hydroxyl groups) of the modified CNTs, an XPS evaluation was carried out. The XPS spectra are shown in Fig. 6.4. Type 1 (KOH only) and type 2 (KOH and KPS) mild hydrothermally treated CNTs showed a higher intensity oxygen (O 1 s) peak compared with the pristine CNTs. The atomic percentage ratios for the pristine CNTs are 98.51% for C 1 s and 1.49% for O 1 s. KOH gave 97.92% for C 1 s and 2.08% for O 1 s, while KPS gave 92.75% for C 1 s and 7.25% for O 1 s. The higher O 1 s peak confirmed that many oxygen functional groups were attached to the surface of these CNTs. These oxygen functional groups are the reason for the mild hydrothermally treated CNTs dispersing uniformly in the polar

solvent and PU matrix. From the XPS result, we also conclude that this treatment was successful as carboxyl and hydroxyl groups were introduced to the surface of the CNTs.

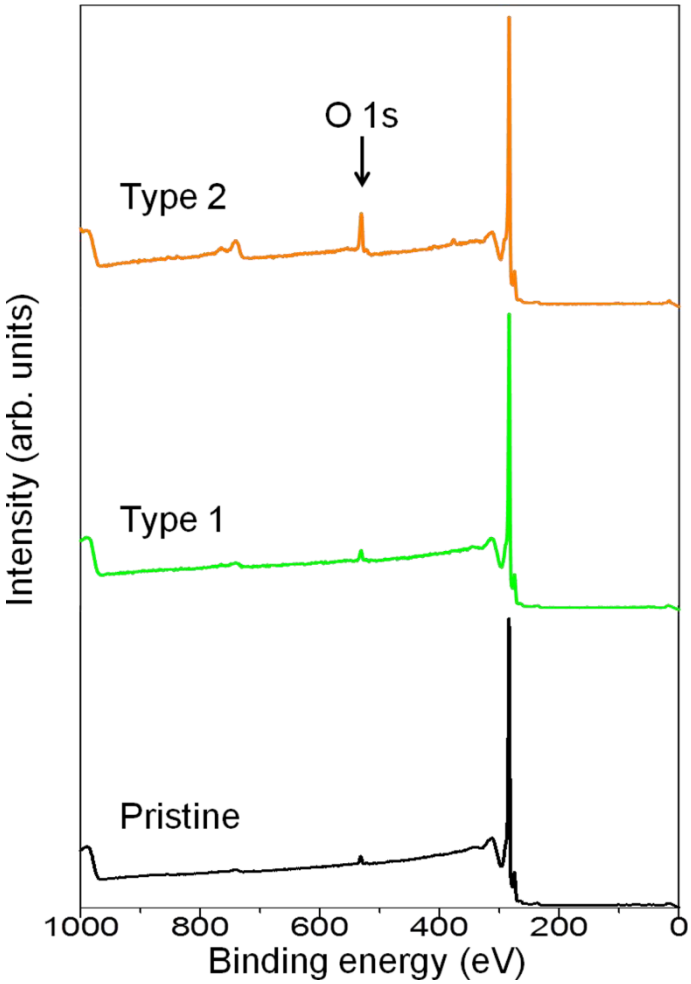

Fig. 6.4 XPS spectra of pristine CNTs and mild hydrothermally treated CNTs.

6.3.2 Bending displacement

The films bent when DC voltage was applied, and the bending displacement was measured. The bending displacement of the films is shown in Fig. 6.5(a). The voltage applied to each film was varied (Fig. 6.5(a)) because high voltage will damage some films, i.e., burnt holes caused by overheating in the area sandwiched between the electrodes. Even with the application of a lower voltage, the bending displacement increased as the CNTs content increased. This shows that low-energy consumption is adequate for higher CNTs content films, and they are more efficient at energy conversion. The bending actuation of KOH 1.0 wt.% upon the application of 10 V is shown in Fig. 6.5(c) and (d). The film showed bending displacement toward the cathode and shifted from its original position when 10 V was applied. The highest bending

displacement was obtained for the KOH 1.0 wt.% film upon the application of 10 V. Its average bending displacement was found to be about 5.0 mm. The PU/CNTs films gave a higher bending displacement compared with the PU films, and the KOH films had better actuation properties compared with the PU and KPS films.

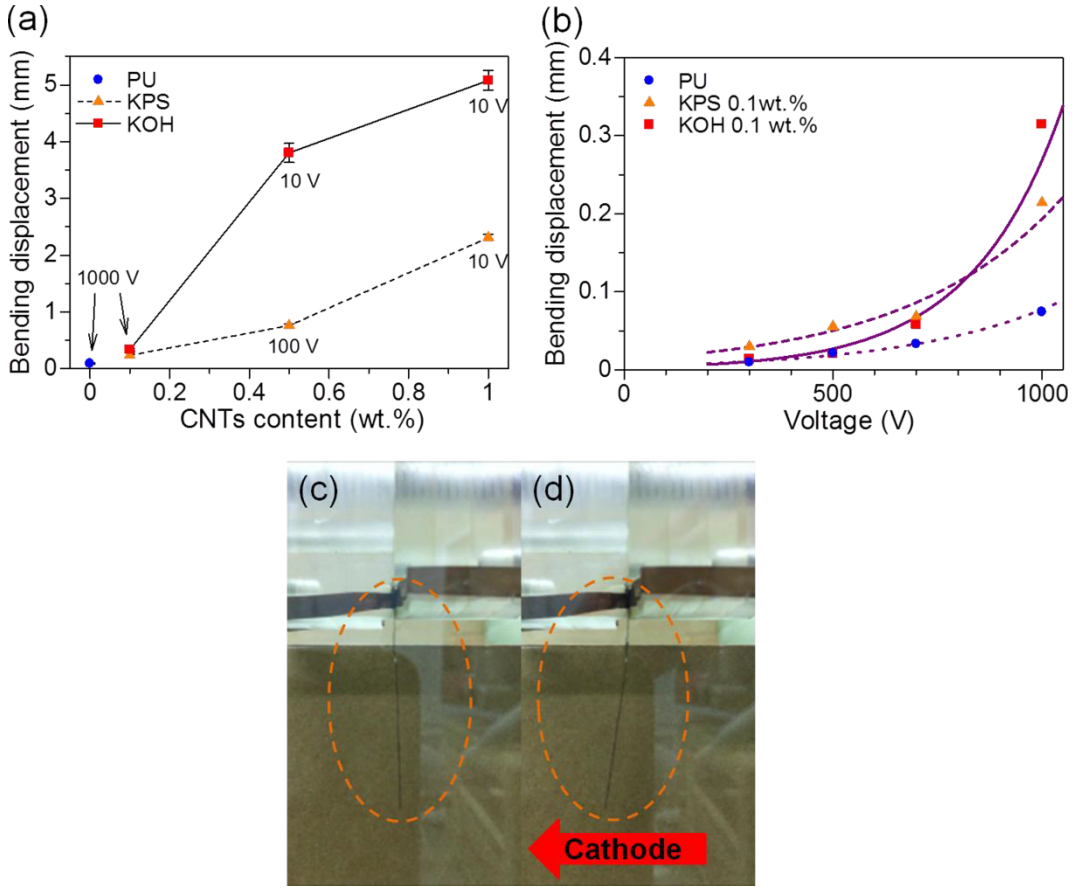

Fig. 6.5 Actuator performance: (a) bending displacement of the films with various applied voltages, (b) relationship between voltage and bending displacement, (c) voltage off KOH 1.0 wt.%, and (d) voltage on (10 V) KOH 1.0 wt.%.

The relationship between voltage and actuation of PU and PU/CNTs films 0.1 wt.% is plotted in Fig. 6.5(b). No significant actuation was observed in the films for an applied voltage less than 300 V, but the bending displacement increased as the applied voltage increased beyond 300 V. This showed that the films are dependent on the applied voltage, and this greatly affected the actuation even though the applied voltage for the higher content CNTs films (Fig. 6.5(a)) was lower.

To evaluate the films as part of a practical actuator, it is important to evaluate them under voltage cycling conditions. A repeat voltage of 10 V was applied to the films, and

the bending displacement was measured as shown in Fig. 6.6. Each cycle is about 65 s, and the films showed maximum bending displacement over the cycle. The films thus gave a fast response to bending actuation upon voltage cycling. The films bent toward the cathode when the voltage was applied and reverted close to the original position when the voltage was removed. The films are considered to be an elastic body, and they showed elastic recovery when the voltage was removed. The bending displacement (creep behavior) of each film is similar in each voltage cycle. This creep behavior phenomenon can be considered to be a type of memory where the electric field reminds the films of the electrically memorized strain [3, 4]. Furthermore, this also proves that the actuation of the films is reproducible and stable upon voltage cycling.

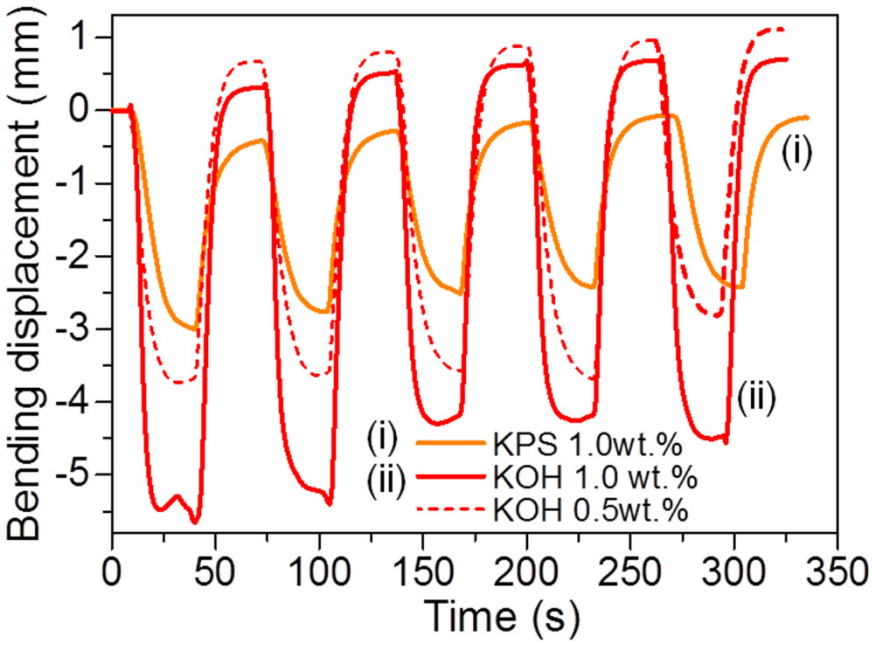

Fig. 6.6 Actuator behavior of the films under 10 V repetitive voltage cycle.

6.3.3 Dielectric spectroscopy

The restored energy and polarization behavior can be characterized by the relative permittivity (dielectric constant), as shown in Fig. 6.7. The PU/CNTs films had higher permittivity than the PU film, and this increased as the CNTs content increased, as shown by the KPS films. At lower frequency, the charges within the film move slowly toward the electrodes and thus, the permittivity is higher. Conversely, at higher frequency, the electric field changes faster and the times are shorter leading to lower

permittivity. Therefore, polarization is faster in the KPS films and slower in the KOH and PU films. The KPS and KOH films have a better polarization property than the PU films, which assists the actuation behavior of the film.

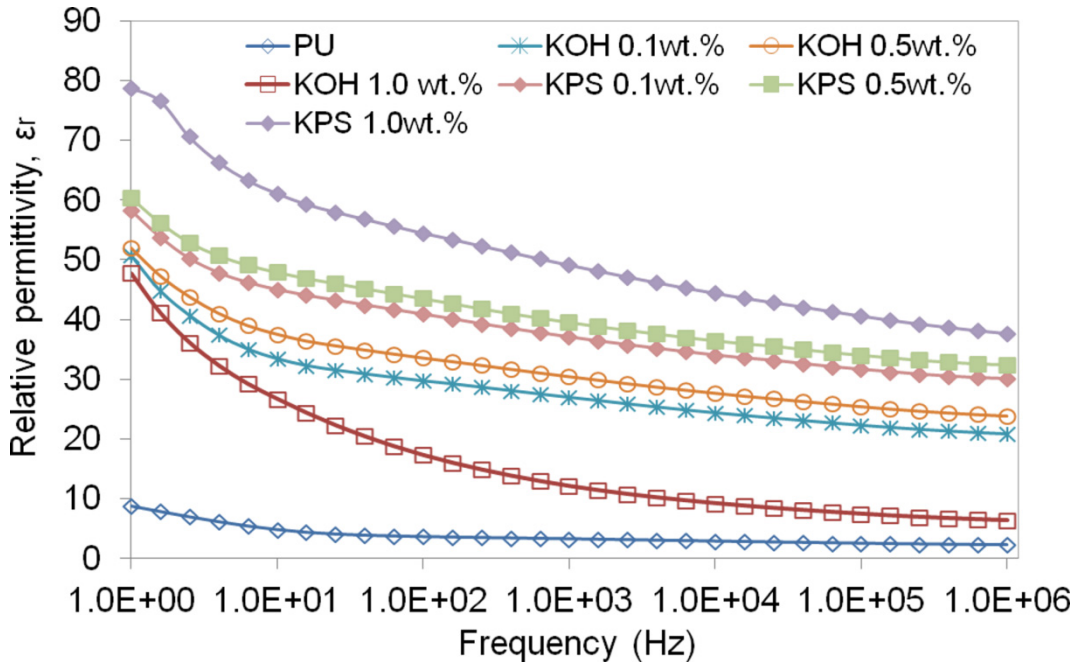

Fig. 6.7 Relative permittivity of the films in a frequency range from 1 Hz to 1 MHz.

Highly polarized dielectric films are considered to be important in the actuation of polymer-based materials because of Maxwell pressure [1-3, 11, 22-24]. Maxwell pressure is a compressive stress in the thickness direction, which changes the length and width of the samples when voltage is applied [1-3, 11, 22-24]. The equation for the generated Maxwell pressure is:

$$p = \varepsilon_0 \varepsilon_r E^2, \tag{6.1}$$

where ε_0 is the vacuum permittivity, ε_r is the relative permittivity, and E is the applied electric field. From this equation, a higher relative permittivity will produce a higher Maxwell pressure if the vacuum permittivity and the applied electric field are constant. With an increase in the CNTs content for the KPS films, the relative permittivity also increased. We thus considered that the KPS films are highly polarized and actuate because of Maxwell pressure. Furthermore, the KPS films also gave the highest relative permittivity in contrast to the other films and this assisted the actuation behavior of the films. When voltage was applied to the films, the electrostatic force from the polarized

charges caused the films to contract in the thickness direction and they were found to enlarge elastically in the plane (Maxwell stress) and this is considered to be the cause of bending actuation in the films [3, 11, 22, 24].

In contrast to the KPS films, the KOH films did not show an increase in relative permittivity with an increase in CNTs content. We thus assume that another factor is responsible for their actuation. To investigate the mechanism, we obtained space charge measurements to determine the charge distribution when a voltage is applied and this will be discussed in the next section.

6.3.4 Space charge behavior

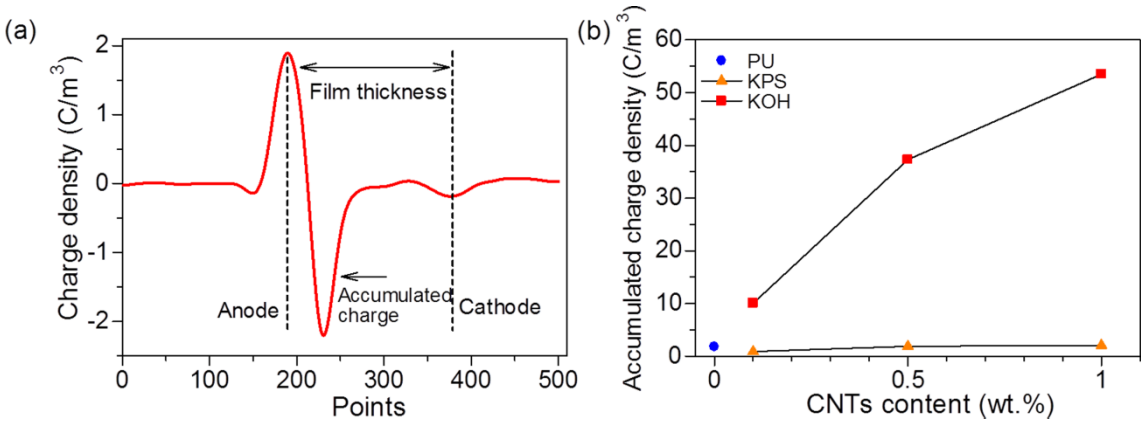

Fig. 6.8 Space charge measurements (a) space charge distribution of KOH 0.5 wt.% film at 100 V and (b) accumulated charge density of the fabricated films at 100 V.

An example of the space charge distribution upon the application of 100 V to KOH 0.5 wt.% is shown in Fig. 6.8(a). The first peak is the anode peak, the second peak is the accumulated charge peak, and the third peak is the cathode peak. The film's thickness is also shown in this figure. The accumulated charge peak is present next to the anode peak, and negative charges accumulated near the anode.

We calculated the area of the accumulated charge peak (as a triangle), and the accumulated charge density that was calculated is shown in Fig. 6.8(b). The KOH films gave the highest accumulated charge density in contrast to the other films. The PU and KPS films gave a relatively lower accumulated charge density compared with the KOH films. Even though the accumulated charge density of the KPS films increased as the CNTs content increased, they only showed a slight increase and the charge density was thus practically unchanged.

Electric conduction in an insulator or in dielectric polymers under a high electric field application can be either bulk- or electrode-limited [3, 7, 14, 25]. An illustration of each case is shown in Fig. 6.9(a) and (b). The injection current (I_i) and the bulk conduction current (I_c) play a role in balancing the charge distribution within the polymers upon electrical conduction. Higher current is suppressed and lower current is thus promoted. When $I_i > I_c$ the injection current from the anode is suppressed and positive charges accumulate near the anode (bulk-limited case). However, when $I_i < I_c$ the injection current from the anode is strengthened and negative charges accumulate near the anode (electrode-limited case). As shown in Fig. 6.8(a), the charge distribution of the films is electrode limited. The charge distribution of the films is asymmetric and can be explained by the accumulated space charge phenomenon.

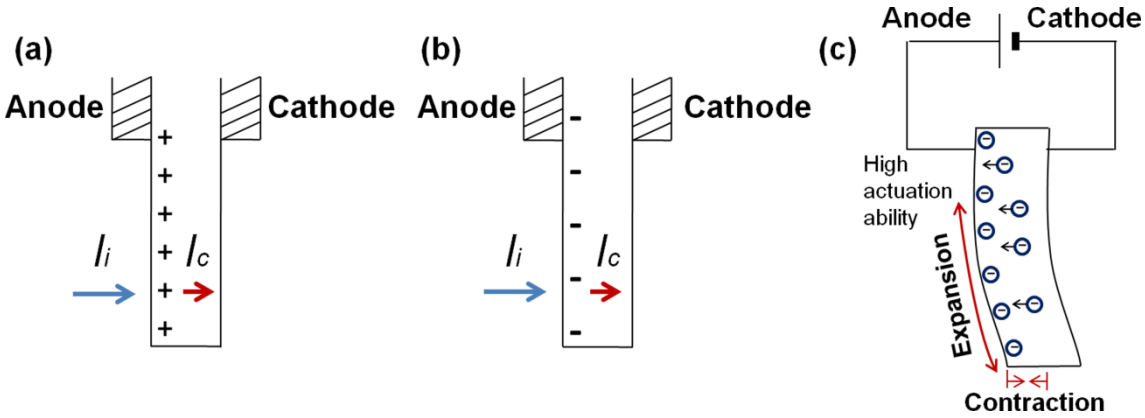

Fig. 6.9 Electric conduction in the polymers, (a) bulk-limited case ($I_i > I_c$), (b) electrode-limited case ($I_i < I_c$), and (c) a model of bending deformation for the KOH film.

The KOH films have an asymmetric charge distribution. The asymmetric charge distribution causes asymmetric strains within the films as illustrated in Fig. 6.9(c). The anode thus becomes a high actuation-ability area because the charge is accumulated there, and the cathode becomes a low actuation-ability area. Negative charge accumulation causes contraction in the direction of the thickness near the anode. Additionally, the contraction results in an expansion of the anode plane as the films maintain a constant volume. Asymmetric strain, i.e., the strain near the anode, causes the films to bend toward the cathode. From the actuator performance test, the results show that the films bend toward the cathode when voltage is applied. We considered

that the asymmetric strain that causes contraction and expansion of the KOH films assisted the actuation and the bending direction toward cathode.

6.4 Conclusions

An innovative polymer-based composite actuator was fabricated using PU as the matrix and two types of mild hydrothermally treated CNTs as the filler. The mild hydrothermally treated CNTs were found to be highly dispersed in a polar solvent and PU matrix. They contained more carboxyl and hydroxyl groups and showed less aggregation compared with pristine CNTs.

The films bent toward the cathode when voltage was applied and reverted to their original position when voltage was removed. The application of 10 V to the KOH 1.0 wt.% film gave the highest bending displacement of about 5.0 mm. Even upon the application of low voltage, we found that as the CNTs content increased, the films showed better bending displacement. All the films showed a stable bending displacement upon voltage cycling. The films also showed similar bending displacement upon voltage cycling, and this is considered to be a type of memory.

The KPS films were found to be highly polarized and bent because of Maxwell pressure. Changes to the length and width in the thickness direction were found to impart actuation. The KOH films showed a high accumulated charge density. Contraction and expansion in the direction of the thickness of the films triggered bending actuation in the films, and this helped us to understand the actuation mechanism of these polymer-based actuators.

References

[1] B. M. O'Brien, E. P. Calius, T. Inamura, S. Q. Xie, I. A. Anderson, Appl. Phys. A 100 (2010) 385-389.

[2] R. Kunanuruksapong, A. Sirivat, Appl. Phys. A 92 (2008) 313-320.

[3] G. J. H. Melvin, Q. Q. Ni, T. Natsuki, Microelectron. Eng. 126 (2014), 9-12.

[4] M. Ali, T. Hirai, J. Mater. Sci. 46 (2011) 7681-7688.

[5] M. Ali, T. Hirai, J. Mater. Sci. 47 (2012) 3777-3783.

[6] L. Z. Chen, C. H. Liu, C. H. Hu, S. S. Fan, Appl. Phys. Lett. 92 (2008) 263104.

[7] M. Watanabe, N. Wakimoto, H. Shirai, T. Hirai, J. Appl. Phys. 94 (2003) 2494-2497.

[8] L. Chen, C. Liu, K. Liu, C. Meng, C. Hu, J. Wang, S. Fan, ACS Nano 5 (2011) 1588-1593.

[9] R. Shankar, T. K. Ghosh, R. J. Spontak, Soft Matter 3 (2007) 1116-1129.

[10] N. J. Jo, D. H. Lim, G. M. Bark, H. H. Chun, I. W. Lee, H. Park, J. Mater. Sci. Technol. 26 (2010) 763-768.

[11] X. Zhang, C. Löwe, M. Wissler, B. Jähne, G. Kovacs, Adv. Eng. Mater. 7 (2005) 361-367.

[12] Z. Cai, J. Kim, J. Appl. Polym. Sci. 115 (2010) 2044.

[13] K. Y. Cho, H. G. Lim, S. R. Yun, J. Kim, K. S. Kang, J. Phys. Chem. C 112 (2008) 7001-7004.

[14] M. Watanabe, Polym. Int. 56 (2007) 1265-1271.

[15] Y. Nakama, J. Kyokane, K. Tokugi, T. Ueda, K. Yoshino, Synth. Met. 135-136 (2003) 749-750.

[16] S. Yun, J. Kim, Sens. Actuators A 154 (2009) 73-78.

[17] S. K. Yadav, S. S. Mahapatra, J. W. Cho, H. C Park, J. Y. Lee, Fibers Polym. 10 (2009) 756-760.

[18] Y. Bai, Y. Zhang, Q. Wang, T. Wang, J. Mater. Sci. 48 (2013) 2207-2214.

[19] L. V. Karabanova, R. L. D. Whitby, A. Korobeinyk, O. Bondaruk, J. P. Salvage, A. W. Lloyd, S. V. Mikhalovsky, Compos. Sci. Technol. 72 (2012) 865-872.

[20] L. Zhang, Y. Hashimoto, T. Taishi, Q. Q. Ni, Appl. Surf. Sci. 257 (2011) 1845-1849.

[21] N. G. Sahoo, Y. C. Jung, H. J. Yoo, J. W. Cho, Compos. Sci. Technol. 67 (2007) 1920-1929.

[22] G. Kofod, R. Kornbluh, R. Pelrine, P. Sommer-Larsen, J. Intell. Mater. Syst. Struct.

14 (2003) 787-793.

[23] L. Petit, B. Guiffard, L. Seveyrat, D. Guyomar, Sens. Actuators A 148 (2008) 105-110.

[24] R. E. Pelrine, R. D. Kornbluh, J. P. Joseph, Sens Actuators A 64 (1998) 77-85.

[25] K. Yoshino, Y. Inuishi, Oyo Buturi 49 (1980) 212-227.

Chapter 7

****

Conclusions

****

7 Conclusions

This dissertation has included the investigation of carbon nanotube (CNT) -based functional nanocomposites for the application of electromagnetic (EM) wave absorbers and electroactive actuators. The relationship and connection between the nanocomposites and EM wave absorption properties have been discussed. Furthermore, the bending actuation behavior of the electroactive nanocomposite films also has been studied to understand the actuation mechanism. CNTs, barium titanate (BTO) nanoparticles, silver (Ag) nanoparticles, and the hybrid nanopowders where BTO and Ag nanoparticles were grafted onto the surface of CNTs have been utilized.

First, in Chapter 1, general introduction of nanotechnology, nanocomposites, and nanomaterials has been presented. Brief summary related to CNTs, BTO and Ag nanoparticles also has been included. Accordingly, brief outline of EM wave absorber and electroactive polymers (EAPs) also has been reviewed.

In Chapter 2, BTO nanoparticles were prepared by sol-gel method and then grafted onto the surface of CNTs to fabricate BTO/CNT hybrid nanocomposites. The diameter of BTO nanoparticles was under 15 nm, ranging from 6 to 12 nm, with spherical shape. The high interfacial area of the hybrid nanomaterials results in high interfacial polarization and multiple scattering, which improves EM wave absorption. Samples with various weight fractions were fabricated and characterized. The reflection loss (*R.L.*) peak decreased from high frequency to lower frequency range and their response bandwidth became wider as the thickness of the sample increased. This proves that not only the weight fraction, the thickness of the samples also can be manipulated to produce absorption bands at different frequencies to design highly effective EM wave absorbers.

In Chapter 3, BTO nanoparticles were grafted onto the surface of CNTs and then incorporated into polyurethane (PU) matrix to fabricate single-layer and double-layer BTO/CNT nanocomposites. The diameter of BTO nanoparticles was under 15 nm, and good dispersion of them in PU was obtained. The double-layer absorber showed that

they can be manipulated to design high *R.L.*, thin, and wide response bandwidth materials. The *R.L.* peak decreased from high frequency to lower frequency range and their response bandwidth become wider as the thickness of the double-layer absorber increased. Thus, the thickness of samples can be controlled to produce absorption bands at different frequencies to produce optimum EM wave absorbers. For the double-layer absorber, the matching layer with excellent transmission capacity firstly achieved an excellent impedance matching, and then the absorption layer could achieve a favorable absorption capacity.

In Chapter 4, Ag nanoparticles were produced by chemical reduction process and then grafted onto the surface of CNTs to fabricate Ag/CNT hybrid nanomaterials. The Ag nanoparticles were less than 10 nm in diameter and showed no agglomeration when adhered to the surface of CNTs. The high interfacial area of the hybrid nanomaterials results in high interfacial polarization and multiple scattering, which improves EM wave absorption. Interestingly, the Ag/CNT hybrid nanomaterials showed two *R.L.* peaks, at low and high frequency region, as the thickness of the sample increased. They also showed wide minimum *R.L.* of over -10 dB (over 90% absorption). The thickness of the samples can be manipulated to produce absorption bands at different frequencies to fabricate excellent EM wave absorbers.

In Chapter 5, polymer-based electroactive nanocomposite was fabricated using PU and microwave-induced polymerization treated CNTs as the filler. The modified CNTs were found to be highly dispersed in a polar solvent and PU matrix. The introduction of methyl methacrylate (MMA) onto the surface of CNTs improved the dispersion of CNTs and they showed less aggregation compared with pristine CNTs. The films showed bending deformation toward the cathode when voltage was applied and reverted close to their original position when voltage was removed. The films also showed a stable bending displacement upon repetitive voltage cycle. The films also showed similar bending displacement upon voltage cycling and this is considered to be a type of memory. Maxwell pressure and the charge accumulation phenomenon cause contraction and expansion in the direction of the thickness of the films that triggered bending actuation in the films. This helped us to understand the actuation mechanism and bending deformation direction of this kind of electroactive nanocomposite material.

Finally, in Chapter 6, innovative polymer-based composite actuator was fabricated using PU as the matrix and two types (type 1 and 2) of mild hydrothermally treated CNTs as the filler. The mild hydrothermally treated CNTs were found to be highly dispersed in a polar solvent and PU matrix. They contained more functional groups such as carboxyl and hydroxyl groups and showed less aggregation compared with pristine CNTs. The films bent toward the cathode when voltage was applied and reverted to their original position when voltage was removed. Even upon the application of low voltage, we found that as the CNTs content increased, the films showed better bending displacement. All the films showed a stable bending displacement upon voltage cycling. The films also showed similar bending displacement upon voltage cycling, and this is considered to be a type of memory. The KPS films (type 2) were found to be highly polarized and bent because of Maxwell pressure. Changes to the length and width in the thickness direction were found to impart actuation. The KOH films showed a high accumulated charge density. Contraction and expansion in the direction of the thickness of the films triggered bending actuation in the films, and thus a reasonable explanation of the actuation mechanism of these polymer-based actuators.

ACCOMPLISHMENTS

LIST OF PUBLICATIONS

****

Journal Publications

[1] **Gan Jet Hong Melvin**, Qing-Qing Ni, Toshiaki Natsuki, Electromagnetic wave absorption properties of barium titanate/carbon nanotube hybrid nanocomposites; Journal of Alloys and Compounds, 615 (2014) 84-90.

[2] **Gan Jet Hong Melvin**, Qing-Qing Ni, Yusuke Suzuki, Toshiaki Natsuki, Microwave-absorbing properties of silver nanoparticle/carbon nanotube hybrid nanocomposites; Journal of Materials Science, 49 (2014) 5199-5207.

[3] **Gan Jet Hong Melvin**, Qing-Qing Ni, Toshiaki Natsuki, Behavior of polymer-based electroactive actuator incorporated with mild hydrothermally treated CNTs; Applied Physics A: Materials Science & Processing, 117 (2014) 2043-2050.

[4] **Gan Jet Hong Melvin**, Qing-Qing Ni, Toshiaki Natsuki, Bending actuation and charge distribution behavior of polyurethane/carbon nanotube electroactive nanocomposites; Polymer Composites, DOI: 10.1002/pc.23177.

[5] **Gan Jet Hong Melvin**, Qing-Qing Ni, Toshiaki Natsuki, Fabrication and characterization of polymer-based electroactive nanocomposite actuator; Microelectronic Engineering, 126 (2014) 9-12.

[6] Toshiaki Natsuki, **Gan Jet Hong Melvin**, Qing-Qing Ni, Vibrational Frequencies and Raman Radial Breathing Modes of Multi-Walled Carbon Nanotubes Based on Continuum Mechanics; Journal of Materials Science Research, 2(4) (2013).

Conferences

International

[1] **Gan Jet Hong Melvin**, Toshiaki Natsuki, Qing-Qing Ni, Bending behavior of polymer-based electroactive nanocomposite actuator incorporated with modified CNTs; International Symposium on Fiber Science and Technology 2014, ISF2014 (September 2014, Tokyo, Japan).

[2] **Gan Jet Hong Melvin**, Toshiaki Natsuki, Qing-Qing Ni, Carbon-based electroactive nanocomposite actuator of thin films; 3rd International Symposium on Advanced Textile Science and Technology, ISATST2013 (November 2013, Hangzhou, China).

[3] **Gan Jet Hong Melvin**, Qing-Qing Ni, Toshiaki Natsuki, Fabrication and characterization of polymer-based electroactive nanocomposite actuator; 8th International Conference on Surfaces, Coatings and Nanostructured Materials, NANOSMAT2013 (September 2013, Granada, Spain).

[4] Qing-Qing Ni, **Gan Jet Hong Melvin**, Hong Xia, Toshiaki Natsuki, Shape memory polyper based nanocomposite actuators; 19th International Conference on Composite Materials, ICCM19 (July 2013, Montreal, Canada).

[5] Qing-Qing Ni, **Gan Jet Hong Melvin**, Hong Xia, Actuation and shape memory effect of SMP/CNTs nanocomposites; 6th Asia-Europe Symposium on Processing and Properties of Reinforced Polymers, AESP6 (June 2013, Wuhan, China).

[6] **Gan Jet Hong Melvin**, Toshiaki Natsuki, Qing-Qing Ni, Fabrication and evaluation of shape memory polymer based composite actuator; The 8th Asian-Australasian Conference on Composite Materials, ACCM8 (November 2012, Kuala Lumpur, Malaysia).

[7] Qing-Qing Ni, **Melvin Gan Jet Hong**, Hong Xia, Guangze Dai, Composite actuator with shape memory polymer and carbon nanotubes; The 8th International Forum on Advanced Materials Science and Technology, IFAMST-8 (August 2012, Fukuoka, Japan).

Domestic (Japan)

[1] **Gan Jet Hong Melvin**, Toshiaki Natsuki, Qing-Qing Ni, Fabrication and electromagnetic wave absorption behavior of BTO/CNT nanocomposites; The 6th Japan Composite Materials Conference, JCCM6 (March 2015, Tokyo, Japan).

[2] **Gan Jet Hong Melvin**, Toshiaki Natsuki, Qing-Qing Ni, Behavior of shape memory polymer/carbon nanotubes nanocomposite as an electroactive actuator film; The 5th Japan Composite Materials Conference, JCCM5 (March 2014, Kyoto, Japan).

[3] **Gan Jet Hong Melvin**, Toshiaki Natsuki, Qing-Qing Ni, Fabrication and evaluation of shape memory polymer based composite actuator; The 3rd Japan Composite Materials Conference, JCCM3, (March 2012, Kyoto, Japan).

[4] **Gan Jet Hong Melvin**, Toshiaki Natsuki, Qing-Qing Ni, Actuator behavior of shape memory polymer based composites; The 40th Japan Society of Mechanical Engineer Student Conference, (March 2011, Ueda, Japan).

ACKNOWLEDGEMENTS

****

"It is not possible to prepare a dissertation without the assistance and encouragement of other people. This one is certainly no exception."

First and foremost, I would like to express my sincere gratitude to my supervisor, Prof. Qing-Qing Ni, for his exemplary guidance, valuable advice, and constant encouragement throughout my PhD course. The knowledge and assistance given by him from time to time shall carry me a long way in the journey of life on which I am about to embark.

I am also grateful to Prof. Toshiaki Natsuki as my co-supervisor and co-referee, for his valuable and constructive suggestions during the development of this research work. Without his enthusiastic encouragement and useful critiques, this research would not have been successful.

I also want to forward my gratitude to Prof. Hajime Konishi, for his extensive advises and guidance for this research work. My deepest gratitude also goes to the committee members, Prof. Yasushi Murakami and Prof. Jianhui Qiu, for their helpful suggestions and comments regarding my research.

I also want to take this opportunity to express a deep sense of gratitude to EPSON International Scholarship Foundation and Grants for Excellent Graduate Schools by the Ministry of Education, Culture, Sports, Science and Technology, Japan through International Fiber Engineering Course of Shinshu University for the financial support.

I wish to thank various people; Mr. Isao Nakamura, Ms. Miho Nakamura, Ms. Makiko Shinotsuka, Ms. Ayako Nishida, Ms. Keiko Kakegawa, Mr. Shouhei Koyama, for their valuable technical support and extensive guidance of experimental equipments on this research.

Special thanks also to all my graduate friends, especially my research group members. I am particularly indebted to Dr. Li Zhang, Dr. Yao-Feng Zhu, and Mr. Yusuke Suzuki for their assistance and precious suggestions on my research.

An honorable mention goes to my beloved families, especially my beloved parents, for their understanding, support, and endless love, through the duration of my study. I also would like to thank all my friends at Shinshu University for their constant friendship and warm encouragement.

Any omission in this brief acknowledgement does not mean lack of gratitude.

Thank you

Melvin Gan Jet Hong